ДОНСКОЙ ГОСУДАРСТВЕННЫЙ ТЕХНИЧЕСКИЙ УНИВЕРСИТЕТ

ДГТУ

Advanced Engineering Research

Theoretical and scientific-practical journal

Vol. 22

no. 2

2022

ISSN 2687-1653

1 Mechanics

2 Machine Building and Machine Science

3 Information Technology, Computer Science, and Management

DOI 10.23947/2687-1653

vestnik-donstu.ru

Advanced Engineering Research

Vol. 22, no. 2

Theoretical and scientific-practical journal

Published since 1999

Quarterly
April-June 2022

ISSN 2687-1653
DOI: 10.23947/2687-1653

Founder and publisher — Federal State Budgetary Educational Institution of Higher Education

Don State Technical University (DSTU)

The journal was known as Vestnik of Don State Technical University (until August 2020)

Included in the list of peer-reviewed scientific editions where the basic research results of doctoral, candidate's theses should be published (State Commission for Academic Degrees and Titles List) in the following research areas:

01.02.01 – Analytical Mechanics (Engineering Sciences)
01.02.04 – Deformable Solid Mechanics (Engineering Sciences)
01.02.04 – Deformable Solid Mechanics (Physicomathematical Sciences)
01.02.06 – Dynamics, Strength of Machines, Gear, and Equipment (Engineering Sciences)
05.02.02 – Engineering Science, Drive Systems and Machine Parts (Engineering Sciences)
05.02.04 – Machine Friction and Wrear (Engineering Sciences)
05.02.07 – Technology and Equipment of Mechanical and Physicotechnical Processing (Engineering Sciences)
05.02.08 – Engineering Technology (Engineering Sciences)
05.02.10 – Welding, Allied Processes and Technologies (Engineering Sciences)
05.02.11 – Testing Methods and Diagnosis in Machine Building (Engineering Sciences)
05.13.11 – Software and Mathematical Support of Machines, Complexes and Computer Networks (Engineering Sciences)
05.13.17 – Foundations of Information Science (Engineering Sciences)
05.13.18 – Mathematical Simulation, Numerical Methods and Program Systems (Engineering Sciences)

The journal is indexed and archived in the Russian Science Citation Index (RSCI), in the International Database EBSCO (Academic Search Ultimate Magazines and Journals), Dimensions, CyberLeninka, ROAD, GoogleScholar. The journal is a member of Directory of Open Access Journals (DOAJ), Association of Science Editors and Publishers (ASEP) and CrossRef.

Certificate of mass media registration ЭЛ № ФС 77 – 78854 of 07.08.2020 is issued by the Federal Service for Supervision of Communications, Information Technology, and Mass Media

The issue is prepared by:

Inna V. Boyko, Gennady I. Rassokhin, Marina P. Smirnova (English version)

Founder's, Publisher's and Printery Address:

Gagarin Sq. 1, Rostov-on-Don, 344003, Russia. Phone: +7 (863) 2-738-372

E-mail: vestnik@donstu.ru http://vestnik-donstu.ru/

CONTENTS

ANNIVERSARY OF THE SCIENTIST

Yury Olegovich Chernyshev, engineer, teacher, scientist, is 85

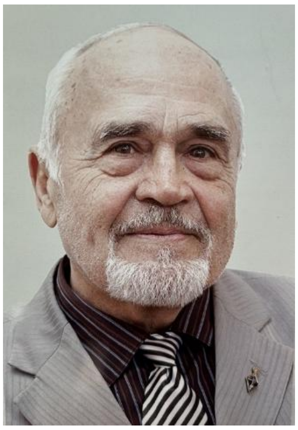

July 11, 2022, marks 85 years since birth of Yuri Olegovich Chernyshev, the Honored Scientist of the Russian Federation, Honorary Professor of DSTU, Professor of the Production Automation Department, Don State Technical University (DSTU), chief researcher of the R&D Center, Krasnodar Higher Military School named after Army General S. M. Shtemenko. He devoted 63 years of his life to scientific, pedagogical and scientific-organizational activities.

Yuri O. Chernyshev graduated from Taganrog Radio Engineering Institute in 1959, defended his candidate's thesis in 1967, and his doctorate dissertation — in 1984.

From 1959 to 1980, he worked in Rostov-on-Don. He was associate professor in Rostov Institute of Agricultural Engineering, as well as senior engineer — head of the group, Rostov Higher Military Command and Engineering School of Rocket Forces named after Artillery Chief Marshal M. I. Nedelin. From 1981 to 1983, he was Director of the North Caucasus Branch of the Russian Branch of the State Design and Technological Institute for the Mechanization of Accounting and Computing Works of the Central Statistical Bureau of the USSR.

Since 1983, Yuri Olegovich has been Head of the Electrical Engineering and Automation Production Department, Rostov State Academy of Agricultural Machinery (RGASKHM). In 1988, he founded the Department of Applied Mathematics and Computer Science at this university and headed it. From joining RGASKHM to DSTU in 2009 to the present day, Yuri O. Chernyshev has been a professor at the Production Automation Department, Don State Technical University, and a chief researcher of the R&D Center, Krasnodar Higher Military School named after Army General S. M. Shtemenko.

Yuri Olegovich Chernyshev is a leading scientist in the field of optimal design of production processes and computing structures, practical creation of computer-aided design systems, automatic process control systems.

The scientist made a great contribution to the training of highly qualified scientific and pedagogical personnel. He enriched science with major scientific works and developments in the field of computer technology, theoretical and technical cybernetics. Under his leadership, about 80 fundamental state-budgeted and self-supporting R&D of national importance with a significant economic effect, confirmed by the relevant implementation acts, were carried out.

Yuri Olegovich has created a successful scientific school in the field of non-traditional models and methods for solving optimization design problems. Nowadays, the school is still running successfully. He has trained 7 doctors and 35 candidates of sciences.

His fruitful scientific activity is presented by more than 500 research papers, including 17 monographs, 22 patents, 18 programs in the funds of algorithms and programs.

Professor Yu. O. Chernyshev was recognized by the domestic and foreign scientific community. From 1976 to 2016, he was a member of three dissertation councils for the defense of doctoral and candidate dissertations. From 1995 to 2000, he was a reviewer of the international journal “Mathematical Reviews” (USA, University of Michigan); a member of the editorial board of the journal “Advanced Engineering Research”, a member of the American Mathematical Society.

In 2001, he received a Letter of Acknowledgement from Governor of the Rostov region “For a great personal contribution to the development of Don science and vocational education”.

In 1996, by Decree of President of the Russian Federation, Yuri Olegovich was awarded the honorary title “Honored Scientist of the Russian Federation”, in 2003 he was awarded the Order of Friendship, in 2008 — the Vernadsky Gold Medal, and in 2020 — the L. V. Krasnichenko medal. In 2011, Yu. O. Chernyshev was given the title of “Honorary Professor of DSTU”.

MECHANICS

UDC 539.3
https://doi.org/10.23947/2687-1653-2022-22-2-81-90

Original article

Related Dynamic Axisymmetric Thermoelectroelasticity Problem for a Long Hollow Piezoceramic Cylinder

Dmitriy A. Shlyakhin ✉, **Mariya A. Kalmova**
Samara State Technical University, 244, Molodogvardeyskaya St., Samara, Russian Federation
✉ d-612-mit2009@yandex.ru

Abstract

Introduction. The article studies the problem of investigation of coupled nonstationary thermoelectroelastic fields in piezoceramic structures. The main approaches related to the construction of a general solution to the initial non-self-adjoint equations describing the process under consideration are briefly outlined. The work aims at constructing a new closed solution to the axisymmetric thermoelectroelasticity problem for a long piezoceramic cylinder.

Materials and Methods. A long hollow cylinder whose electrodated surfaces were connected to a measuring device with large input resistance was considered. On the cylindrical surfaces of the plate, a time-varying temperature was given. The hyperbolic theory of Lord–Shulman thermo-electro-elasticity was used. The closed solution is constructed using a generalized method of finite integral transformations.

Results. The developed calculation algorithm makes it possible to determine the stress–strain state of the cylinder, its temperature, and electric fields. In addition, it becomes possible to investigate the coupling of fields in a piezoceramic cylinder, as well as to analyze the effect of relaxation of the heat flow on the fields under consideration.

Discussion and Conclusion. The use of assumptions about the equality of the components of the temperature stress tensor and the absence of temperature effect on the electric field allowed us to formulate a self-adjoint initial system of equations and construct a closed solution.

Keywords: thermoelectroelasticity, hyperbolic theory, nonstationary coupled problem, long piezoceramic cylinder, finite integral transformations.

Acknowledgements: the authors express their gratitude to the editors for their attentive attitude to the article and the comments, which made it possible to improve its quality.

For citation: D. A. Shlyakhin, M. A. Kalmova. Coupled dynamic axisymmetric thermoelectroelasticity problem for a long hollow piezoceramic cylinder. Advanced Engineering Research, 2022, vol. 22, no. 2, pp. 81–90. https://doi.org/10.23947/2687-1653-2022-22-2-81-90

Introduction. Recently, different-purpose technical devices made of piezoceramic material have become widespread. Here, devices whose operation is based on the effect of the coupling of elastic, electric and temperature fields hold a specific place [1]. Various theories of thermoelectroelasticity were developed to describe their work taking into account the coupling of fields [2–4]. At the same time, for a better description and evaluation of non-stationary processes in structures, it was required to construct analytical solutions. However, the mathematical formulation of the problems under consideration included a system of non-self-adjoint partial differential equations, whose integration was difficult to treat mathematically.

To solve this problem, as a rule, equations are investigated in an uncoupled form [5, 6], infinitely long bodies are analyzed [7−11], or thermoelectroelasticity problems are considered in a quasi-static formulation [12, 13].

In this paper, we consider a coupled dynamic thermoelectroelasticity problem for an infinitely long hollow piezoceramic cylinder. As a result of the transformation of the initial calculated ratios, it was possible to form a self-adjoint system of equations, the integration of which was carried out by the method of incomplete separation of variables in the form of a generalized finite integral transformation [13].

Materials and Methods. Let a hollow, long, loose in the radial plane, piezoceramic cylinder occupy area Ω in the cylindrical coordinate system (r_*,θ,z): $\{a \le r_* \le b, 0 \le \theta \le 2\pi, -\infty < z < \infty\}$. On the cylindrical surfaces, the temperature is given in the form of the following nonstationary functions (boundary conditions of the 1st kind) — $\omega_1^*(t_*)$ ($r_* = a$), $\omega_2^*(t_*)$ $(r_* = b)$. The internal electrodated surface is grounded, and the external one is connected to a measuring device with a large input resistance (electric idle mode.

The mathematical formulation of the axisymmetric problem under consideration in dimensionless form includes differential equations of motion, electrostatics, and thermal balance based on the hyperbolic Lord–Shulman theory, as well as the boundary conditions [2, 7, 15]:

$$\nabla\frac{\partial U}{\partial r} - a_1\frac{U}{r^2} + \nabla\frac{\partial \phi}{\partial r} - a_2\frac{1}{r}\frac{\partial \phi}{\partial r} - \nabla\Theta + a_3\frac{\Theta}{r} - \frac{\partial^2 U}{\partial t^2} = 0, \tag{1}$$

$$-\nabla\frac{\partial \phi}{\partial r} + a_4\nabla\frac{\partial U}{\partial r} + a_5\frac{1}{r}\frac{\partial U}{\partial r} + a_6\nabla\Theta = 0,$$

$$\nabla\frac{\partial \Theta}{\partial r} - \left(\frac{\partial}{\partial t} + \beta\frac{\partial^2}{\partial t^2}\right)\left(a_7\Theta + a_8\nabla U\right) = 0;$$

$$r = R,1\ \frac{\partial U}{\partial r} + a_9\frac{U}{r} + \frac{\partial \phi}{\partial r} - \Theta = 0\ ,\Theta_{|r=R} = \omega_1, \Theta_{|r=1} = \omega_2, \tag{2}$$

$$\phi_{|r=R} = 0\ ,\left(-\frac{\partial \phi}{\partial r} + a_4\frac{\partial U}{\partial r} + a_5\frac{U}{r} + a_6\Theta\right)_{|r=1} = 0\ ;$$

$$t = 0\ U = \Theta = 0\ ,\frac{\partial U}{\partial t} = 0, \frac{\partial \Theta}{\partial t} = \dot{\Theta}_0; \tag{3}$$

where $\{U,r,R\} = \{U^*,r_*,a\}/b$, $\phi = \frac{e_{33}}{C_{33}b}\phi^*$, $\{\Theta,\omega_1,\omega_2\} = \frac{\gamma_{33}}{C_{33}}\{\Theta^*,\omega_1^*-T_0,\omega_2^*-T_0\}$, $\{t,\beta\} = \frac{\{t_*,\beta_{rel}\}}{b}\sqrt{\frac{C_{33}}{\rho}}$, $a_1 = \frac{C_{11}}{C_{33}}$, $a_2 = \frac{e_{31}}{e_{33}}$, $a_3 = \frac{\gamma_{11}}{\gamma_{33}}$, $a_4 = \frac{e_{33}^2}{C_{33}\varepsilon_{33}}$, $a_5 = \frac{e_{31}e_{33}}{C_{33}\varepsilon_{33}}$, $a_6 = \frac{g_3 e_{33}}{\varepsilon_{33}\gamma_{33}}$, $a_7 = k\frac{b}{\Lambda}\sqrt{\frac{C_{33}}{\rho}}$, $a_8 = \frac{b\gamma_{33}^2 T_0}{\Lambda\sqrt{C_{33}\rho}}$, $a_9 = \frac{C_{13}}{C_{33}}$

$U^*(r_*,t_*),\phi^*(r_*,t_*),\Theta^*(r_*,t_*)$ — accordingly, the radial component of the displacement vector, the electric field potential, and the temperature increment in dimensional form; ($\Theta^*(r_*,t_*) = T(r_*,t_*) - T_0(r_*)$, — current temperature and temperature of the initial state of the body; $C_{ms},\rho,e_{ms},\varepsilon_{33}$ — elastic moduli, density, piezo module, and permittivity coefficient of electroelastic anisotropic material; $\left(m,s=\overline{1,3}\right)$; γ_{11},γ_{33} — components of the temperature stress tensor ($\gamma_{11} = C_{11}\alpha_t$, $\gamma_{33} = C_{33}\alpha_t$); Λ,k,α_t — coefficients of thermal conductivity, volumetric heat capacity, and linear thermal expansion of the material; g_3 — component of the pyroelectric coefficient tensor; β_{rel} — relaxation time; $\dot{\Theta}_0$ — the rate of temperature change known at the initial moment; $\nabla = \frac{\partial}{\partial r} + \frac{1}{r}$.

In the case of grounding of the inner surface of a piezoceramic element, electrical voltage $V(t_*)$ is determined by the potential on its outer surface:

$$V(t_*) = \phi(1,t_*)\,. \tag{4}$$

When constructing a general solution at the first stage of the study, the radial component of the electric field intensity vector is determined as a result of integrating the electrostatics equation:

$$E_r = \frac{\partial \phi}{\partial r} = a_4 \frac{\partial U}{\partial r} + a_5 \frac{U}{r} + a_6 \Theta + \frac{D_1}{r}, \tag{5}$$

where D_1 — integration constant.

Substituting (5) into (1)–(3) allows us to formulate a new problem with respect to functions $U(r,t), \Theta(r,t)$. In this case, the condition of the absence of a radial component of the electric field induction vector on the outer cylindrical surface of the element (the last equality (2)) is fulfilled at $D_1 = 0$; and the condition of grounding of the inner surface ($\phi_{|r=R} = 0$) is satisfied as a result of integration (5).

At the next stage of the solution, the inhomogeneous boundary conditions (2) are reduced to a form that allows further use of the procedure for incomplete separation of variables by the method of finite integral transformations. To do this, new functions $u(r,t)$, $N(r,t)$ related to $U(r,t)$, $\Theta(r,t)$ are introduced:

$$U(r,t) = H_1(r,t) + u(r,t),\ \Theta(r,t) = H_2(r,t) + N(r,t), \tag{6}$$

where $H_1(r,t) = f_1(r) A(1,t) + f_2(r) A(R,t) + f_3(r)\omega_1(t) + f_4(r)\omega_2(t)$,

$$H_2(r,t) = f_5(r)\omega_1(t) + f_6(r)\omega_2(t),$$

$f_1(r)...f_6(r)$ — twice differentiable function, $A(r,t)_{r=R,1} = (1 + a_4 - a_5 - a_9)U(r,t)/r$.

Substituting (6) into the calculated ratios (1)–(3) with respect to functions $U(r,t), \Theta(r,t)$ when the following conditions are met:

$$(1+a_4)\nabla H_1 + (a_6 - 1) H_2 = A(r,t)_{r=R,1},\ H_{2|r=R} = \omega_1,\ H_{2|r=1} = \omega_2, \tag{7}$$

allows us to get a new boundary value problem with respect to function $u(r,t)$, $N(r,t)$:

$$\nabla \frac{\partial u}{\partial r} - b_1 \frac{u}{r^2} + b_2 \frac{\partial N}{\partial r} + b_3 \frac{N}{r} - \frac{1}{(1+a_4)} \frac{\partial^2 u}{\partial t^2} = F_1, \tag{8}$$

$$\nabla \frac{\partial N}{\partial r} - \left(\frac{\partial}{\partial t} + \beta \frac{\partial^2}{\partial t^2} \right)(a_7 N + a_8 \nabla u) = F_2;$$

$$r = R,1\ \nabla u = 0,\ N = 0; \tag{9}$$

$$t = 0\ u = -H_1(r,0),\ N = -H_2(r,0), \tag{10}$$

$$\frac{\partial u}{\partial t} = -\frac{\partial H_1(r,t)}{\partial t},\ \frac{\partial N}{\partial t} = \dot{\Theta}_0 - \frac{\partial H_2(r,t)}{\partial t};$$

where $F_2 = -\nabla \frac{\partial H_2}{\partial r} + \left(\frac{\partial}{\partial t} + \beta \frac{\partial^2}{\partial t^2} \right)(a_7 H_2 + a_8 \nabla H_1)$,

$F_1 = -\nabla \frac{\partial H_1}{\partial r} + b_1 \frac{H_1}{r^2} + b_2 \frac{\partial H_2}{\partial r} + b_3 \frac{H_2}{r} + \frac{1}{(1+a_4)} \frac{\partial^2 H_1}{\partial t^2}$,

$b_1 = \frac{a_1 + a_2 a_5}{1+a_4},\ b_2 = \frac{a_6 - 1}{1+a_4},\ b_3 = b_2 + \frac{a_3 - a_2 a_6}{1+a_4}$.

It should be noted here that $A(r,t)$ is a function of the displacements of the cylindrical surfaces of the cylinder. Initially, $A(r,t)$ is equated to zero with its subsequent determination and refinement H_1, F_1, F_2.

Further transformations of the calculated ratios (8)–(10) are associated with the use of the following assumptions: $b_1 = 1$, $b_3 = 0$, and the introduction of a thermoelastic potential

$$N = \nabla B. \tag{11}$$

Condition $b_1 = 1$ can be accepted without a large error, since for piezoceramic materials $b_1 = 0.94 \div 0.98$, and dependence $b_3 = 0$ is fulfilled in the case of equality of the components of the temperature stress tensor ($\gamma_{11} = \gamma_{33}$) and the absence of temperature influence on the electric field ($g_3 = 0$).

As a result, the following task is formed regarding $u(r,t), B(r,t)$:

$$\frac{\partial}{\partial r}\nabla u + b_2 \frac{\partial}{\partial r}\nabla B - \frac{1}{(1+a_4)}\frac{\partial^2 u}{\partial t^2} = F_1, \tag{12}$$

$$\frac{\partial}{\partial r}\nabla B - \left(\frac{\partial}{\partial t} + \beta\frac{\partial^2}{\partial t^2}\right)(a_7 B + a_8 u) = F_3;$$

$$r = R,1 \ \nabla u = \nabla B = 0 \ ; \tag{13}$$

$$t = 0 \ u = -H_1(r,0) \ , \nabla B = -H_2(r,0), \tag{14}$$

$$\frac{\partial u}{\partial t} = -\frac{\partial H_1(r,t)}{\partial t}, \frac{\partial}{\partial t}\nabla B = \dot{\Theta}_0 - \frac{\partial H_2(r,t)}{\partial t};$$

where $F_3 = -\frac{\partial H_2}{\partial r} + \left(\frac{\partial}{\partial t} + \beta\frac{\partial^2}{\partial t^2}\right)(a_7 H_3 + a_8 H_1), \nabla H_3 = f_5(r)\omega_1(t) + f_6(r)\omega_2(t)$.

The initial boundary value problem (12)–(14) is solved using the structural algorithm of the generalized finite integral transformation (FIT) [14]. At the same time, it is possible to use single-component unknown transformation kernel $K(\lambda_i, r)$ for this task:

$$\{G_1(\lambda_i,t), G_2(\lambda_i,t)\} = \int_R^1 \{u(r,t), B(r,t)\} K(\lambda_i,r) r dr, \tag{15}$$

$$\{u(r,t), B(r,t)\} = \sum_{i=1}^{\infty} \{G_1(\lambda_i,t), G_2(\lambda_i,t)\} K(\lambda_i,r) \|K_i\|^{-2}, \tag{16}$$

$$\|K_i\|^2 = \int_R^1 K(\lambda_i,r)^2 r dr \ ;$$

where λ_i — eigenvalues forming a countable set.

As a result of using the FIT algorithm [14], we obtain problems with respect to the transformation kernel $K(\lambda_i, r)$:

$$\frac{d^2 K(\lambda_i,r)}{dr^2} + \frac{1}{r}\frac{dK(\lambda_i,r)}{dr} + \left(\lambda_i^2 - \frac{1}{r^2}\right) K(\lambda_i,r) = 0, \tag{17}$$

$$r = R,1 \ \nabla K(\lambda_i,r) = 0, \tag{18}$$

and transform $G_1(\lambda_i,t), G_2(\lambda_i,t)$:

$$-\lambda_i^2 G_{1i} + \frac{\lambda_i^2}{(1+a_4)} G_{2i} - \frac{1}{(1+a_4)}\frac{d^2 G_{1i}}{dt^2} = F_{1H} \ , \tag{19}$$

$$-\lambda_i^2 G_{2i} - \left(\frac{d}{dt} + \beta\frac{d^2}{dt^2}\right)(a_7 G_{2i} + a_8 G_{1i}) = F_{2H} \ ;$$

$$t = 0 \ G_{1i} = G_{1i0}, \frac{dG_{1i}}{dt} = \dot{G}_{1i0}, G_{2i} = G_{2i0}, \frac{dG_{2i}}{dt} = \dot{G}_{2i0}; \tag{20}$$

where $\{F_{1H}, F_{2H}\} = \int_R^1 \{F_1, F_3\} K(\lambda_i,r) r dr$, $\{G_{1i0}, G_{2i0}\} = -\int_R^1 \{H_1(r,0), H_2(r,0)\} K(\lambda_i,r) r dr$,

$$\{\dot{G}_{1i0}, \dot{G}_{2i0}\} = \int_R^1 \left\{ -\frac{\partial H_1(r,t)}{\partial t}\bigg|_{t=0}, \left(\dot{\Theta}_0 - \frac{\partial H_1(r,t)}{\partial t}\right)\bigg|_{t=0} \right\} K(\lambda_i,r) r dr.$$

The general solution to problem (17), (18) has the form:

$$K(\lambda_i, r) = Y_0(\lambda_i) J_1(\lambda_i r) - J_0(\lambda_i) Y_1(\lambda_i r). \tag{21}$$

Here, eigenvalues λ_i are determined using the following transcendental equation:

$$Y_0(\lambda_i) J_0(\lambda_i R) - J_0(\lambda_i) Y_0(\lambda_i R) = 0.$$

The system of differential equations (19) is reduced to the following resolving equation of the 4th order with respect to $G_1(\lambda_i, t)$:

$$\left(\frac{d^4}{dt^4} + b_4 \frac{d^3}{dt^3} + b_{5i}\frac{d^2}{dt^2} + b_{6i}\frac{d}{dt} + b_{7i}\right) G_{1i} = F_H, \tag{22}$$

where $F_H = -\dfrac{\lambda^2}{a_7 \beta}\left[F_{2H} + (1+a_4) F_{1H}\right] - \dfrac{(1+a_4)}{\beta}\left(\dfrac{\partial}{\partial t} + \beta \dfrac{\partial^2}{\partial t^2}\right) F_{1H}$,

$b_4 = \dfrac{1}{\beta}$, $b_{5i} = \lambda_i^2\left(1 + a_4 + \dfrac{a_8}{a_7} + \dfrac{1}{a_7 \beta}\right)$, $b_{6i} = \dfrac{\lambda_i^2}{\beta}\left(1 + a_4 + \dfrac{a_8}{a_7}\right)$, $b_{7i} = \lambda_i^4 \dfrac{(1+a_4)}{a_7 \beta}$.

Since the characteristic equation corresponding to (22),

$$k^4 + b_4 k^3 + b_{5i} k^2 + b_{6i} k + b_{7i} = 0,$$

is valid, then it, from the condition of the oscillating solution for $G_1(\lambda_i, t)$, has two real roots (k_{1i}, k_{2i}) and two complex-conjugate roots

$$(k_{3i} = \sigma + i\omega,\ k_{4i} = \sigma - i\omega).$$

In this case, the general solution to equation (22) has the form:

$$G_1(\lambda_i, t) = D_{2i}\exp(k_{1i} t) + D_{3i}\exp(k_{2i} t) + D_{4i}\exp(k_{3i} t) + D_{5i}\exp(k_{4i} t) + \tag{23}$$

$$+ b_{8i}\int_0^t F_H(\tau)\left\{\exp\left[k_{1i}(t-\tau)\right] - \exp\left[k_{2i}(t-\tau)\right]\right\} d\tau + b_{9i}\int_0^t F_H(\tau)\exp\left[\sigma(t-\tau)\right]\left\{b_{10i}\sin(\omega t - \omega\tau) - b_{11i}\cos(\omega t + \omega\tau)\right\} d\tau,$$

where $b_{8i} = \left\{(k_{1i} - k_{2i})\left[(k_{1i} - \sigma)^2 + \omega^2\right]\right\}^{-1}$, $b_{9i} = \left[\omega\left(b_{10i}^2 + b_{11i}^2\right)\right]^{-1}$, $\sigma = \dfrac{k_{3i} + k_{4i}}{2}$, $b_{10i} = k_{1i}k_{2i} - (k_{1i} + k_{2i})\sigma + \sigma^2 - \omega^2$,

$b_{11i} = \omega(2\sigma - k_{1i} - k_{2i})$, $\omega = \left|\dfrac{k_{3i} - k_{4i}}{2i}\right|$.

Function $G_2(\lambda_i, t)$ is determined from the first equation of system (19). Substitution of the obtained expressions for the transforms under the boundary conditions (20) makes it possible to determine the integration constants $D_{2i} ... D_{5i}$ . .. (19).

Substitution of $G_1(\lambda_i, t)$, $G_2(\lambda_i, t)$ into (16), (11), (6) allows us to get the final expressions for functions $U(r,t)$, $\Theta(r,t)$:

$$U(r,t) = H_1(r,t) + \sum_{i=1}^{\infty} G_1(\lambda_i, t) K(\lambda_i, r)\|K_i\|^{-2}, \tag{24}$$

$$\Theta(r,t) = H_2(r,t) + \sum_{i=1}^{\infty} G_2(\lambda_i, t)\nabla K(\lambda_i, r)\|K_i\|^{-2}.$$

At the final stage of the study, functions $H_1(r,t), H_2(r,t)$ are determined through solving the following differential equations:

$$\nabla\frac{\partial H_1}{\partial r} - b_1 \frac{H_1}{r^2} - b_2 \frac{\partial H_2}{\partial r} - b_3 \frac{H_2}{r} = 0,\ \nabla\frac{\partial H_2}{\partial r} = 0, \tag{25}$$

which makes it possible to significantly simplify the right parts (F_1, F_2) of the calculated ratios (8).

Substitution of expressions for H_1, H_2 in (25) enables to form systems of equations with respect to functions $f_1(r)...f_6(r)$, that are determined when the conditions are satisfied (7).

The potential of the electric field of a piezoceramic cylinder is determined from integrating equality (5) and satisfying the next-to-last boundary condition (2):

$$\phi = \int\left[a_4\frac{\partial H_1(r,t)}{\partial r} + a_5\frac{H_1(r,t)}{r} + a_6 H_2(r,t)\right]dr + \qquad (26)$$

$$+\sum_{i=1}^{\infty} G_1(\lambda_i,t)B_1(\lambda_i)\|K_i\|^{-2} + a_6\sum_{i=1}^{\infty} G_2(\lambda_i,t)B_2(\lambda_i)\|K_i\|^{-2} + D_6(t)$$

where $D_6(t) = -\left[\int\left[a_4\frac{\partial H_1(r,t)}{\partial r} + a_5\frac{H_1(r,t)}{r} + a_6 H_2(r,t)\right]dr + \sum_{i=1}^{\infty} G_1(\lambda_i,t)B_1(\lambda_i)\|K_i\|^{-2} +\right.$

$\left. + a_6\sum_{i=1}^{\infty} G_2(\lambda_i,t)B_2(\lambda_i)\|K_i\|^{-2}\right]_{|r=R}$, $B_1(\lambda_i) = \int\left[a_4\frac{\partial K(\lambda_i,r)}{\partial r} + a_5\frac{K(\lambda_i,r)}{r}\right]dr$,

$B_2(\lambda_i) = \int \nabla K(\lambda_i,r)dr$.

The obtained calculated relations (24), (26) satisfy differential equations (1) and boundary conditions (2), (3), i.e., they are a closed solution to the problem under consideration.

Research Results. As an example, we considered a radially polarized piezoceramic cylinder ($b = 0.02$ m, $R = 0.8$) of PZT–4 composition, having the following physical characteristics [10]: $\rho = 7500$ kg/m^3,

$\{C_{11}, C_{33}, C_{13}\} = \{13.9;\ 11.5;\ 7.43\}\times 10^{10}$ N/m^2, $\{e_{31}, e_{33}\} = \{-5.2;\ 15.1\}$ C/m^2,

$\{\gamma_{11}, \gamma_{33}\} = \{4.6;\ 3.9\}\times 10^5$ H/(m^2 ^{o}C), $\varepsilon_{33} = 5.62\times 10^{-9}$ Ф/м, $g_3 = 2\times 10^{-4}$ Кл/(m^2 ^{o}C),

$k = 3\times 10^6$ J/(m^3 ^{o}C), $\Lambda = 1.6$ W/(m ^{o}C), $\beta_{rel} = 5\times 10^{-5}$ c.

A temperature load acts on the inner surface ($r_* = a$) of the piezoceramic cylinder:

$$\omega_1^*(t_*) = T_{\max}\left[\sin\left(\frac{\pi}{2t_{\max}^*}t_*\right)H\left(t_{\max}^* - t_*\right) + H\left(t_* - t_{\max}^*\right)\right], \omega_2^*(t_*) = 0,$$

where $H(\tilde{t})$ —Heaviside step function ($H(\tilde{t}) = 1$ at $\tilde{t} \ge 0$, $H(\tilde{t}) = 0$ at $\tilde{t} < 0$), $T_{\max} = T_{\max}^* - T_0$, $T_{\max}^*, t_{\max}^*$— maximum value of the external temperature effect and the corresponding time in dimensional form ($T_{\max}^* = 373\ K\ (100\ ^0C), T_0 = 293\ K\ (20\ ^0C)$, $t_{\max}^* = 1$ s).

Figure 1 shows graphs of changes in functions $\Theta^*(r,t)$, $U(r,t)$, $\phi(r,t)$ along radial coordinate r at various points in time t. The numbers 1−3 respectively indicate the results obtained at the following time values: $t = t_{\max}, 4t_{\max}, 15t_{\max}$ ($t_{\max} = \dfrac{\Lambda_*}{kb^2}t_{\max}^*$).

Analysis of the calculation results allows us to draw the following conclusions:

− sufficiently large value of the coefficient of linear thermal expansion α_t of the piezoceramic material causes rapid heating of the cylinder;

− radial displacements on the inner cylindrical surface ($r = R$) at the first stage of the study ($t = t_{\max}$) take the greatest values, followed by a decrease over time. The reverse pattern is observed with respect to the displacements at $r = 1$;

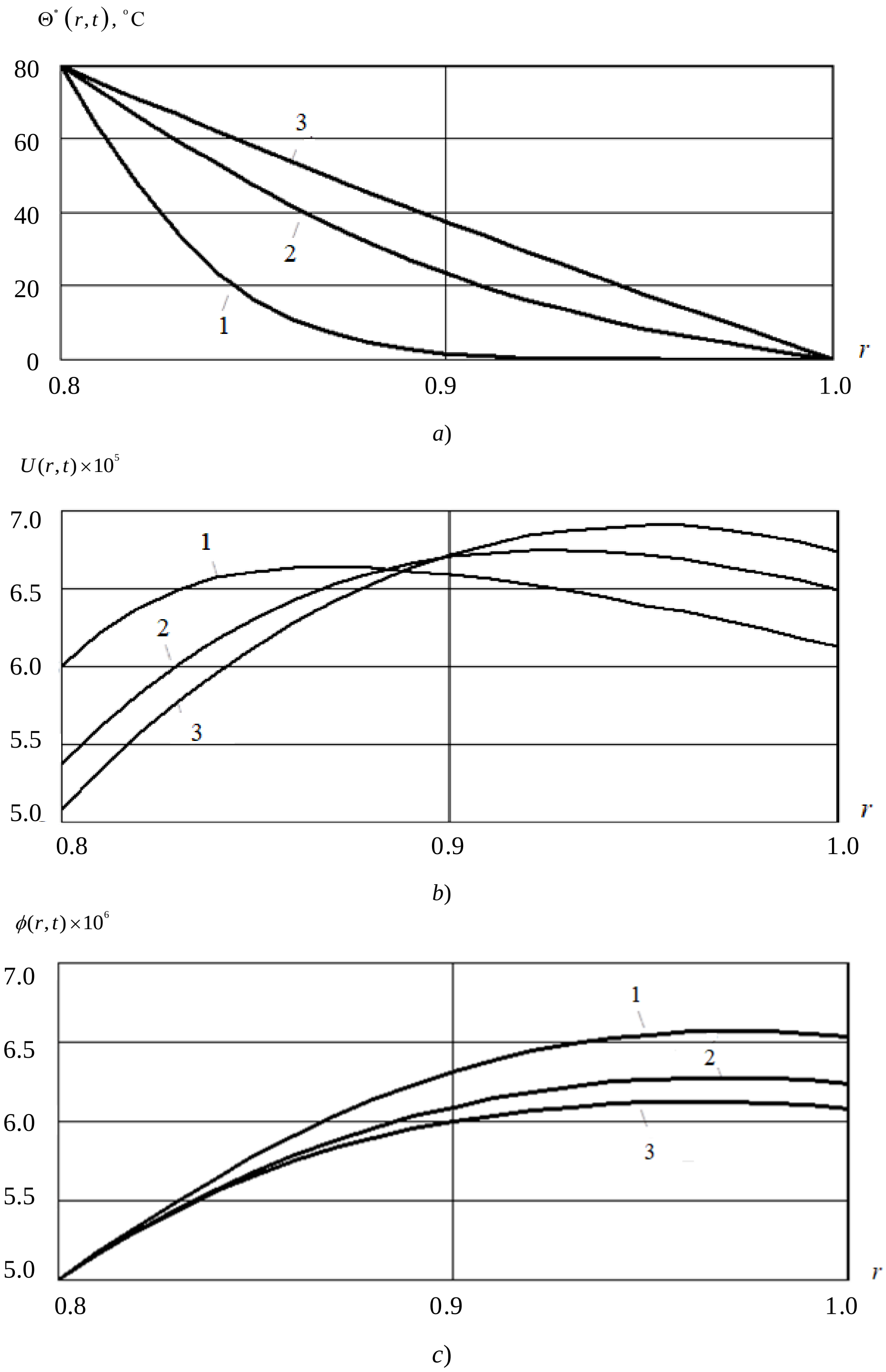

Fig. 1. Graphs of $\Theta^*(r,t)$, $U(r,t), \phi(r,t)$ changes along radial coordinate r at various points in time t $(1-t_{\max}, 2-4t_{\max}, 3-15t_{\max})$: *a* — $\Theta^*(r,t) \div r$; *b* — $U(r,t) \div r$; *c* — $\phi(r,t) \div r$

The degree of coupling of thermoelectroelastic fields is most conveniently analyzed using the coefficient $b_{6i} = \dfrac{\lambda^2}{\beta}\left(1 + a_4 + \dfrac{a_8}{a_7}\right)$ from equality (21). Here, a_4 determines the coupling of electroelastic fields, and $\dfrac{a_8}{a_7}$ — the effect of the rate of change in the volume of the body on its temperature field.

Figure 2 shows displacement graph $U(1,\ t)$ in time t taking into account (solid line) and without taking into account (dotted line) the induced electric field.

It should be noted that the preliminary polarization of piezoceramics causes the formation of a more “rigid” material ($a_4 = 0.353$) and, accordingly, a decrease in displacements during deformation of the cylinder.

The coupling of temperature and electroelastic fields in a piezoceramic cylinder can be neglected due to the small value

$$\frac{a_8}{a_7} = 1.8\times10^{-4} \ll 1.$$

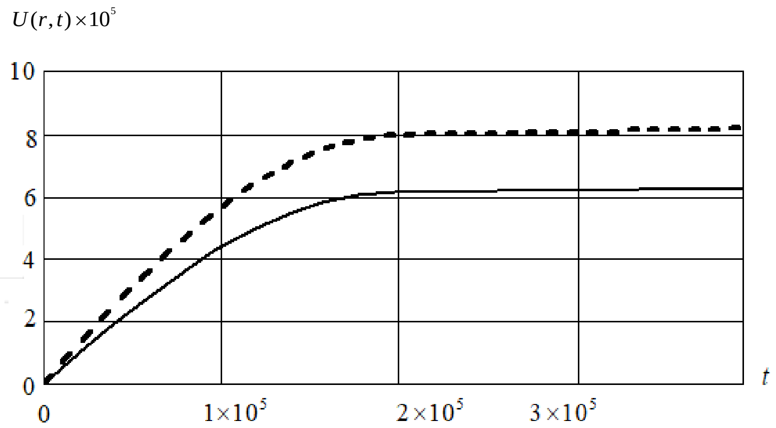

Fig. 2. Graph of change $U(1,\ t)$ in time t

(solid line — including the polarization; dotted line — without including the electric field)

Figure 3 shows graphs of changes in electrical voltage $V(t)$ over time, taking into account (solid line) and without taking into account (dotted line, $\beta_{rel} = 0$) the heat flow relaxation.

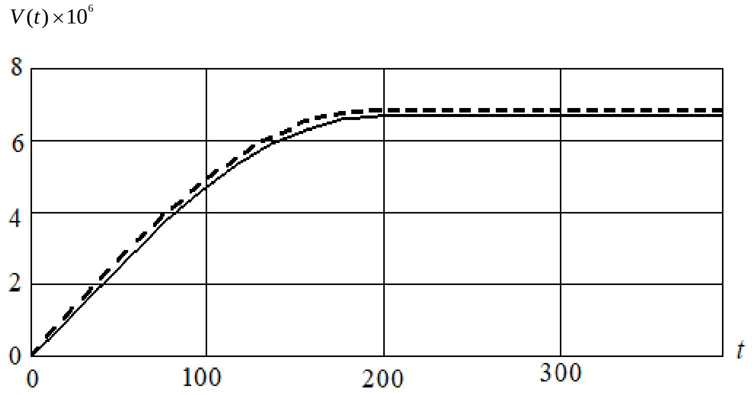

Fig. 3. Graph of change $V(t)$ over time t ($t^*_{\max} = 0.001\ s$, $t_{\max} = 196$)

The calculation results show that for the problem under consideration, the refined hyperbolic Lord-Shulman theory should be used at a high rate of change in the temperature load ($t^*_{\max} \geq 0.001$ s, $\left.\frac{d\omega_1^*(t_*)}{dt_*}\right|_{t=0} \geq 5.56\times10^5\ K/s$ and at lower speeds — the classical theory of thermoelectroelasticity ($\beta_{rel} = 0$).

Discussion and Conclusion. The constructed new closed solution to the coupled dynamic problem with satisfaction of the boundary conditions of thermal conductivity of the 1st kind made it possible to determine all the components of thermoelectroelastic fields in a long piezoceramic cylinder. The advantage of the presented calculation algorithm is that there is no need to approximate the temperature function when studying the equation of motion, in contrast to the uncoupled formulation of the problem. At the same time, the effect of the rate of change in the volume of a piezoceramic body on its temperature field can be neglected.

References

1. Kulchin YuN. Raspredelennye volokonno-opticheskie izmeritel'nye sistemy. Moscow: Fizmatgiz; 2001. 272 p. (In Russ.)

2. Lord HW, Shulman Y. A generalized dynamical theory of thermoelasticity. Journal of the Mechanics and Physics of Solids. 1967;15:299–309. https://doi.org/10.1016/0022-5096(67)90024-5

3. Green AE, Naghdi PM. Thermoelasticity without energy dissipation. Journal of Elasticity. 1993;31:189–208. https://doi.org/10.1007/BF00044969

4. Montanaro A. Some theorems of incremental thermoelectroelasticity. Archives of Mechanics. 2010;62:49–72.

5. Kulikov GM, Mamontov AA, Plotnikova SV. Coupled thermoelectroelastic stress analysis of piezoelectric shells. Composite Structures. 2015;124:65–76. https://doi.org/10.1016/j.compstruct.2014.12.045

6. Abbas IA, Zenkour AM. LS model on electro-magneto-thermoelastic response of an infinite functionally graded cylinder. Composite Structures. 2013;96:89–96. https://doi.org/10.1016/j.compstruct.2012.08.046

7. Vatulyan AO, Kiryutenko AYu, Nasedkin AV. Ploskie volny i fundamental'nye resheniya v lineinoi termoehlektrouprugosti. Journal of Applied Mechanics and Technical Physics. 1996;37:135–142. (In Russ.)

8. Vatulyan AO, Nesterov SA. The dynamic problem of thermoelectroelasticity for functionally graded layer. Computational Continuum Mechanics. 2017;10:117–126. https://doi.org/10.7242/1999-6691/2017.10.2.10

9. Saadatfar M, Razavi AS. Piezoelectric hollow cylinder with thermal gradient. Journal of Mechanical Science and Technology. 2009;23:45–53. https://doi.org/10.1007/s12206-008-1002-8

10. Khorsand M. Dynamic analysis of a functionally graded piezoelectric spherical shell under mechanical and thermal shocks. Mechanical Engineering Science. 2014;228:632–645. https://doi.org/10.1177/0954406213489445

11. Ishihara M, Ootao Y, Kameo Y, et al. Thermoelectroelastic response of a piezoelectric cylinder with D symmetry under axisymmetric mechanical and thermal loading. Mechanical Engineering Journal. 2017;4:16–00609. https://doi.org/10.1299/mej.16-00609

12. Shlyakhin DA, Kalmova MA. Uncoupled problem of Thermoelectroelasticity for a cylindrical shell. In: Proc. XXX Russian-Polish-Slovak Seminar Theoretical Foundation of Civil Engineering (RSP 2021). 2022;189:263–271. https://doi.org/10.1007/978-3-030-86001-1_31

13. Shlyakhin DA, Kalmova MA. The nonstationary thermoelectric elasticity problem for a long piezoceramic cylinder. PNPRU Mechanics Bulletin. 2021;2:181–190. https://doi.org/10.15593/perm.mech/2021.2.16

14. Senitskii YuE. Mnogokomponentnoe obobshchennoe konechnoe integral'noe preobrazovanie i ego prilozhenie k nestatsionarnym zadacham mekhaniki. Russian Mathematics (Iz. VUZ). 1991;4:57–63. (In Russ.)

15. Grinchenko VT, Ulitko AF, Shulga NA. Mekhanika svyazannykh polei v ehlementakh konstruktsii. Kiev: Naukova dumka; 1989. 279 p. (In Russ.)

Received 11.04.2022
Revised 04.05.2022
Accepted 09.05.2022

About the Authors:

Shlyakhin, Dmitriy A., Head of the Structural Mechanics, Engineering Geology, Bases and Foundations Department, Samara Polytech (244, Molodogvardeyskaya St., Samara, 443100, RF), Dr.Sci. (Eng.), associate professor, ResearcherID, ORCID, d-612-mit2009@yandex.ru

Kalmova, Mariya A., senior lecturer of the Structural Mechanics, Engineering Geology, Bases and Foundations Department, Samara Polytech (244, Molodogvardeyskaya St., Samara, 443100, RF), ResearcherID, ORCID, kalmova@inbox.ru

Claimed contributorship

D. A. Shlyakhin: academic advising; basic concept formulation; research objectives and tasks; computational analysis; formulation of conclusions. M. A. Kalmova: text preparation; analysis of the research results; the text revision; correction of the conclusions.

Conflict of interest statement

The authors do not have any conflict of interest.

All authors have read and approved the final manuscript.

MECHANICS

Check for updates

UDC 531.011:531.8

Original article

https://doi.org/10.23947/2687-1653-2022-22-2-91-98

Calculation of the Force and Kinematic Parameters of the Transfer Mechanism Based on a Twisted Arm Chain

Ivan R. Bondarenko ✉, **Artem A. Voloshkin**, **Victoria S. Perevuznik**, **Leonid A. Kovalev**

Belgorod State Technological University named after V. G. Shukhov, 46, Kostyukova St., Belgorod, Russian Federation

✉ ivanbond85@rambler.ru

Abstract

Introduction. The paper presents a brief kinematic analysis, as well as the application of D'Alembert's principle to finding the relationship between the force parameters in the transmission mechanism of a robotic manipulator constructed from a twisted arm chain. The use of this transfer mechanism can enhance the life of the arm actuator, the accuracy of its positioning, and increase the workload compared to the flexible linkage actuators (twisted strings). The work aimed at obtaining dependences between the displacements of circuit elements, as well as their force parameters required to monitor the control system operation of these devices.

Materials and Methods. In the course of solving the problem, an elementary segment (element) of the transmission chain was considered. To find the relationship between the loads in the element, the virtual displacement principle was used. When finding kinematic connections between displacements, a brief geometric analysis of the transmission chain element was carried out. To conduct a comparative analysis of the analytical dependences obtained, a simulation technique implemented on a graphical link model using the NX software package was applied.

Results. In the course of the study, we obtained dependences for determining the magnitude of the moment developed on the input link, depending on the external workload and its rotation angle, as well as for defining the linear displacement of the output link. A simulation model of the actuator was constructed, which can be applied in the dynamic study of the actuator mechanism, taking into account the inertia of the links.

Discussion and Conclusions. From the obtained analytical dependences, we determined the value of the angle of rotation of the input link of the mechanism element, at which the maximum torque value for a fixed workload on the output element was achieved, as well as the maximum linear displacement of the output link. The calculated values were in good agreement with similar values obtained from the results of the simulation experiment, which gave us the possibility of using analytical dependences in the formation of a robot control system. In addition, these dependences made it possible to provide the selection of actuators with the required force indicators.

Keywords: manipulators, flexible linkage, driven elementary segment, rigid arms, virtual displacement principle, torque, simulation experiment.

Acknowledgements: the authors would like to thank the editorial board and the reviewers for their advertency to the article – the research is done with the financial support from RFFI (grant no. 20−31−90134).

For citation: I. R. Bondarenko, A. A. Voloshkin, V. S. Perevuznik, L. A. Kovalev. Calculation of the force and kinematic parameters of the transfer mechanism based on a twisted arm chain. Advanced Engineering Research, 2022, vol. 22, no. 2, pp. 91–98. https://doi.org/10.23947/2687-1653-2022-22-2-91-98

Introduction. Recently, devices based on twisting cables or strings (threads) have begun to gain popularity. These inventions are universal in use and are in demand in various areas of robotics, specifically, in the manufacture of manipulators, grippers and exoskeletons[1] [1−4]. Drive structures based on twisting flexible elements have a number of advantages. These include the size of the device, ease of assembly and installation, versatility. As an example, a mechatronic twisted actuator, which is an electromechanical device with numerical control, is able to independently monitor the state of the working body based on data obtained from the shaft position sensor and the force sensor.

In the presented work, the authors carried out a kinematic and power analysis of the transmission mechanism of the actuator, built on the basis of a twisted arm chain. This design is intended to replace actuators using flexible transmission links, namely, twisting cables and strings.

The experimental device shown in Figure 1 consists of an electric motor and several strings oriented along the motor rotation axis. Strings connect the motor drive shaft to the simulated load generated by another electric actuator. Load control (linear actuator) enables to consider this system as a spring damper with adjustable parameters.

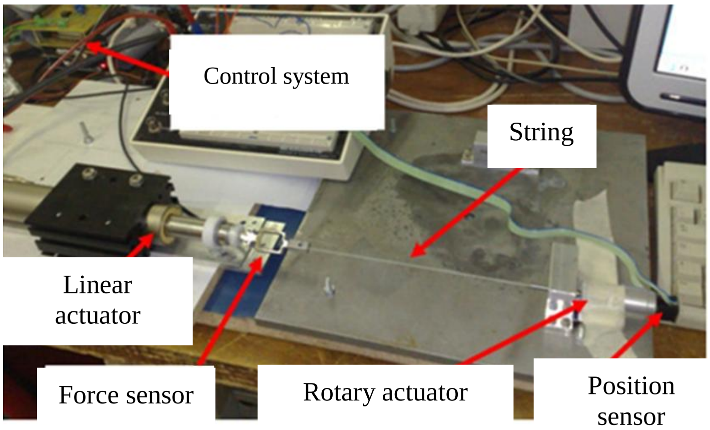

Fig. 1. Experimental setup [4]

Thanks to the string-twisted actuator, it was possible to place all the drives and motors in the prosthetic arm, given that all the main degrees of mobility of the arm were provided [5−8]. At the same time, the weakest point of the system is a flexible cable or string. Wear and stretching of the twisting string are the key disadvantages of this type of actuators.

An alternative solution to this problem may be the replacement of twisted strings or cables with a chain link system. Let us replace a fragment of twisted strings or cables with an element (segment) of rigid levers (rods) that pivotally connect two circles with radius *R* and centers O_1 and O_2 (Fig. 2 *a*). Input link *1* is supported by thrust bearing *6* and has the possibility of rotational movement relative to center O_1, located on Z_O axis. In this case, lower circle *4* (the output link) can make a translational movement along Z_O axis due to the presence of guide *5*. As a result of rotation of the upper circle, levers *3* and *4* perform spherical motion relative to link *1,* thereby changing distance *l* and moving workload *P* (Fig. 2 *b*, *c*).

[1] Gaponov II, Nedelchev SI. Mechatronic drive on twisted threads. RF Patent no. 2020144036, IPC F 16 H 35/00; 2021 (In Russ.)

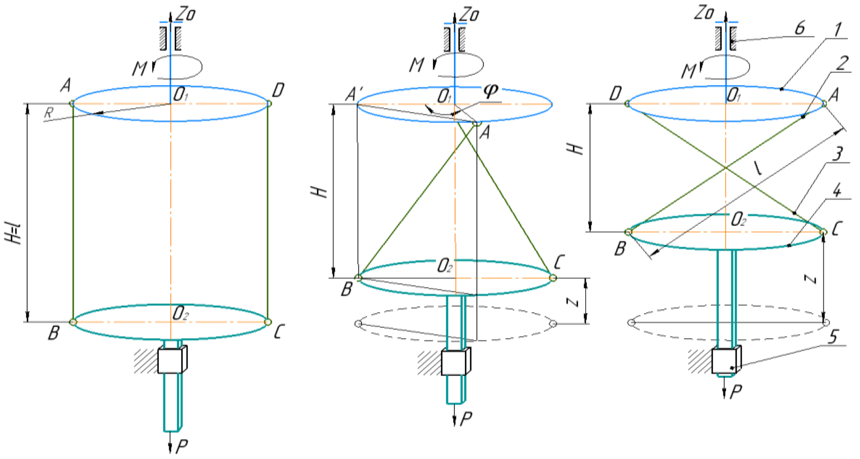

a) b) c)

Fig. 2. Diagram of the actuator chain segment: *a* — in initial position;
b — in intermediate position; *c* — in limit position

For the practical implementation of this design solution, it is required to have a control system based on a mathematical model of the actuator, which reflects the kinematic and power connections between the elements of the actuator chain.

This work aimed at finding kinematic and power connections in an elementary segment of the actuator chain.

Materials and Methods. We propose to find the solution to this problem using the virtual displacement principle [9], which enables to exclude internal forces in the links of the actuator element from consideration. Thus, the torque applied to the input link remains under consideration, as well as workload *P* applied to the output link. Considering the scheme shown in Fig. 4 *b*, we take rotation angle φ as the generalized coordinate for the input link, and linear displacement *z* — for the output link [10].

In accordance with the virtual displacement principle [11], we make up the equation of works:

$$M\delta\phi - P\delta z = 0\,, \qquad (1)$$

where $\delta\varphi$ — rotational virtual displacement of the input link, δz — linear virtual displacement of the output link.

Distance *H* between links *1* and *2* is related to the linear displacement *z* of link *2*, taking into account the length of the lever AB = *l*, dependence $H = l - z$. Then, taking into account the scheme shown in Figure 4 *b*, we can write:

$$l^2 - \left(2R\sin\left(\frac{\phi}{2}\right)\right)^2 = (l - z)^2\,.$$

Value z, depending on the rotation angle φ, is defined as:

$$z = l - \sqrt{l^2 - \left(2R\sin\left(\frac{\phi}{2}\right)\right)^2}\,. \qquad (2)$$

According to [11], the relationship between virtual displacements can be established as:

$$\delta z = \frac{df(\phi)}{d\phi}\delta\phi\,.$$

Then, taking derivative $\dfrac{df(\varphi)}{d\varphi}$ from (2) and performing the transformations, we get the dependence between the virtual displacements

$$\delta z = \frac{R^2\sin\phi}{\sqrt{l^2 - \left(2R\sin\left(\frac{\phi}{2}\right)\right)^2}}\delta\phi\,.$$

Substituting δz into the equation of works (1), we obtain:

$$M\,\delta\phi - P\frac{R^2\sin\phi}{\sqrt{l^2-\left(2R\sin\left(\frac{\phi}{2}\right)\right)^2}}\delta\phi = 0\,,$$

whence, through reducing by $\delta\varphi$, we express moment M as rotation angle function φ in the form:

$$M = \frac{PR^2\sin\phi}{\sqrt{l^2-\left(2R\sin\left(\frac{\phi}{2}\right)\right)^2}}\,. \qquad (3)$$

To evaluate the obtained analytical dependences of moment (3) developed at the input link and the linear displacement of the output link from the angle of rotation (2), a simulation experiment was carried out [12, 13], implemented in the NX Nastran software environment [14]. For this purpose, a three-dimensional solid-state model of a section of the actuator chain (Fig. 3 *a*), consisting of two sequentially connected elementary segments of the mechanism under study, was constructed. One of the segments of the actuator (Fig. 3 *b*) was used to perform the calculation with the following parameters*:* R = 12 mm, l = 54 mm. When constructing the model, spherical joints were presented in the form of toroidal joints, which made it possible to perform chain elements in the form of curved rings connected by rigid levers (Fig. 3). This design allows the levers to perform spherical movement. Since this connection provides the levers with the required degree of freedom, it can be considered corresponding to a spherical joint (Fig. 5 *c*).

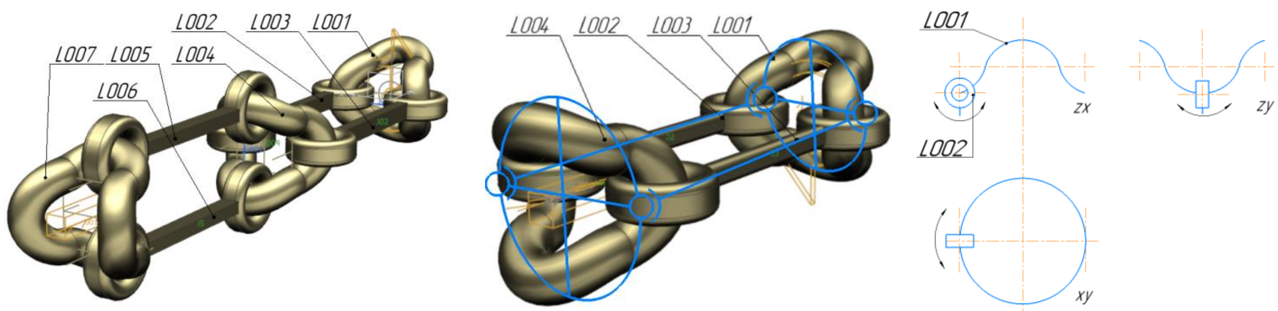

a) *b)* *c)*

Fig. 3. Three-dimensional solid models: *a* — chain section of two segments;
b — chain segment; *c* — projections of a complexly curved ring

In the developed three-dimensional model, kinematic connections were assigned, the centers of mass of the links were determined, and workload P = 100 N was set, after which the motion of the elementary segment of the actuator chain was simulated in NX Nastran [14, 15]. The parameters of the segment model are given in Table 1.

Table 1

Simulation Options

Connection number in simulation	Moment of inertia about each of the axes, kg · mm²			Mass, kg	Original coordinate of center of mass, mm			Name
	IX	IY	IZ		X	Y	Z	
L001	5.51	4.18	4.18	0.04	0	1.63	209	Curved ring of complex shape
L004					0	1.63	139.5	
L007					0	1.63	69.8	
L002	0.03	12.9	173.4	0.02	–0.03	–12.9	173.4	Lever
L003					–0.03	12.9	173.4	
L005					12.9	1.5	103.7	
L006					–12.9	1.5	103.7	

Research Results. In accordance with the obtained analytical dependences for the amount of linear displacement z, as well as torque *M*, a calculation was performed in the MathCAD environment, whose results are shown in Figure 4. The calculation was based on the following initial data: workload P = 100 N, radius of the input and output link R = 12 mm, lever length R = 12 mm, range of rotation angle φ of the input link within 0–180°.

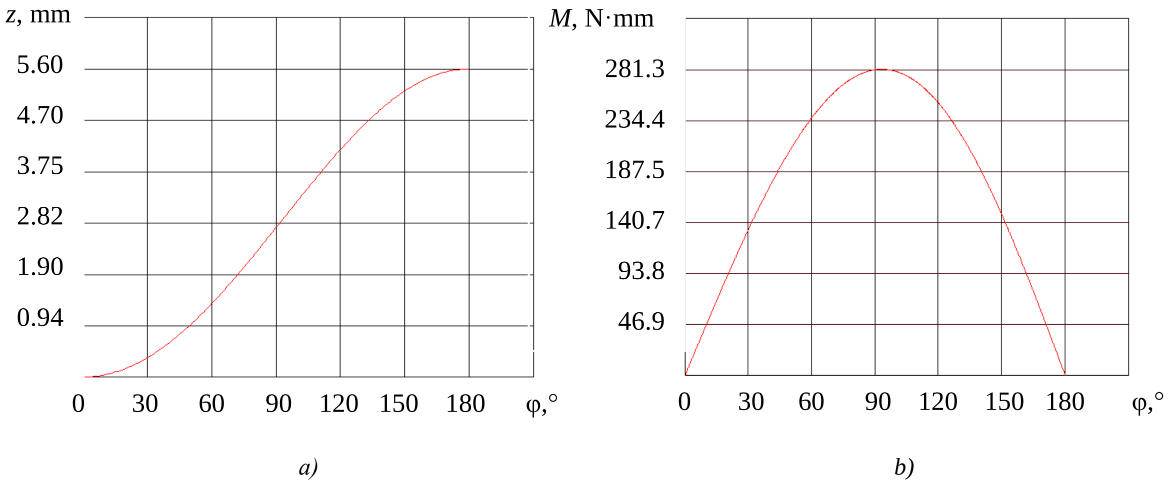

Fig. 4. Dependences of the studied values on the angle of rotation:

a — linear displacement of the output link; *b* — torque *M* at the input link

From the presented graphical dependences, it could be established that the maximum displacement amount was achieved at a rotation angle approaching 180 ° and is 5.6 mm, and the torque data peaked at 281.3 N·mm at rotation angle φ = 93°.

As a result of simulation modeling, a displacement schedule of output link L004 was obtained depending on the rotation of the actuator link L001 (Fig. 5). The movement of the elementary segment of the lever mechanism occurred until the right and left levers touched in the extreme position. Since the levers had volume, a complete rotation of the output link was impossible due to the side surface contact, which is also shown on the graph (Fig. 5). To achieve a complete rotation, it is required to change the structure of the lever to a more complex shape. Figure 6 shows the dependence of the torque when turning the chain segment of the calculated model by 180°.

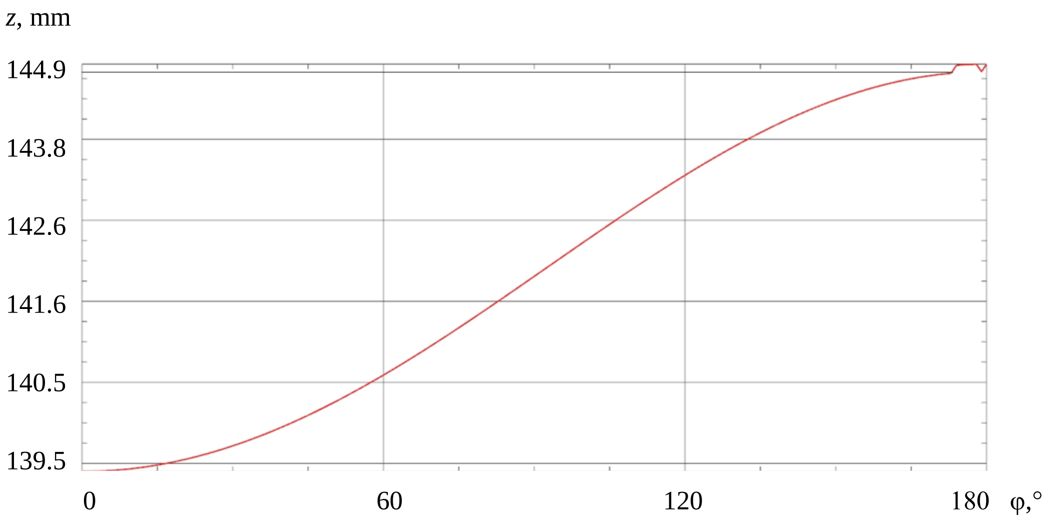

Fig. 5. Travel schedule of the output link in the relative coordinate system

Mechanics

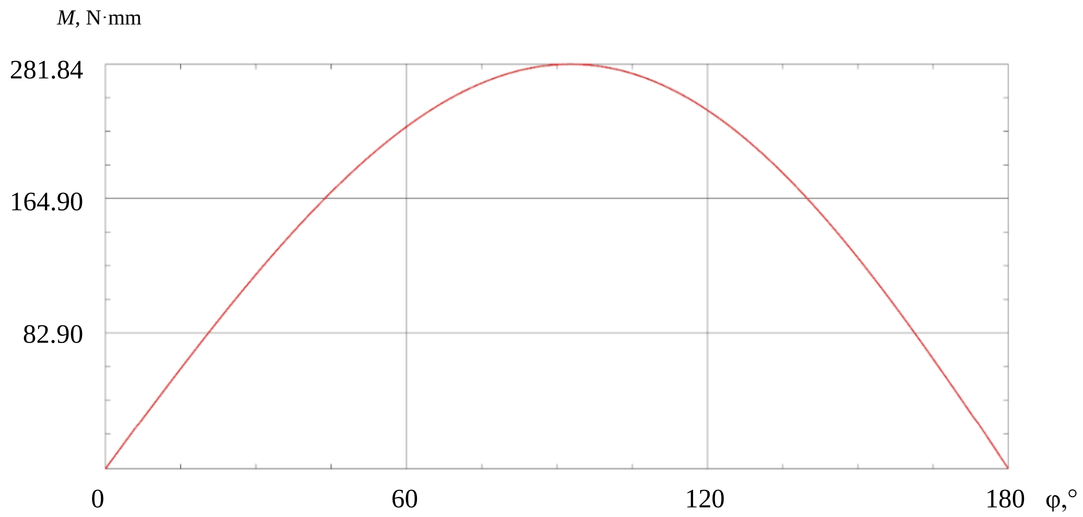

Fig. 6. Graph of torque change during the simulation experiment

The values of the studied parameters obtained through simulation (simulation experiment) differed from the values obtained theoretically by no more than 3 %.

Discussion and Conclusions. Within the framework of the presented work, kinematic and power analyses of the elementary segment of the actuator chain of the manipulator were carried out. The obtained analytical dependences made it possible to determine the maximum amount of linear displacement and the developed torque in the actuator segment. The results of the simulation experiment implemented in NX Nastran environment and the subsequent comparative analysis showed a good correspondence of the obtained analytical dependences with respect to the three-dimensional dynamic model of the object. This allowed us to conclude that the obtained analytical dependences could be used in the development of a control system for the actuators of the above-mentioned manipulator devices. The conducted studies showed that the chain of segments of the lever mechanism in question had good transmission properties and, with sufficient length, could replace the transmission based on twisting the string. However, the device of the studied transmission is more complex. Despite this, the transmission based on twisting a chain of segments has the advantage of being able to provide a greater number of operating cycles of the manipulator device while maintaining the required positioning accuracy and repeatability due to less deformations of the chain elements.

References

1. Gaponenko EV, Rybak LA, Holoshevskaya LR. Structural analysis and classification of robotic systems with driving mechanisms on the basis of cable elements. Bulletin of BSTU named after V.G. Shukhov. 2019;4:126–136.

2. Gaponov I, Popov D, Jee-Hwan Ryu. Twisted String Actuation Systems: A Study of the Mathematical Model and a Comparison of Twisted Strings. IEEE/ASME Transactions on Mechatronics. 2014;19:1331−1342. https://doi.org/10.1109/TMECH.2013.2280964

3. Hosseini M, Meattini R, Palli G, et al. A wearable robotic device based on twisted string actuation for rehabilitation and assistive applications. Journal of Robotics. 2017; 2017:3036468. http://dx.doi.org/10.1155/2017/3036468

4. Sonoda T, Godler I. Multi-fingered robotic hand employing strings transmission named “Twist Drive”. In: Proc. IEEE/RSJ Int. Conf. on Intelligent Robots and Systems. 2010. P. 2733–2738. http://dx.doi.org/10.1109/IROS.2010.5652886

5. Wuertz T, May Ch, Holz B, et al. The Twisted String Actuation System: Modeling and Control. IEEE/ASME Transactions on Mechatronics. 2010;18:1215−1220. http://dx.doi.org/10.1109/IROS.2010.5652886

6. Berselli G, Borghesan G, Brandi M, et al. Integrated mechatronic design for a new generation of robotic hands. IFAC Proceedings Volumes. 2009;42:8−13. https://doi.org/10.3182/20090909-4-JP-2010.00004

7. Palli G, Melchiorri C, Vassura G, et al. The DEXMART hand: Mechatronic design and experimental evaluation of synergy-based control for human-like grasping. The International Journal of Robotics Research. 2014;33:799–824. https://doi.org/10.1177/0278364913519897

8. Honh Liu, Peter Meusel, Gerd Hirzinger, et al. The modular multisensory DLR-HIT-Hand: Hardware and software architecture. IEEE/ASME Transactions on Mechatronics. 2008;13:461–469. https://doi.org/10.1109/TMECH.2008.2000826

9. Lapshin VV. On principle of virtual displacements. Herald of the Bauman Moscow State Technical University. 2012;45:59–64.

10. Vorobieva NS, Zhoga VV, Dyashkin-Titov VV, et al. Development of the base of models of the parallel and sequence structure manipulator. Izvestiya SFedU. Engineering Sciences. 2017;194:143–152.

11. Mikhailenko NI, Zhivago EYa. Primenenie printsipa vozmozhnykh peremeshchenii k resheniyu tekhnicheskikh zadach. Vestnik SibGIU. 2013;3:58–63. (In Russ.)

12. Vdovin DS,Chichekin IV, Pozdnyakov TD. Virtual test bench for determining loads affecting an automobile steering system. Engineering Journal: Science and Innovation. 2017;68:1–12.

13. Čepon G, Manin L, Boltežar M. Introduction of damping into the flexible multibody belt-drive model: A numerical and experimental investigation. Journal of Sound and Vibration. 2009;324:283–296. https://doi.org/10.1016/j.jsv.2009.02.001

14. Malaka J, Hetmańczyk M. Generating numerical multibody model of toothed belt in technological machines with Siemens NX. International Journal of Modern Manufacturing Technologies. Special Issue. 2021;XIII:87–95. https://doi.org/10.54684/ijmmt.2021.13.3.87

15. Nuzhnyy AM, Verkoshanskiy MV, Grebennikoba NI, et al. Parametrization of solid models using NX Open. Proceedings of VSUET. 2019;15:24–27.

Received 04.05.2022

Revised 26.05.2022

Accepted for publication 06.06.2022

About the Authors:

Bondarenko, Ivan R., associate professor of the Engineering Mechanics and Strength of Materials Department, Belgorod State Technological University named after V.G. Shukhov (46, Kostyukova St., Belgorod, 308012, RF), ORCID, ivanbond85@rambler.ru

Voloshkin, Artem A., research engineer, Belgorod State Technological University named after V.G. Shukhov (46, Kostyukova St., Belgorod, 308012, RF), ORCID, voloshkin.artem.a@gmail.com

Perevuznik, Victoria S., junior research assistant, Belgorod State Technological University named after V. G. Shukhov (46, Kostyukova St., Belgorod, 308012, RF), ScopusID, ORCID, viktorija.kuzmina@yandex.ru

Kovalev, Leonid A., associate professor of the Engineering Mechanics and Strength of Materials Department, Belgorod State Technological University named after V. G. Shukhov (46, Kostyukova St., Belgorod, 308012, RF), ORCID, lkovalev55@yandex.ru

Claimed contributorship

I. R. Bondarenko: academic advising; research objectives and tasks; obtaining analytic dependences; computational analysis; text preparation; formulation of conclusions. A. A. Voloshkin: development of a digital model; simulation of model movement in CAD system; simulation analysis; correction of the conclusions. L. A. Kovalev: analysis of the research results; the text revision; correction of the conclusions. V. S. Perevuznik: basic concept formulation; text preparation; formulation of conclusions.

Conflict of interest statement

The authors do not have any conflict of interest.

All authors have read and approved the final manuscript.

MACHINE BUILDING AND MACHINE SCIENCE

UDC 621.914.1

https://doi.org/10.23947/2687-1653-2022-22-2-99-106

Original article

Study of the Effect of Cutting Modes on Output Parameters under High-speed Steel Turn-milling

Dmitriy A. Matlygin ✉, Andrey V. Savilov , Aleksey S. Pyatykh, Sergey A. Timofeev

Irkutsk National Research Technical University, 83, Lermontov St., Irkutsk, Russian Federation

✉ gmatlygin@mail.ru

Abstract

Introduction. The article elucidates increasing the efficiency of turn-milling of powdered metal high-speed steel products. Turn-milling can be used as an alternative to the traditional turning method. The article describes advantages of the turn-milling method. A review of studies devoted to improving the surface quality of parts when turning by milling is given. The work aims at determining the effect of cutting modes on the surface roughness by the orthogonal turning method through milling powdered high-speed steel with a monolithic cutter.

Materials and Methods. Statistical analysis methods based on the creation of a mathematical model for predicting microgeometric deviations of the treated surface were used. An experimental research method was applied to verify the adequacy of the mathematical model. The experiment was planned according to the non-composite design proposed by Box and Behnken. The experiment was carried out on a turning machining center with a driving tool. Powdered high-speed steel BÖHLER S390 MICROCLEAN was used as sample material for the experiment. A monolithic carbide milling cutter served as a cutting tool. During the experiment, the cutting speed, milling width, and feed per tooth varied. The roughness of the treated surface was measured by a contact profilometer.

Results. A mathematical model of the formation of surface roughness depending on the processing modes was developed. During the experiments, the effect of cutting speed, tool feed, and radial cutting depth on the roughness of the treated surface was determined. It was established that the dependence of roughness on feed had a linear character over the entire investigated range of cutting modes. In turn, the dependence of roughness on the cutting speed and cutting width had a parabolic character. The results obtained allowed us to achieve the roughness of the treated surface Ra = 1.85 without reducing the processing performance.

Discussion and Conclusions. The developed mathematical model reflects the impact of cutting modes on the surface roughness when turning high-speed steel with a monolithic cutter. The results of the conducted research can be used to determine the optimal cutting modes that provide a given surface quality in the manufacture of real parts under the production conditions. It is recommended to continue the research with the control of additional output parameters, such as temperature and vibration. Reducing the effect of regenerative self-oscillations on the roughness of the treated surface can be reached through assigning the cutting modes based on the results of a modal analysis of the process system.

Keywords: turn-milling, carbide cutter, roughness, high-speed steel, cutting simulation.

Acknowledgements: the authors would like to thank the editors and reviewers for their careful attention to the article and for the comments, which made it possible to improve its quality.

For citation: G. V. Matlygin, A. V. Savilov, A. S. Pyatykh, S. A. Timofeev. Study of the effect of cutting modes on output parameters under high-speed steel turn-milling. Advanced Engineering Research, 2022, vol. 22, no. 2, pp. 99–106. https://doi.org/10.23947/2687-1653-2022-22-2-99-106

Introduction. An alternative to the classical cutting process is turn-milling. The first attempts to describe this type of processing and its practical application took place in the first half of the twentieth century. In 1948, G. I. Granovsky described the kinematics of processing a cylindrical rotating part using a milling cutter [1]. In 1964, A. O. Ehtin described various methods of turn-milling, including milling with a tool with an axis parallel to the axis of the part, and milling with a cylindrical cutter with circular and tangential feeds [2]. Schultz and Spur are considered to be the founders of the practical application of this method. They divided turn-milling operations into two groups: orthogonal and tangential [3]. A significant contribution to the study of this technique was made by U. Karaguzel, M. Bakkal, and E. Budak, who studied the mechanics and thermal aspects of turn-milling. They also developed models to test the geometry of the process, kinematics and mechanics, and the quality of machined parts in orthogonal and tangential turn-milling operations [4].

When implementing the turn-milling operation, a challenging issue is to obtain high surface quality, first of all, to reduce roughness. The analysis of publications allowed us to identify the main directions in the study of ways to achieve high surface quality:

– study of the effect of eccentricity [5];

– determination of the profile of the cutting tool with multi-faceted indexable inserts with round and rounded cutting edges [6];

– study of the effect of temperature in the cutting zone [7];

– prediction of the wear resistance of the cutting edge when using the turn-milling operation [8].

It should be noted that in the above works, traditional structural steels were used as the materials under study. Investigations on high-speed steel, including those obtained by powder metallurgy, are not common. This limits the application of the advantages of turn-milling for the manufacture of rotating cutting tools [9]. This direction of machining can be attributed to the area, where turn-milling can give the greatest economic effect.

The surface quality is affected by the cutting tool used. In particular, the application of end mills with replaceable polyhedral plates does not always provide the required surface roughness [10]. It is important to note that the considered experimental part of the research was carried out on multi-purpose machines. However, turn-milling can also be used on turning machining centers with driven tools [11].

This work aimed at determining the effect of cutting modes on the surface roughness in the orthogonal method of turn-milling powdered high-speed steel with a solid cutter.

Materials and Methods. The experiment was carried out on a turning machining center with DMG NEF 400 drive tool (Fig. 1).

Fig. 1. Treatment zone during the experiment

Powdered high-speed steel BÖHLER S390 MICROCLEAN[1] was used as the test material. The workpiece was a cylinder measuring 88×300 mm that was fixed in a three-jaw hydraulic chuck with preloaded center mounted in the tailstock of the machine (Fig. 2). Monolithic carbide milling cutter YG-1 GM999 12(R3)×12×32×75, z = 5 was used as a cutting tool. The treatment was carried out without the use of coolant. The roughness of the treated surface was measured using a stationary Taylor&Hobson Form Talysurf 200 profilometer.

Chemical composition of BÖHLER S390 MICROCLEAN steel:

1.64 % C; 0.60 % Si; 0.30 % Mn; 4.80 % Cr; 2.00 % Mo; 4.80 % V; 10.40 % W; 8.00 % Co.

Processing characteristics of BÖHLER S390 MICROCLEAN steel, presented in a scoring system of 5 points corresponding to the maximum values of the properties of this group of steels:

- compressive strength — 4;
- grindability — 3;
- hardenability — 4;
- viscosity — 4;
- wear resistance — 4.

[1]M390–BÖHLER Russia. www.bohlernn.ru URL: https://www.bohlernn.ru/ru/products/m390/ (accessed: 14.12.2021).

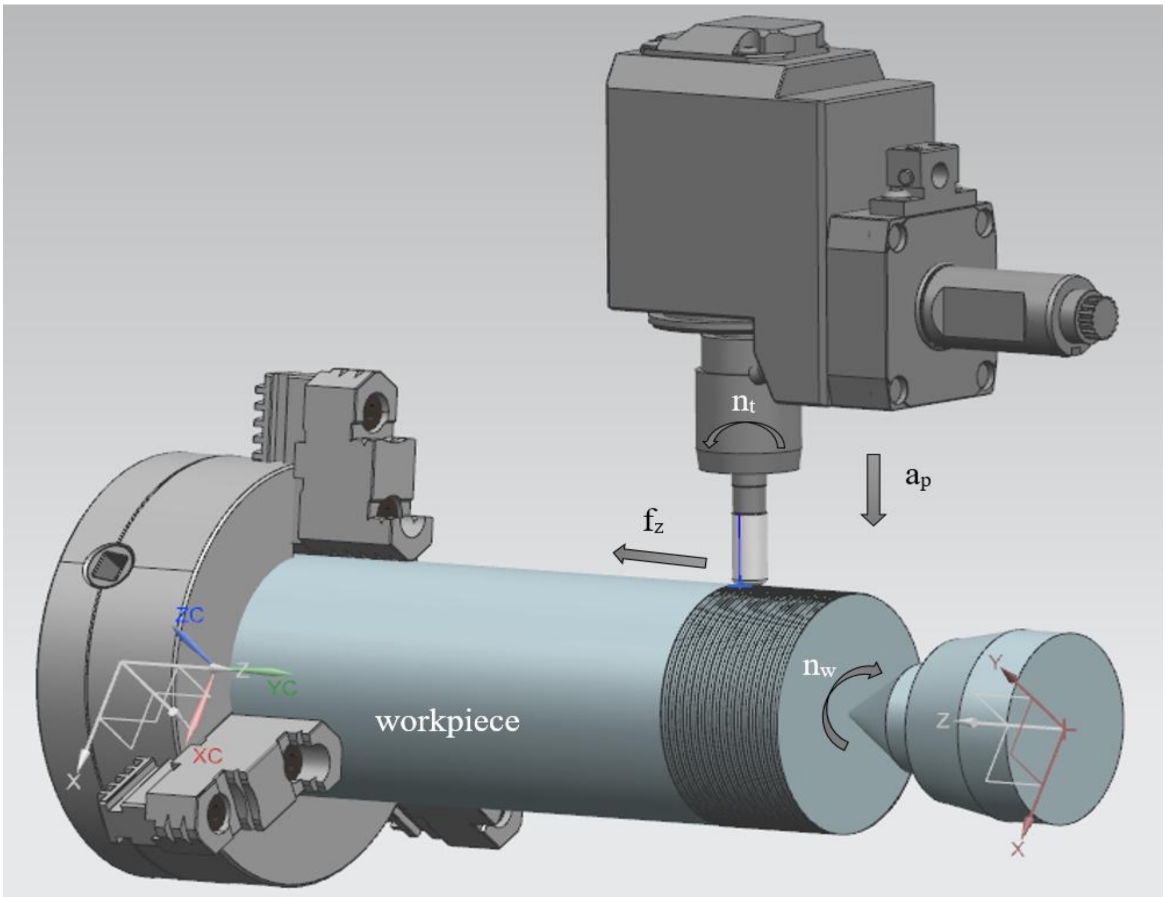

Fig. 2. Scheme of orthogonal processing with YG-1 GMG19910 monolithic milling cutter

The mathematical model of the deviation of the surface roughness can be presented by the equation [11]:

$$\ln Ra = \ln D + c_1 \cdot \ln f_z + c_{11} \cdot \ln f_z^2 + c_2 \cdot \ln V_c + c_{22} \cdot \ln V_c^2 + c_3 \cdot \ln a_e + c_{33} \cdot \ln a_e^2,$$

where f_z — feed, mm/tooth; V_c — cutting speed, m/min; a_e — cutting width, mm.

Rename this expression as follows:

$$y_1 = g_0 \cdot x_0 + g_1 \cdot x_1 + g_{11} \cdot x_1^2 + g_2 \cdot x_2 + g_{22} \cdot x_2^2 + g_3 \cdot x_3 + g_{33} \cdot x_3^2,$$

where $y_1 = \ln Ra$; x_0 — dummy variable; x_1, x_2, x_3 — coded factor values; g_0, g_1, g_2, g_3 — constant coefficients.

Encoding of variables is carried out according to the following relations:

$$x_1 = \frac{2(\ln f_z + \ln f_{z_{max}})}{\ln f_{z_{max}} - \ln f_{z_{min}}} + 1;$$

$$x_2 = \frac{2(\ln V_c + \ln V_{c_{max}})}{\ln V_{c_{max}} - \ln V_{c_{min}}} + 1;$$

$$x_3 = \frac{2(\ln a_e + \ln a_{e_{max}})}{\ln a_{e_{max}} - \ln a_{e_{min}}} + 1,$$

where $f_{z_{max}}, V_{c_{max}}, a_{e_{max}}$ — upper levels of factors; $f_{z_{min}}, V_{c_{min}}, a_{e_{min}}$ — lower levels of factors; $f_{z_0}, V_{c_0}, a_{e_0}$ — main levels of factors. The values of these parameters are presented in Table 1.

Table 1

Values of experiment factor levels

Factors	Code	Lower level (-1)	Main level (0)	Upper level (+1)
f_z, mm/tooth	x_1	0.04	0.08	0.12
V_c, m/min	x_2	80	90	100
a_e, mm	x_3	1	2	3

The experiment was planned according to the non-composite design proposed by Box and Behnken. This plan is a sampling of rows from a complete 3^k type factor experiment. It includes 15 experiments. The matrix of the plan is shown in Table 2.

Table 2

Experiment Design Results Matrix

No	Factors										Output parameter
	x_0	x_1	x_2	x_3	$x_1 \cdot x_2$	$x_1 \cdot x_3$	$x_2 \cdot x_3$	x_1^2	x_2^2	x_3^2	Ra, μm
1	1	-1	-1	0	1	0	0	1	1	0	0.9487
2	1	1	-1	0	-1	0	0	1	1	0	1.5583
3	1	-1	1	0	-1	0	0	1	1	0	1.2183
4	1	1	1	0	1	0	0	1	1	0	1.7555
5	1	-1	0	-1	0	1	0	1	0	1	1.5674
6	1	1	0	-1	0	-1	0	1	0	1	1.9084
7	1	-1	0	1	0	-1	0	1	0	1	1.5198
8	1	1	0	1	0	1	0	1	0	1	1.9505
9	1	0	-1	-1	0	0	1	0	1	1	1.8912
10	1	0	1	-1	0	0	-1	0	1	1	1.0914
11	1	0	-1	1	0	0	-1	0	1	1	1.6132
12	1	0	1	1	0	0	1	0	1	1	1.7664
13	1	0	0	0	0	0	0	0	0	0	1.5668
14	1	0	0	0	0	0	0	0	0	0	1.5081
15	1	0	0	0	0	0	0	0	0	0	1.5046

The coefficient vector is determined from the formula:

$$B = (X^T X)^{-1} X^T Y.$$

Variances $S^2(b_j)$ of the regression coefficient are found from the expression:

$$S^2(b_j) = c_{ii} S_y^2,$$

where c_{ii} — diagonal elements of matrix XX^{-1}; S^2y — empirical regression variance.

The average value and variance are determined by the vector of experiments at the center of the plan.

Average value:

$$y = \frac{\sum_{i=0}^{2} Y_{u_i}}{3},$$

where Y_u — vector of response function values in the center of the plan.

Dispersion:

$$S_y^2 = \frac{\sum_{i=0}^{2} (Y_{u_i} - y)^2}{2}.$$

Based on the results of experiments carried out according to the plan (Table 2), it is possible to determine the constant coefficients of the equation:

$$y = g_0 \cdot x_0 + g_1 \cdot x_1 + g_2 \cdot x_2 + g_3 \cdot x_3 + g_{12} \cdot x_1 \cdot x_2 + g_{13} \cdot x_1 \cdot x_3 + g_{23} \cdot x_2 \cdot x_3$$
$$+ g_{11} \cdot x_1^2 + g_{22} \cdot x_2^2 + g_{33} \cdot x_3^2;$$

$$g_0 = \frac{1}{n_0} \sum_{u=1}^{n_0} y_{0u} ;$$

$$g_i = A \sum_{j=1}^{N} x_{ij} y_j ;$$

$$g_{il} = D \sum_{j=1}^{N} x_{ij} x_{lj} y_j ;$$

$$g_3 = B\sum_{u=1}^{N} x_{ij}^2 y_j + C\sum_{i=1}^{k}\sum_{j=1}^{N} x_{ij}^2 y_j - \frac{1}{p\cdot n_0}\sum_{u=1}^{n_0} y_{0u},$$

where n_0 — number of experiments in the center of the plan; u — number of parallel experiments in the center of the plan; y_{0u} — value of the response function in the u-th experiment; N — number of experiments in the planning matrix; j — number of experiments in the planning matrix; i, l — factor numbers; x_{ij}, x_{lj} — coded values of the i-th and l-the number of factors in the j-th experiment; y_j — value of the response function in the j-th experiment.

It follows from this: $g_0 = 1.388$; $g_1 = 0.24$; $g_2 = -0.022$; $g_3 = 0.268$; $g_{11} = 2.413$; $g_{22} = 2.267$; $g_{33} = 3.072$.

Thus, the model of the dependence of the deviation of the surface roughness on the processing parameters and the cutting width will have the form:

$$Ra = 1.388 + 2.413\cdot f_z^2 - 0.24\cdot f_z.$$

Research Results. The dependences of the surface roughness on the cutting modes are shown in Figure 3.

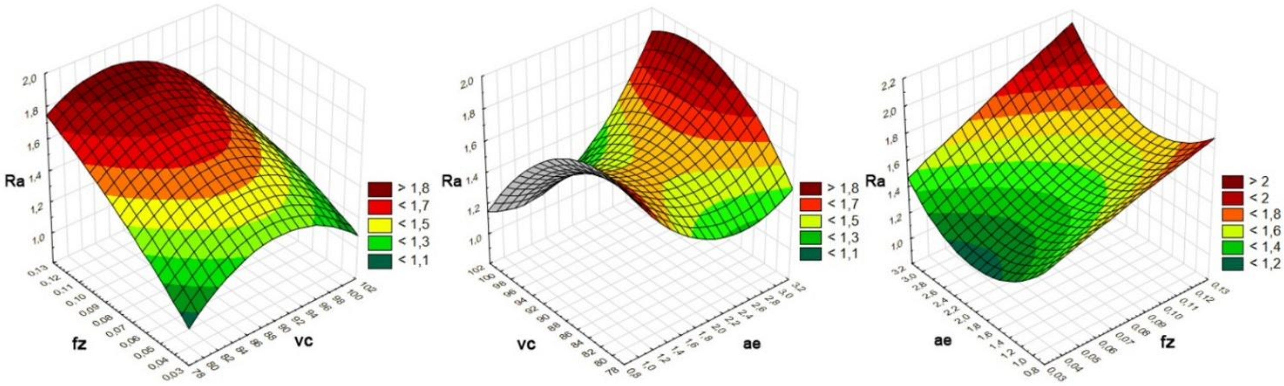

a) *b*) *c*)

Fig. 3. Dependences of the deviation of roughness parameter R_a: *a* — on feed to tooth f_z and on cutting speed V_c; *b* — on cutting speed V_c and milling width a_e; *c* — on milling width a_e and feed to tooth f_z

The analysis of the obtained results shows that the dependence of roughness on feed has a linear character over the entire investigated range of cutting modes (Fig. 3 *a*, *b*). At the same time, with an increase in feed, the roughness increases proportionally, which is consistent with the basic concepts of the cutting theory. The maximum value of the roughness parameter R_a is 1.85 μm, which corresponds to the most common requirements for finishing machining in mechanical engineering.

The dependence of roughness on the cutting speed V_c (Fig. 3 *a*, *b*) has a parabolic character with maximum roughness values in the range of cutting speeds of 90–95 m/min. This can be explained by the fact that in the specified range of cutting speeds, there is an effect of built-up material on the cutting edge. To verify this hypothesis, it is required to conduct additional studies with temperature control in the cutting zone and the use of a high-speed video camera to monitor the process of chip formation and possible build-up formation.

The impact of milling width a_e on the surface roughness is also parabolic in nature (Fig. 3 *b*, *c*), but the maximum values of roughness are reached at a_e = 0.25 mm and a_e = 3 mm, and the minimum value is at a_e = 1.8–2.2 mm. It can be assumed that in the specified cutting width range, the treatment process is less affected by regenerative vibrations, which also depend on the design and geometric parameters of the cutting tool.

As a result, it can be stated that with the established cutting modes, it was possible to achieve a surface roughness no higher than R_a = 1.85 without loss of process performance.

Discussion and Conclusions. A mathematical model has been developed reflecting the effect of cutting modes on the surface roughness through turn-milling of high-speed steel with a monolithic cutter. The results of the conducted research can be used to determine the optimal cutting conditions that provide a given surface quality in the manufacture of real parts under production conditions.

It is recommended to conduct additional studies with temperature control in the cutting area and vibrations. The assignment of cutting modes should be carried out on the basis of the results of the modal analysis of the technological system to reduce the effect of regenerative self-oscillations on the roughness of the treated surface.

References

1. Granovsky GI. Kinematika rezaniya. Moscow: Mashgiz; 1948. 323 p. (In Russ.)

2. Ehtin AO. Kinematicheskii analiz metodov obrabotki metallov rezaniem. Moscow: Mashinostroenie; 1964. 324 p. (In Russ.)

3. Schulz H, Lehmann T. Kräfte und Antriebsleistungen beim Ortagonalen Drehfräsen (Forces and Drive Powers in Orthogonal Turn-Milling). Werkstatt und Betrieb. 1990;123:921–924.

4. Karaguzel U, Bakkal M, Budak E. Process modeling of turn-milling using analytical approach. Procedia CIRP. 2012;4:131–139. https://doi.org/10.1016/j.procir.2012.10.024

5. Lida Zhu, Zenghui Jiang, Jiashun Shi, et al. An overview of turn-milling technology. The International Journal of Advanced Manufacturing Technology. 2015;81:493–505. https://doi.org/10.1007/s00170-015-7187-y

6. Harry Otalora-Ortega, Patxi Aristimuño Osoro, Pedro Arrazola Arriola. Uncut chip geometry determination for cutting forces prediction in orthogonal turn-milling operations considering the tool profile and eccentricity. International Journal of Mechanical Sciences. 2021;198:106351. https://doi.org/10.1016/j.ijmecsci.2021.106351

7. Koji Shimanuki, Akira Hosokawa, Tomohiro Koyano, et al. Study on the relationship between material removal rate and tool flank temperature in orthogonal turn-milling. Journal of Advanced Mechanical Design, Systems, and Manufacturing. 2021;15:JAMDSM0043. https://doi.org/10.1299/jamdsm.2021jamdsm0043

8. Felusiak-Czyryca A, Madajewski M, Twardowski P, et al. Cutting Forces during Inconel 718 Orthogonal Turn-Milling. Materials. 2021;14:6152. https://doi.org/10.3390/ma14206152

9. Matlygin G, Savilov A, Zarak T. Analysis of progressive machining technologies for rotating cutting tools. iPolytech Journal. 2020;24:498–513. https://doi.org/10.21285/1814-3520-2020-3-498-513

10. Pyatykh A. Improving effective output and hole processing quality based on cutting process dynamics estimation. Proceedings of Irkutsk State Technical University. 2018;140:67-81. https://doi.org/10.21285/1814-3520-2018-9-67-81

11. Matlygin G, Savilov A, Pyatykh A, et al. The Impact of Cutting Modes on the Output Turn-Milling Parameters for High-Speed Steel. Key Engineering Materials. 2022;910:129–137. https://doi.org/10.4028/p-n6exa0

Received 21.04.2022

Revised 17.05.2022

Accepted 24.05.2022

About the Authors:

Matlygin, Georgy V., postgraduate of the Technology and Equipment for Machine-Building Production Department, Irkutsk National Research Technical University (83, Lermontov St., Irkutsk, 664074, RF), ResearcherID, ScopusID, ORCID, gmatlygin@mail.ru

Savilov, Andrey V., associate professor of the Technology and Equipment for Machine-Building Production Department, Irkutsk National Research Technical University (83, Lermontov St., Irkutsk, 664074, RF), Cand.Sci. (Eng.), associate professor, ResearcherID, ScopusID, ORCID, saw@istu.edu

Pyatykh, Aleksey S., associate professor of the Technology and Equipment for Machine-Building Production Department, Irkutsk National Research Technical University (83, Lermontov St., Irkutsk, 664074, RF), Cand.Sci. (Eng.), associate professor, ResearcherID, ScopusID, ORCID, pyatykhas@ex.istu.edu

Timofeev, Sergey A., Junior Research Fellow of the Technology and Equipment for Machine-Building Production Department, Irkutsk National Research Technical University (83, Lermontov St., Irkutsk, 664074, RF), ResearcherID, ScopusID, ORCID, sevans@istu.edu

Claimed contributorship

G. V. Matlygin, A. V. Savilov: basic concept formulation; research objectives and tasks; цели и задачи исследования, анализ существующих подходов; text preparation; formulation of conclusions. A. S. Pyaiykh, S. A. Timofeev: conducting research; analysis of research results.

Conflict of interest statement

The authors do not have any conflict of interest.

All authors have read and approved the final manuscript

MACHINE BUILDING AND MACHINE SCIENCE

Check for updates

UDC 678.549

https://doi.org/10.23947/2687-1653-2022-22-2-107-115

Original article

Using the Finite Element Method to Simulate a Carbon Fiber Reinforced Polymer Pressure Vessel

Imad Rizakalla Antipas ✉, **Alexey G. Dyachenko**

Don State Technical University, 1, Gagarin sq., Rostov-on-Don, Russian Federation

✉ Imad.antypas@mail.ru

Abstract

Introduction. Over the past decade, global demand for pressure vessels has increased significantly, specifically in such industries as aviation, space, chemical, and oil and gas. Being under the constant impact of high internal pressure, the walls of the tanks are under increased stress, which can cause their sudden destruction. To eliminate this probability and improve the strength characteristics, the tanks are made in the form of metal cylinders with an internal coating of composite material consisting of resin reinforced with carbon fibers. This article aimed at studying the effect of the angle of inclination of carbon fiber on cylindrical tanks and determining the maximum destructive pressure using the finite element method of ANSYS program.

Materials and Methods. Using the ANSYS program, a finite element model of a tank was created. It has a central part, which is a metal cylinder with an internal coating of composite material consisting of polymer reinforced with carbon fibers. At the ends of the tank, spiral wound hemispheres were placed. In these studies, SHELL 99 was used to model the layered composite material. The Tsai-Wu theory was used to determine the pressure tank failure criterion.

Results. The cylindrical tank model was calculated for two types of fiber winding paths: annular and spiral, at different angles of their inclination. The results of the pressure value analysis for different fiber inclination angles showed that, starting from the angle value of 0° and up to 45°, it increased, and then, up to the angle value of 65°, it began to decrease. The critical pressure value for a carbon fiber reinforced tank was 207 MPa, which was obtained at a fiber angle of 45°.

Discussion and Conclusion. Analysis of the studies showed that at a fiber inclination angle of 45°, the value of the maximum stress turned out to be the smallest, and the maximum possible destructive pressure at the same angle was 207 MPa. It follows, that the optimal fiber orientation angle to provide safe operation of the high-pressure tank is ± 45°, and the carbon fiber tank, calculated at the same fiber winding angle, has the maximum strength value.

Keywords: high-pressure tank, computer model, winding angle, composite coating, carbon fiber, polymer binder.

Acknowledgements: the authors would like to thank the editorial board and the reviewers for their advertency to the article and the comments, which contributed to its quality.

For citation: I. R. Antypas, A. G. Dyachenko. Using the Finite Element Method to Simulate a Carbon Fiber Reinforced Polymer Pressure Vessel. Advanced Engineering Research, 2022, vol. 22, no. 2, pp. 107–115.

https://doi.org/10.23947/2687-1653-2022-22-2-107-115

Introduction. The use of high-pressure carbon fiber vessels has found widespread use in various industries due to its distinctive properties, such as low weight and high strength. Therefore, recently the demand for such vessels has increased significantly in cases where weight plays a major role [1, 2].

The critical areas of application of this type of tanks are aerospace, aviation, and chemical engineering. In addition, fiber-reinforced tanks are widely used for increase in pressure during the transportation of oil and gas. In many cases of such use, tanks are exposed to high internal pressure, which may result in a step-like increase in stress on the vessel walls and their sudden collapse, causing great damage to material and human resources [3, 4].

In [5], a number of studies were carried out aimed only at exploring a pressure tank made of multilayer composite, during which the expected collapse resistance was determined. In [6], the behavior of a rotating composite pressure vessel under the internal pressure and axial load was studied. In [7], the effect of thermal loads on a multilayer composite pressure tank was described. In [8], the behavior of a polygonal composite pressure tank of five different shapes under the action of internal pressure of various modes was studied; and in [9], the performance of a composite pressure tank was explored under the influence of transverse loads.

The design of a composite tank is a challenge; therefore, priority factors should be selected to conduct a complete and accurate analysis. We studied a pressure vessel reinforced with several layers of carbon fibers and subjected to internal pressure loading. To determine the maximum stresses and displacements at operating pressure, to identify the expected limiting pressure causing destruction, as well as to identify the optimal angle of orientation of the fibers, a finite element model of the tank was created using ANSYS customized application.

Materials and Methods. Theoretical Research. The high-pressure tank made of carbon fibre reinforced plastic (CFRP) consists of a central part, which is a metal cylinder with an internal coating made from a polymer reinforced with carbon fibers. The end surfaces of the tank have the shape of hemispheres with spiral winding (Fig. 1).

Fig. 1. Longitudinal section of the tank

Tanks operating at high pressures and reinforced with carbon fiber are manufactured by the method of filament winding (Fig. 2). To obtain the required reinforcement stability, the fibers are sent to a moving trolley with careful selection of their coordination, and then wound onto a cylindrical surface. The stability of fiber coordination is influenced by several factors: temperature, surface shape and treatment, as well as the degree of adhesion of fibers to the matrix. The winding angle is controlled by the speed of the trolley and the rotation speed of the cylindrical drum. To obtain high operational and strength properties, the inner cylindrical surface of the tank is covered with several layers of fibers [10].

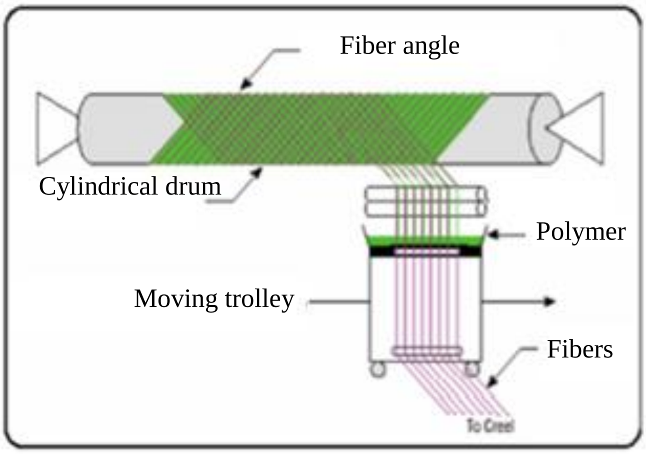

Fig. 2. Fiber winding scheme

The angle of the fibers has a significant effect on the properties of the vessels; therefore, to find the appropriate angle for each part of the vessel is of critical importance. The fiber orientation angle is determined by the required amount of friction between the fibers and the composite material layer, as shown in the relation:

$$\alpha(R) = \sin^{-1}\left(\frac{R_0}{R}\right) \pm \delta\left(\frac{R - R_0}{R_{t1} - R_0}\right)^n, \tag{1}$$

where R — distance between the center and the point of the layer; R_0 — central axis radius; R_{t1} — radius on the tangent to the surface of the cylinder at $\delta = 0$ [8].

Tsai-Wu Destruction Criteria. When studying and simulating a high-pressure tank made of composite material, the destruction criteria according to the Tsai-Wu theory [11] were used. The implementation of equation (1) is required to study the expected fracture of orthotropic materials according to the Tsai-Wu theory:

$$F_1\sigma_{11} + F_2\sigma_{22} + F_6\sigma_{12} + F_{11}\sigma_{22}^2 + F_{66}\tau_{12}^2 + 2F_{12}\sigma_{11}\sigma_{22} = 1.$$

Elastic properties are determined by four independent constants: E_{11}, E_{22}, G_{12}, V_{12}, presented in Table 1.

Table 1

Characteristics of LY5052/T300 composite material

Properties	Carbon fiber T300	Epoxide LY5052
Elasticity modulus	230 GPa	3.0 GPa
Tensile Strength	3.5 GPa	71.0 GPa
Density	1,760 g/cm^3	1.14 g/cm^3

Forces are calculated from the following equations:

$$F_1 = \frac{1}{X_t} - \frac{1}{X_c};\ F_2 = \frac{1}{Y_t} - \frac{1}{Y_c};\ F_6 = 0;\ F_{11} = -\frac{1}{X_t X_c};$$

$$F_{22} = -\frac{1}{Y_t Y_c};\ F_{66} = -\frac{1}{S_2};\ F_{12} = -\frac{1}{2}\sqrt{F_{11}F_{22}},$$

where X_t — tensile force in the longitudinal direction; Y_t — tensile force in the transverse direction; X_c — pressure force in the longitudinal direction; Y_c — pressure force in the transverse direction; S — shear force.

The maximum destructive stress is reached when one of the following ratios is met [12]:

$$\frac{\sigma_1}{X} \geq 1;\ \frac{\sigma_2}{Y} \geq 1;\ \frac{\tau_{12}}{S} \geq 1.$$

Material properties and finite element modeling. The composite material used for the tank under study is polymer reinforced with T300-type carbon fiber, and LY5052 epoxy is used as polymer material. Composite materials are orthotropic in nature; therefore, the process of modeling them with finite elements is more complicated than isotropic materials, such as aluminum and steel.

Figure 3 shows a finite element model of a high-pressure tank made of carbon fiber, whose inner layer consists of an aluminum alloy reinforced with eight layers of Carbon/Epoxy T300/LY5052 composite material.

The model has the following dimensions:

– tank length —1,200 mm;
– tank diameter in the center — 300 mm;
– total thickness — 64 mm;
– thickness of one layer — 6.5 mm;
– lining thickness — 0.12 mm.

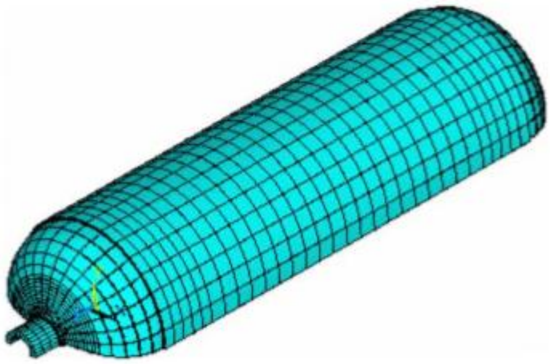

Fig. 3. Finite element model of the CFRP tank

To study high-pressure tanks made of composite materials, it is very important to select the appropriate type of finite elements. ANSYS program contains SHELL and SOLID finite elements required for modeling layered composite materials. For this study, SHELL 99 program was used, which accelerated the calculation of a structure with up to 250 layers. This element is a multi-level linear structure with eight nodes and six degrees of freedom. It allows the user to determine the flexibility, slope of layers, and density of each layer.

When studying composite materials, the formation of layers is one of the major issues, since each layer has its own angle of inclination, and the fibers in each layer have different angles of inclination; therefore, the properties of each layer should be determined separately.

The formation of layers requires the characteristics of the material, the number of layers, the fiber inclination angles, the thickness of the layer, and the number of integration points in each layer. Here is some comparative information about the properties of the materials used: CFRP and aluminum 6061. Density: CFRP — 1,570 kg/m^3, aluminum — 2,750 kg/m^3. Table 2 shows mechanical characteristics of the materials used: elastic modulus *E*; shear strength *G*; tensile strength *V*.

Table 2

Mechanical properties of CFRP and aluminum 6061

Parameters in the directions of coordinate axes, GPa	CFRP	Aluminum 6061
E_X	128	7070
E_Y	10.5	70
G_{XY}	5	70
G_{YZ}	5	
G_{ZX}	5	
V_{XY}	0.27	0.3
V_{YZ}	0.4	0.3
V_{ZX}	0.02	0.3

$$\left[+25^{o}/-25^{o}\right],\ \left[+30^{o}/-30^{o}\right],\ \left[+35^{o}/-35^{o}\right],\ \left[+40^{o}/-40^{o}\right],\ \left[+45^{o}/-45^{o}\right],\ \left[+50^{o}/-50^{o}\right],\ \left[+55^{o}/-55^{o}\right].$$

Figure 4 shows a sequence of layers with the fiber inclination at an angle of $\pm 45°$, implemented in ANSYS program.

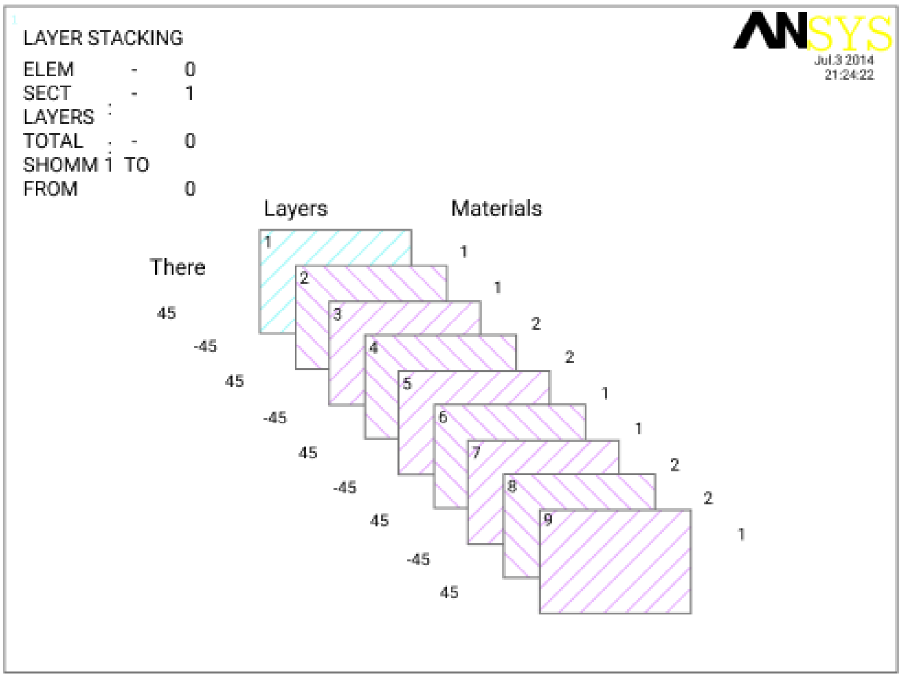

Fig. 4. Sequence of layers with the fiber inclination at an angle of $\pm 45°$

Digital simulation. Calculation of stresses and displacements. The operation of the high-pressure tank was analyzed using the destruction criteria according to Tsai-Wu theory. Internal working pressure of 35 MPa was used to calculate the maximum stresses and displacements. The greatest stress of the tank was observed at the angle of inclination of the annular fibers — 0° and various angles of inclination of the spiral fibers:

$$\left[+25^{\circ}/-25^{\circ}\right], \left[+30^{\circ}/-30^{\circ}\right], \left[+35^{\circ}/-35^{\circ}\right], \left[+40^{\circ}/-40^{\circ}\right], \left[+45^{\circ}/-45^{\circ}\right], \left[+50^{\circ}/-50^{\circ}\right], \left[+55^{\circ}/-55^{\circ}\right].$$

Figure 5 shows the distribution of equivalent stresses and displacements in the tank at the fiber inclination of $\pm 45°$. Tables 3, 4 show the maximum and minimum values of displacements and equivalent stresses in the directions of X, Y, Z coordinate axes.

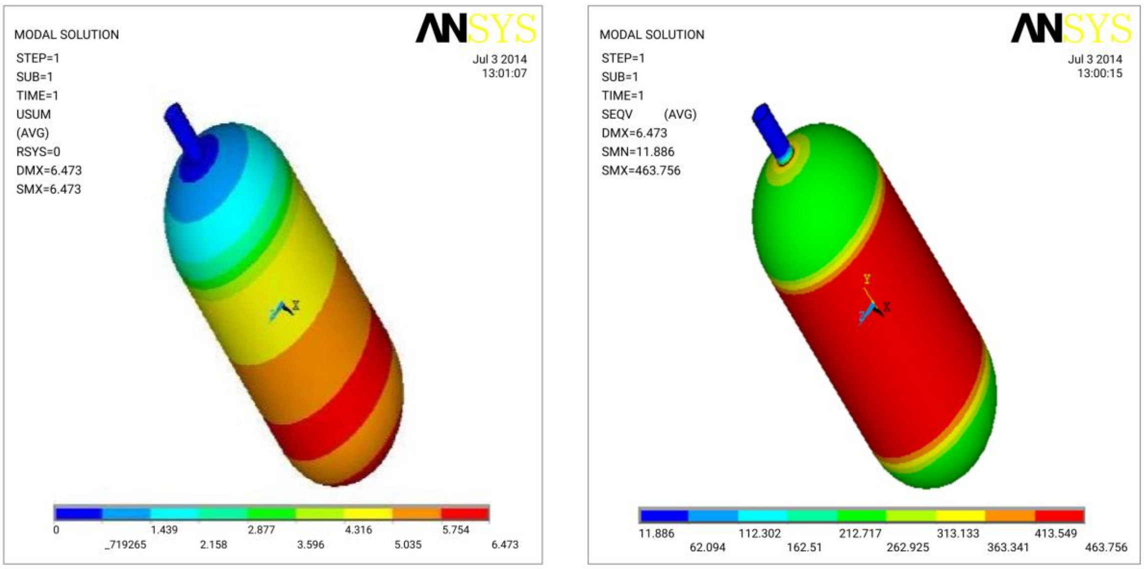

a) *b*)

Fig. 5. Equivalent distribution in the tank: *a* — stresses; *b* — displacements

Table 3

Maximum and minimum displacement values
in the directions of *X*, *Y*, *Z* axes

Direction of deformation	Minimum, mm	Maximum, mm
total vector	0	6.473
along *X*-axis	-3.914	3.914
along *Y*-axis	-6.473	0
along *Z*-axis	-3.906	3.909

Table 4

Maximum and minimum stress values in the direction of *X*, *Y*, *Z* axes

Direction of deformation	Minimum, MPa	Maximum, MPa
total vector	11.886	463.756
along *X*-axis	-81.852	528.485
along *Y*-axis	-155.587	341.607
along *Z*-axis	-80.307	530.07

Determination of the expected destructive pressure and the optimal fiber inclination angle. The loading of the tank was carried out through gradually increasing the internal pressure, starting from its operating value — 35 MPa. Then, the obtained design maximum internal pressure stress was compared to the final allowable stress under the condition: $\sigma_{\max} \le \sigma_u$, where: $\sigma_{\max}$ — design maximum stress; σ_u — final allowable stress. The permissible stress for CFRP pressure tanks is 1,210 MPa.

The cylindrical tank model was calculated for two types of fiber winding paths: annular and spiral, as well as at different fiber inclination angles:

$$\left[+25^{\circ}/-25^{\circ}\right], \left[+30^{\circ}/-30^{\circ}\right], \left[+35^{\circ}/-35^{\circ}\right], \left[+40^{\circ}/-40^{\circ}\right], \left[+45^{\circ}/-45^{\circ}\right], \left[+50^{\circ}/-50^{\circ}\right], \left[+55^{\circ}/-55^{\circ}\right].$$

With an annular winding path, the fiber inclination angle to the axis of the cylinder was 0 °. Figure 6 shows a finite element model of a cylindrical high-pressure tank.

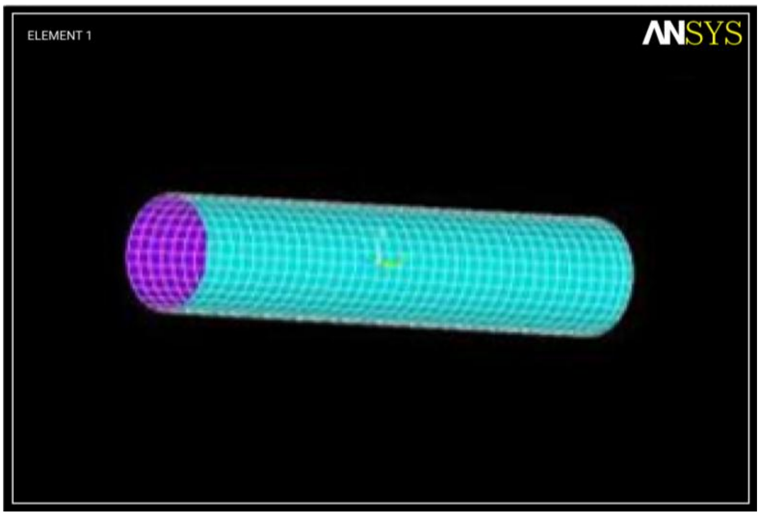

Fig. 6. Finite-element model of a cylindrical high-pressure tank

Research Results. Figure 7 shows the change in the maximum stress; starting from the angle value from 0° to 45°, it decreased, and then increased to the value of 65°. It was found that the maximum stress in a cylindrical CFRP pressure tank was the lowest at the fiber inclination angle of ± 45°.

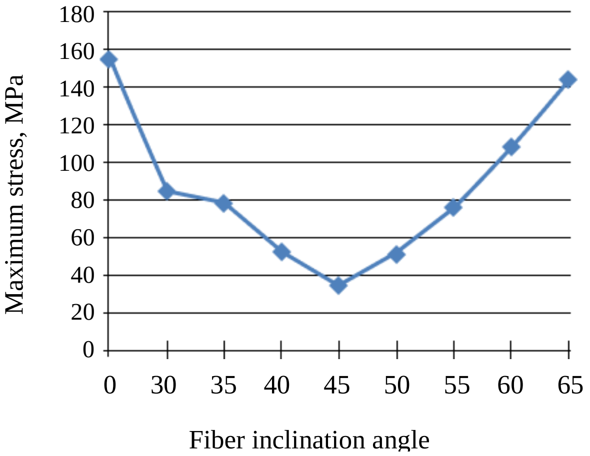

Fig. 7. Dependence of maximum stress on the fiber inclination angle

Figure 8 shows the results of the analysis of the pressure value for various fiber inclination angles: starting from the value of angle 0^{o} and up to 45^{o}, the pressure increased, and then it decreased to the value of angle 65^{o}. The maximum pressure that a CFRP tank can withstand without destruction is 207 MPa. This pressure occurs at the fiber inclination angle of $\pm 45^{o}$, i.e., it is the expected value of the destructive pressure for the tank.

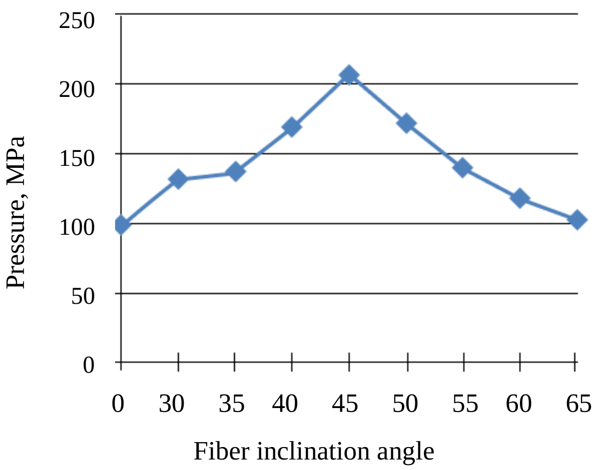

Fig. 8. Dependence of pressure on the fiber inclination angle

Figure 9 shows the distribution of stresses in the tank with fiber inclination angle of $\pm 45^{o}$, and the maximum pressure stress is 1,213 MPa, which is higher than the allowable stress for CFRP pressure tanks 1,210 MPa.

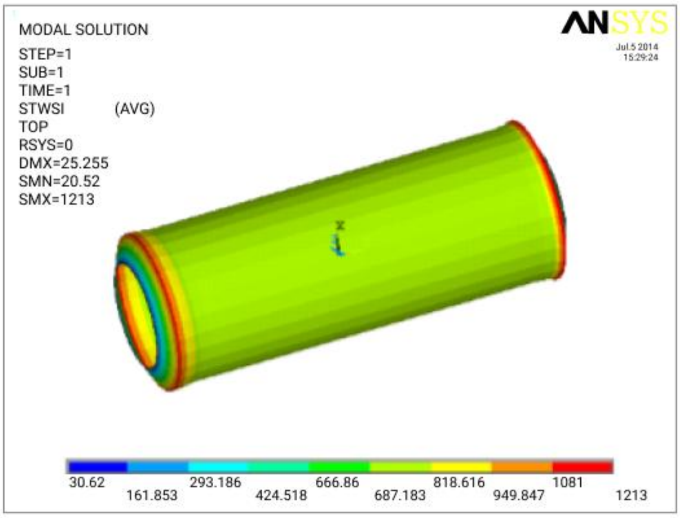

Fig. 9. Stress distribution in the tank under pressurization and at fiber angle of $\pm 45^{o}$

Machine building and machine science

Discussion and Conclusions. A finite element model of a carbon fiber reinforced tank was designed and analyzed using ANSYS program with the application of SHELL 99 element in the course of the simulation process. Several models were created with different fiber angles. The maximum stress and collapse pressure for the high-pressure vessel were calculated using the Tsai-Wu criteria. It was found that the maximum stress was the smallest at the fiber inclination angle of $\pm 45^{o}$, and the maximum possible collapse pressure under the same conditions was 207 MPa. This indicates that the optimal fiber angle for safe operation of a pressure vessel is $\pm 45^{o}$, and a CFRP vessel rated at the same fiber winding angle has maximum strength.

References

1. Sankar Reddy S, Yuvraj C, Prahlada Rao K. Design, Analysis, Fabrication and Testing of CFRP with CNF Composite Cylinder for Space Applications. International Journal of Composite Materials Structures. 2015;5:102−128. https://doi.org/10.5923.j.cmaterials.20150505.03.html

2. Subhash N Khetre, Nitnaware PT, Arun Meshram. Design and Analysis of Composite High Pressure Vessel with Different Layers using FEA. International Journal of Engineering Research & Technology (IJERT). 2014;3:1460−1464.

3. HS da Costa Mattos, LM Paim, JML Reis. Analysis of burst tests and long-term hydrostatic tests in produced water pipelines. Engineering Failure Analysis. 2012;22:128–140. https://doi.org/10.1016/j.engfailanal.2012.01.011

4. Goldin Priscilla CP, Selwin Rajadurai J, Krishnaveni A. Effect of statistical scatter in the elastic properties on the predictability of first ply failure of a polymer composite pressure vessel. Journal of Engineering Research. 2021. P. 128–140. https://doi.org/10.36909/jer.11529

5. Chang RR. Experimental and theoretical analyses of first-ply failure of laminated composite vessels. Composite Structures. 2000;49:237−243. https://doi.org/10.1016/S0263-8223(99)00133-6

6. Levend Parnas, Nuran Katuc. Design of fiber-reinforced composite vessels under loading condition. Composite Structures. 2002;58: 83−95. https://doi.org/10.1016/S0263-8223(02)00037-5

7. Aziz Onder, Onur Sayman, Tolga Dogan, et al. Burst failure load of composite pressure vessels. Composite Structures. 2009;89:159−166. https://doi.org/10.1016/j.compstruct.2008.06.021

8. Wahab MA, Alam MS, Pang SS. Stress analysis of non-conventional composite pipe. Composite Structures. 2007;79:125−132. https://doi.org/10.1016/j.compstruct.2005.11.054

9. Guedes RM. Stress-strain analysis of cylindrical pipe subjected to a transverse load and large deflection. Composite Structures. 2009;88:188−194. https://doi.org/10.1016/j.compstruct.2008.03.031

10. Madhavi M, Rao KVJ, Narayana Rao K. Design and Analysis of Filament Wound Composite Pressure Vessel with Integrated-end Domes. Defence Science Journal. 2009;59:73−81. http://dx.doi.org/10.14429/dsj.59.1488

11. Stephen W Tsai. Composites Design. 3rd ed. Dayton, Ohio: Think Composites; 1987.

12. Pihong Xu, Jinyang Zheng, PF Liu. Finite element analysis of burst pressure of composite hydrogen storage vessels. Materials & Design. 2009;30:2295−2301. https://doi.org/10.1016/j.matdes.2009.03.006

Received 04.04.2022

Revised 19.04.2022

Accepted 01.05.2022

About the Authors:

Antipas, Imad Rizakalla, associate professor of the Fundamentals of Machinery Design Department, Don State Technical University (1, Gagarin sq., Rostov-on-Don, 344003, RF), Cand,Sci. (Eng.), associate professor, ScopusID, ResearcherID, ORCID, imad.antypas@mail.ru

Dyachenko, Alexey G., associate professor of the Fundamentals of Machinery Design Department, Don State Technical University (1, Gagarin sq., Rostov-on-Don, 344003, RF), Cand,Sci. (Eng.), ScopusID, ORCID, alexey-a2@mail.ru

Claimed contributorship

I. R. Antipas: academic advising; research task setting; definition of research methodology; collection and analysis of the analytical and practical materials on the research topic; critical analysis and finalization of the solution; computer implementation of the problem solution. A. G. Dyachenko: analysis of scientific sources on the topic of research, critical analysis and revision of the text.

Conflict of interest statement

The authors do not have any conflict of interest.

All authors have read and approved.

MACHINE BUILDING AND MACHINE SCIENCE

UDC 621.914.1

https://doi.org/10.23947/2687-1653-2022-22-2-116-129

Original article

Analysis of Automated Surface Roughness Parameter Support Systems Based on Dynamic Monitoring

Mikhail R. Gimadeev ✉, **Andrey A. Li**

Pacific National University, 136, Tihookeanskaya St., Khabarovsk, Russian Federation

✉ 009063@pnu.edu.ru

Abstract

Introduction. Domestic and foreign works on the milling of complex-profile surfaces with a ball-end tool were analyzed. Methods of surface quality control and ways to provide amplitude parameters of roughness, based on research data and field experiments, were considered. Theoretical provisions on the determination of cutting forces and the results of vibroacoustic diagnostics were presented.

Materials and Methods. The methods of correlation analysis, comparison and generalization of the results were applied. The data were calculated at different tool angles, taking into account the instantaneous cutting forces, and were fixed in the range of values of the variable feed per tooth (fz) and the angle of inclination of the surface (γ). The vibroacoustic diagnostic data and theoretical data of the presented model at different tool inclination angles were verified by experiment. Consequently, such methods can be used to predict surface roughness parameters.

Results. The relationship between cutting forces, tool inclination angle, and vibroacoustic diagnostics data was found. A model of the cutting force and tool displacements was formulated taking into account the inclination of the surface. The optimal range of the inclination angle of the tool to the surface to be machined, at which the minimum values of the amplitude parameters of roughness were achieved, was determined. The sound vibrations obtained empirically, presented in spectral and wave forms, were in good agreement with data from other sources. This allowed us to conclude about the feasibility of forecasting and monitoring roughness parameters in real time through acoustics.

Discussion and Conclusions. It was established that the growth of forces in the direction $a_e(X)$ and $fz(Y)$ was observed at $\gamma > 40°$. This was due to the distribution of the components of the cutting force along the cutting edge and depended on the inclination of the surface. The amplitude parameters decreased when the angle increased from 10 to 40 degrees. The found interrelations of force analysis, processing directions, and vibroacoustic diagnostics have validated the use of vibroacoustic diagnostics to predict surface roughness. Acoustic diagnostics, regardless of the layout of technological equipment, enables to quickly adjust the sound device and assess the impact of cutting modes on roughness parameters.

Keywords: surface roughness, ball-end tool, vibroacoustic diagnostics, milling, tool inclination, vibration, cutting forces.

Acknowledgements: the authors would like to thank A.V. Nikitenko, Cand.Sci. (Eng.), associate professor of the Department of Technical Informatics and Information Systems (PNU, Khabarovsk), for assistance with organizing and conducting experimental research at the CAD/CAM Technologies Training and Production Center.

For citation: M. R. Gimadeev, A. A. Li. Analysis of automated surface roughness parameter support systems based on dynamic monitoring. Advanced Engineering Research, 2022, vol. 22, no. 2, pp. 116–129. https://doi.org/10.23947/2687-1653-2022-22-2-116-129

Introduction. Specialists do not have enough software tools that could help predicting the value of the cutting force, vibration amplitude, etc., when programming machines with numerical control (CNC). As a result, it is required to select the feed rate based on experience, setting a constant feed rate for the entire processed complex surface. This can reduce the processing efficiency and surface quality. To solve this problem, it is required to build a highly accurate and reliable model for predicting surface roughness.

Currently, two main approaches are used in such forecasting. In the first case, photoelectric sensors transmit roughness data online. This method efficiency is quite low because chips are formed during the cutting process, and a lubricating fluid (lubricoolant) is supplied to the area of the recorded microrelief. The second group includes control methods using artificial intelligence, as well as theoretical modeling and modeling of empirical regression analysis. In practice, methods from the second group are most common.

The authors of paper [1] explored the spherical tool milling of aerospace components made of aluminum alloy LM6 and developed a model using ARMAX structures (autoregressive moving average with exogenous inputs) to predict surface roughness under various processing modes. In [2], a mathematical model of the trajectory of a spherocylindrical tool for processing mushroom-shaped blades of a steam turbine was presented to improve the processing efficiency and surface quality. The authors [3] created an analytical model of the milling with a spherocylindrical tool and considered the situation of vibration occurrence to predict the limits of tool stability at different angles of inclination and spindle rotation speed.

In [4], the processing of the impeller on a five-axis CNC machine using a spherical cylindrical tool was studied. The tool trajectory and optimal cutting modes had to be developed due to the complex curved surface and the close location of the wheel blades, since in this case, it was impossible to use standard CAM systems (computer-aided manufacturing - an automated system or its module for the preparation of control production programs).

In [5], a system for optimizing the feed rate for three-axis milling with a spherical tool was described. The authors used the geometric modeling capabilities of B-rep ACIS: miter cutting was converted to an orthogonal model for various tools and workpieces. The authors [6] created a mathematical model of a constant cutting force [7] for processing a complex curved surface with a spherocylindrical tool on a CNC machine through maintaining a constant cutting speed at different tool inclination angles. Paper [8] presents a dynamic model of the milling with a spherical cylindrical tool, including cutting modes and tool edge wear. The authors [9] developed a real-time monitoring system with error compensation to improve accuracy in the production of free-form parts. In [10], the energy consumption of various cutting strategies was studied to evaluate the efficiency of each cutting strategy. The authors of this work have established that the optimal strategy enables to provide the specified parameters of surface quality. Many scientists used the Taguchi method to optimize processing parameters [11–13]. Some of the surveys are narrowly focused, and more work is needed to scale up the results [14–18].

The analysis of literature sources found the absence of recommendations on using the method of forecasting and monitoring roughness in real time. This is even more so in cases where sound vibrations in the air are taken into account.

Materials and Methods. To determine the cutting forces, a model from [7, 19] is used:

$$\begin{aligned} dF_{tj} &= K_{te}dl_j + K_{tc}dS_{zj}, \\ dF_{rj} &= K_{re}dl_j + K_{rc}dS_{zj}, \\ dF_{aj} &= K_{ae}dl_j + K_{ac}dS_{zj}. \end{aligned} \tag{1}$$

Here, K_{te}, K_{re}, K_{ae} — edge specific coefficients; K_{tc}, K_{rc}, K_{ac} — shear specific coefficients; dl_j — incremental cutting-edge length l_j [20]; S_{zj} — cross-sectional area of the cut segment.

In this model, a set of curvilinear coordinate systems, perpendicular to the tangents to the spherical surface, is used to set the resulting force acting on the *i*-th infinitesimal segment of the cutting edge.

The geometry of the spherocylindrical end mill is schematically shown in Figure 1.

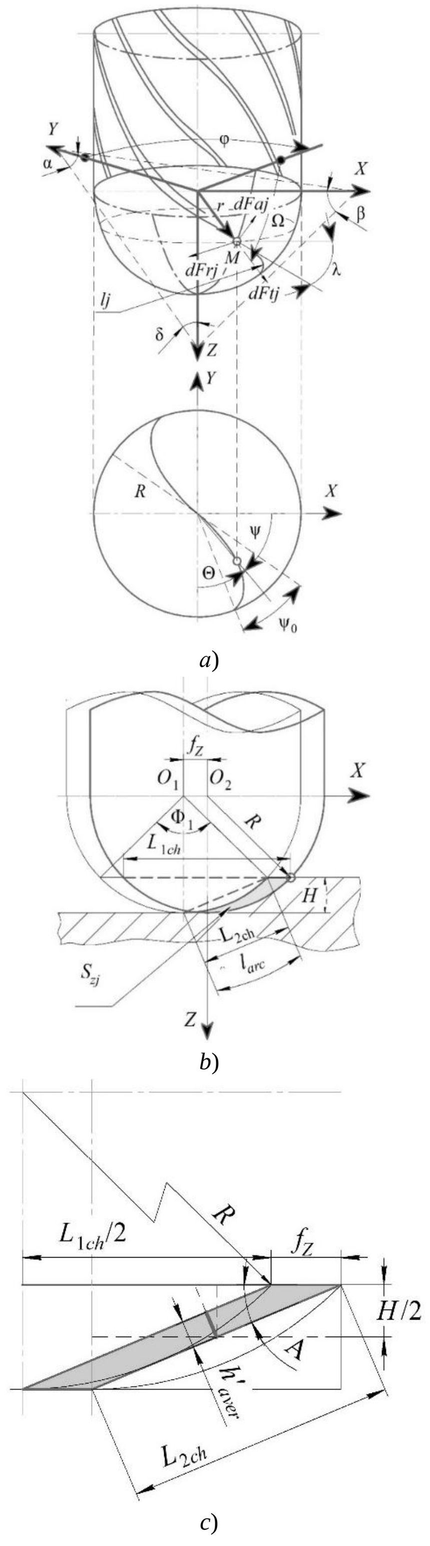

Fig. 1. Diagram for determining: *a* — cutting forces of a spherocylindrical cutter;
b — segment to be cut; *c* — cross-sectional area of the given figure [16]

The diagram shows the angle of inclination λ of a milling cutter with a spherocylindrical initial surface of the tool along the cutting edge. Here, we also see:

− tangential dF_{tj}, radial dF_{rj}, axial dF_{aj} cutting forces acting on the *j*-th tooth, and the coordinates of the tool for the spherocylindrical end mill (Fig. 1 *a*);

− chord L_{2ch}, segment angle Φ_1, arc length l_{arc} (Fig. 1 *b*);

− cross-section area (Fig. 1 *b*, *c*).

$$S_{zj} = L_{2ch} \cdot h'_{aver}, \tag{2}$$

where L_{2ch} — length of the second chord, mm; h'_{aver} — average chip thickness, mm.

$$L_{2ch} = 2 \cdot \sqrt{\left(\frac{H}{2}\right)^2 + \left(\frac{L_{1ch}}{4}\right)^2}, \tag{3}$$

$$h'_{aver} = fz \cdot \sin A. \tag{4}$$

Length of the first chord L_{1ch}, arc length l_{arc}, and circle segment angle Φ_1:

$$L_{1ch} = 2 \cdot \sin \cdot \frac{l_{arc}}{2R} \cdot R, \tag{5}$$

$$l_{arc} = \frac{\Phi_1 \cdot R}{2}, \tag{6}$$

$$\Phi_1 = 2\arccos\left(1 - 2 \cdot \frac{H}{2R}\right). \tag{7}$$

Angle A (Fig. 1 *c*) for calculating the average chip thickness:

$$A = \arctan\left(\frac{H}{L_{1ch} / 2}\right). \tag{8}$$

Radius vector r of the current point of the initial tool surface:

$$r = \begin{bmatrix} R\sin\varphi \cos\Omega \\ R\sin\varphi \sin\Omega \\ R\cos\varphi \\ 1 \end{bmatrix}. \tag{9}$$

The equation of the cutting edge is solved as the equation of a curve located on the original instrumental surface and crossing the meridians at angle λ 90°. A parametric equation of the form $\Omega = \Omega(\varphi)$ describes a certain line on the sphere. Cosines of the angles between the axes of *XYZ* coordinate system of the spherocylindrical cutter and the tangent line to the curve $\Omega = \Omega(\varphi)$ on the initial tool surface:

$$\begin{aligned} \cos\alpha &= \frac{dX}{dS} = \frac{\cos\varphi \cos\Omega \, d\varphi - \sin\varphi \sin\Omega \, d\varphi}{\sqrt{d\varphi^2 + \sin^2\varphi \, d\Omega^2}}, \\ \cos\beta &= \frac{dY}{dS} = \frac{\cos\varphi \sin\Omega \, d\varphi - \sin\varphi \cos\Omega \, d\varphi}{\sqrt{d\varphi^2 + \sin^2\varphi \, d\Omega^2}}, \\ \cos\delta &= \frac{dZ}{dS} = \frac{-\sin\varphi \, d\varphi}{\sqrt{d\varphi^2 + \sin^2\varphi \, d\Omega^2}}, \end{aligned} \tag{10}$$

where dS — cutting edge arc differential.

Cosines of the angles between the coordinate axes and the tangent to the meridian (at Ω = const) on the initial tool surface are represented as Radzevich's dependences [21]:

$$\begin{aligned} \cos\alpha &= \frac{dX}{dS} = \cos\varphi \cos\Omega, \\ \cos\beta &= \frac{dY}{dS} = \cos\varphi \sin\Omega, \\ \cos\delta &= \frac{dZ}{dS} = -\sin\varphi. \end{aligned} \tag{11}$$

We set the condition: $\Omega = \lambda$. Then, the cutting-edge equations in parametric form:

$$\begin{aligned} X &= \frac{R\cos\lambda}{chq(\lambda + C)}, \\ Y &= \frac{R\sin\lambda}{chq(\lambda + C)}, \\ Z &= Rthq(\lambda + C), \end{aligned} \tag{12}$$

where ch — hyperbolic cosine, th — hyperbolic tangent.

To determine the infinitesimal length of the cutting edge, we can use the expression proposed in [7, 16, 19]:

$$dl = \sqrt{r^2(\psi) + \left(r'(\psi)^2\right) + \left(z'(\psi)^2\right)}\, d\psi, \tag{13}$$

where

$$\left.\begin{aligned} r(\psi) &= \sqrt{1 - (\psi \cot\lambda - 1)^2} \\ r'(\psi) &= \frac{-R(\psi \cot\lambda - 1)\cot\lambda}{\sqrt{1 - (\psi \cot\lambda - 1)^2}} \\ z'(\psi) &= X^2 + Y^2 + (R - Z)^2 \cot^2\lambda \end{aligned}\right\}. \tag{14}$$

Main Text

Experiment Details. At the preparatory stage, the literature was studied [22–27]. The data for planning the experiment are described below. Machining was carried out in passing and counter directions (Fig. 2), on blanks with the properties of steel 45 (foreign analogues — C45, 1045). We used a spherocylindrical end carbide milling cutter with a diameter of D = 8 mm, with two teeth from Sandvik Coromant (z = 2). The ratio of the overhang of the tool installed in the chuck was taken as l / D, equal to 4. The milling tool made of fine-grained tungsten carbide had anti-wear coating TiAlN and parameter λ = 30°. Feed per tooth fz = 0.2 mm/tooth, allowance for all samples $a_p = H$ = 0.2 mm, lateral pitch a_e = 0.2 mm.

To provide equal cutting speed V_c at different angles of inclination (γ) of the tool to the surface to be processed, the rotation frequency (n) varied in the range from 1478 min^{-1} to 8000 min^{-1}.

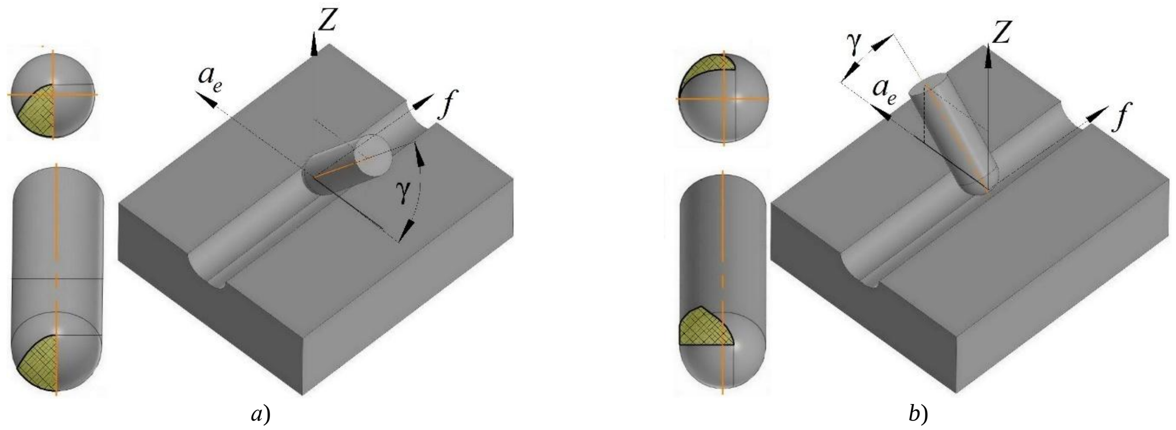

Fig. 2. Types of the conditional contact surface of workpiece and tool at different values of tool inclination angles in the direction: *a* — passing; *b* — counter

Angle γ was selected from the range from 10° to 50°; therefore, the calculation of the effective diameter D_{cap} (L_{1ch}) was carried out using the formulas:

$$\gamma > 0° \begin{cases} D_{cap} = 2D\cos\omega = 2 \cdot R \cdot \cos(90° - \gamma) \\ \text{or} \\ D_{cap} = L_{1ch} = 2 \cdot \sin \cdot \dfrac{l_{arc}}{2R} \cdot R. \end{cases} \tag{15}$$

In the experiments, a DMG DMU 50 CNC machine (Heidenhain control system) was used. The surface roughness after treatment was measured using profilometer-profilograph-contorograph Surfcam 1800D. In accordance with the current standards[1], measurements were carried out along various routes. To find the maximum values of the surface roughness parameters, 50 % Gaussian filtration was used. Vibroacoustic diagnostics was performed according to GOST R ISO 7919-3-99[2] using spectrum analyzer Zet 017-U2. As an output evaluation of the processing efficiency, amplitude A of the vibrations of the spindle assembly (mm), varying with time (t, s) was used.

[1] GOST 27964-88. Measurement of surface roughness parameters. Terms and definitions. Moscow, 2018. 13 p. (In Russ.)
[2] GOST R ISO 7919-3-99. Mechanical vibration of non-reciprocating machines. Measurements on rotating shafts and evaluation criteria. Moscow, 2000. 12 p. (In Russ.)

Research Results. The experiment has shown that the real surface roughness differs significantly from the data of theoretical models — the results of the kinematic-geometric projection of the tool on the workpiece. Currently, there is a growing demand for details of a spatially complex configuration and surface quality requirements. In this regard, it is worth focusing on the requirements of predictability of machining results, expressed, among other things, by roughness indicators.

Tables 1 and 2 present the results of the experiment of amplitude parameters of roughness described in GOST R ISO 4288[3].

Table 1

Roughness parameters depending on the machining direction
with a spherocylindrical tool under climb milling

	Amplitude parameters of roughness, μm					
Angle, °	*Ra*	*Rq*	*Rz*	*Rt*	*Rp*	*Rv*
10	0.457	0.569	2.912	5.000	1.671	1.240
20	0.597	0.735	3.936	5.159	2.335	1.600
30	0.449	0.561	3.007	4.960	1.808	1.200
40	0.479	0.590	3.232	4.239	1.823	1.407
50	0.787	1.027	6.615	12.68	4.119	2.496

Table 2

Roughness parameters depending on the machining direction
with a spherocylindrical tool under up-cut milling

	Amplitude parameters of roughness, μm					
Angle, °	*Ra*	*Rq*	*Rz*	*Rt*	*Rp*	*Rv*
10	0.806	1.006	4.776	5.960	2.776	2.000
20	0.752	0.935	5.207	6.440	2.847	2.359
30	0.509	0.647	3.727	5.239	2.223	1.503
40	0.628	0.805	4.832	7.400	2.912	1.919
50	0.730	0.915	5.111	7.639	3.039	2.072

Analyzing the data of Tables 1 and 2, we note that the prevailing influence on the "height" of the roughness is exerted by the cutting direction. The quantitative value of the amplitude parameters is "lower" under climb milling. Hereafter, we will talk only about this type of milling. Based on the data in Table 1, a correlation analysis was performed, and a correlogram was made up (Fig. 3). The found dependences were correlated with the results of papers [28, 29].

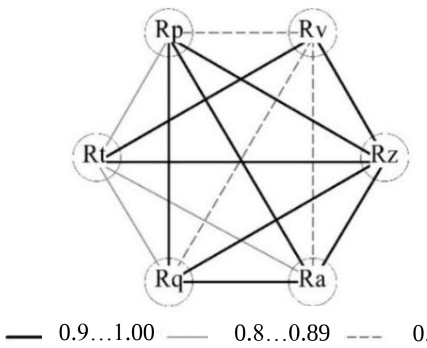

Fig. 3. Correlogram of the amplitude roughness parameters after milling under climb milling

The equations obtained during the correlation analysis helped us to move away from the direct normalization of roughness parameters. At the same time, analytical dependences provided minimizing the number of controlled factors. This reduced the complexity of the transition to real-time monitoring of sound vibrations.

[3]GOST R ISO 4287-2014. Geometrical Product Specifications (GPS). Surface texture. Profile method. Terms, definitions and surface texture parameters. Moscow, 2015. 20 p. (In Russ.)

In the presented study, the cutting forces (Fx, Fy, Fz) were calculated (Fig. 4). It can be seen that the inclination angle of the surface γ affected significantly the cutting forces.

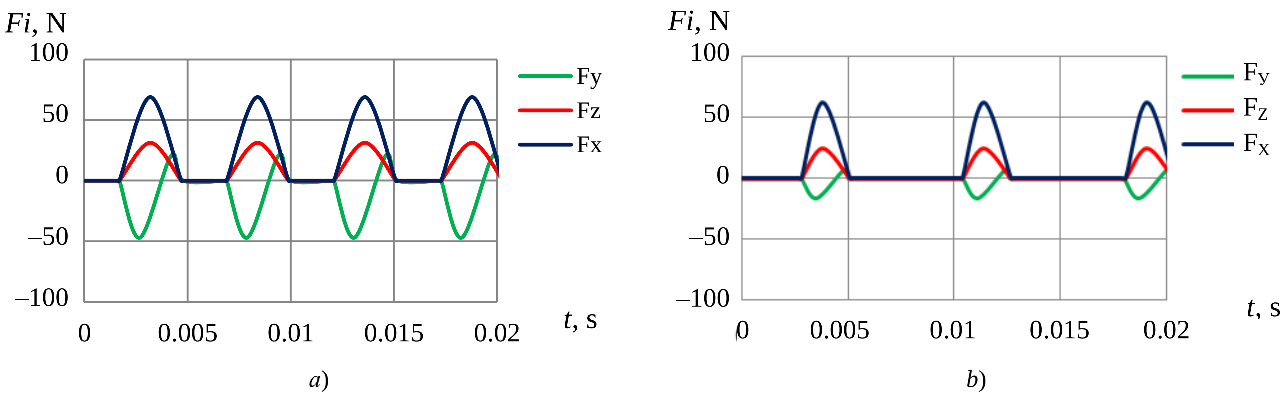

Fig. 4. Cutting forces calculated for: *a* — γ = 10; *b* — γ = 40

The data obtained allowed us to establish that the forces decreased with an increase in the tool inclination angle from 10° to 40°. In addition, force Fx was most sensitive when the inclination angle of the surface changed. It should also be noted that the cutting forces calculated according to the above-mentioned method were in good agreement with the empirical results obtained [6, 17, 24, 26, 27, 30].

With an increase in angle γ, the maximum area of plunging of the tool into the workpiece decreased (determined by the working angle and the active number of teeth z_c). Consequently, when finishing milling with a spherocylindrical tool, "pulsating" forces may be present, since for the inclination angle of the surface γ > 0°, the number of active teeth is often less than one ($z_c < 1$).

To establish z_c, sound vibrations during cutting were analyzed. The authors of [31] proposed to divide the spectrum of vibrations of working bodies into ranges:

− 20…300 Hz — low frequency,

− 300…1500 Hz — medium frequency,

− 1500 Hz and more — high frequency.

The experimentally obtained range of sound vibrations is shown in Figure 5.

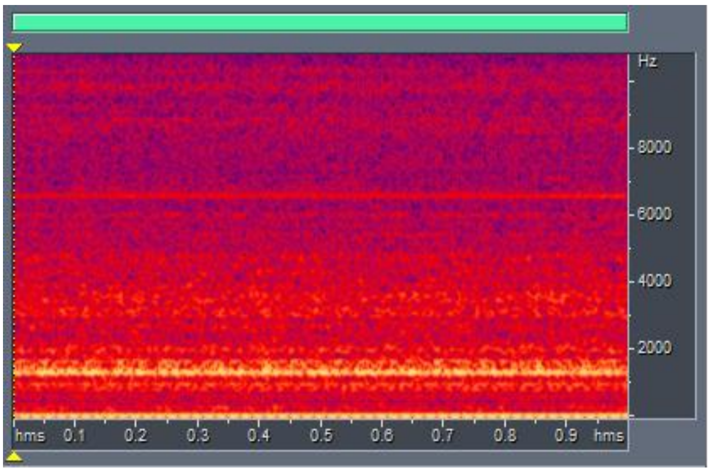

Fig. 5. Experimentally obtained spectral type of sound wave (segment is 1 sec)

The vibrations of the mounting elements and feed drives should be attributed to the low frequency range, the frequency of tool, spindle, etc. — to the medium and high frequency ranges. In this work, from the point of view of acoustic diagnostics, optimal cutting modes were determined that supported the stable operation of the technological system.

The frequency corresponding to the cutting frequency was pre-determined (Fig. 6). Filtering was applied to sound vibrations under:

− spindle assembly movement (Y, Z),

− rotation (n),

− table movement (X),

− noise in the laboratory.

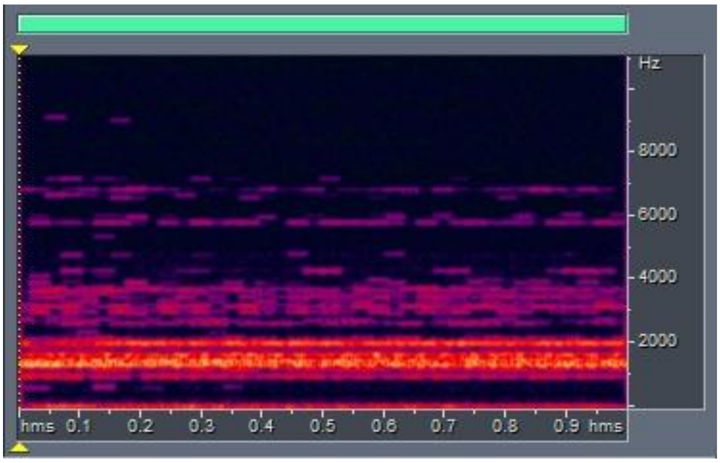

Fig. 6. Spectrogram of the sound wave after filtering (segment is equal to 1 sec)

Some spread in values (Fig. 6), associated with a huge number of factors that were difficult to exclude when conducting a full-scale experiment, is noteworthy.

The middle of the pronounced frequency range shown in Figure 5 corresponded to a rotation of 1500 rpm with a tool tilt of 40°. Acoustic diagnostics confirmed that the cutting went on almost continuously, i.e., without shock “pulsating” loads. The latter situation is shown in Figure 7. Here, the allocated evaluation time is 0.5 s, the number of periods is 25.

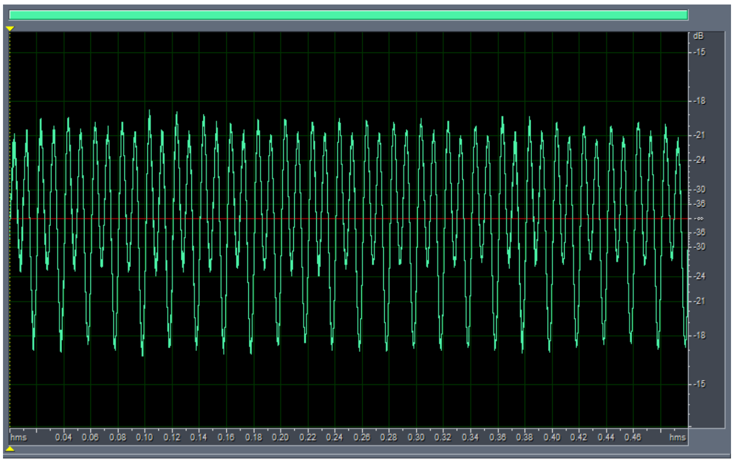

Fig. 7. Filtered fragment of the sound wave based on the sound of cutting at $\gamma = 40°$ (segment is 1/2 sec)

Figure 7 shows an ambiguously interpreted sound wave. However, it is quite easy to characterize it if we delve into the essence of mechanical milling. Under the climb milling and rounding of the cutting edge, plastic deformations of the metal with residual stresses remain on the treated surface. Even with proper coolant supply, temperature deformations occur in the surface layers of the material and distort the crystal lattice (residual stresses of the III kind). Along with this, after removing the tool, the stretched upper layers of the metal acquire residual compression stresses. If we describe the machining from the kinematics of the process, of note, the chip removal factor, namely value Θ_2 — the cutting angle of the material with the inclined spindle in the passing direction (Fig. 8).

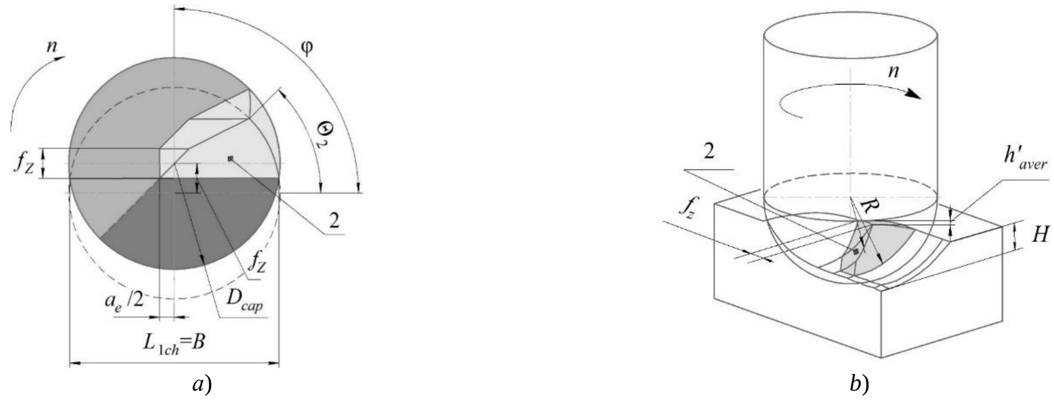

Fig. 8. Segment 2 to be cut off during machining: *a* — top view; *b* — projection of the segment being cut [16]

We specify that the tool cut in zone 2. The data obtained were validated by the simulation results, but were considered for the ideal case.

Along with these factors, theoretical and empirical discrepancies were often caused by vibrations associated with tool deflection and wear, as well as with the geometry of the cutting zone. Figure 7 shows the process of cutting the workpiece material with the *j*-tooth of the tool, which, along with other factors, determines such an interesting shape of the resulting wave.

In addition to the above, Figure 9 presents dependences which show that with a decrease in the amplitude of vibrations, the angle of inclination increased from 10° to 40°.

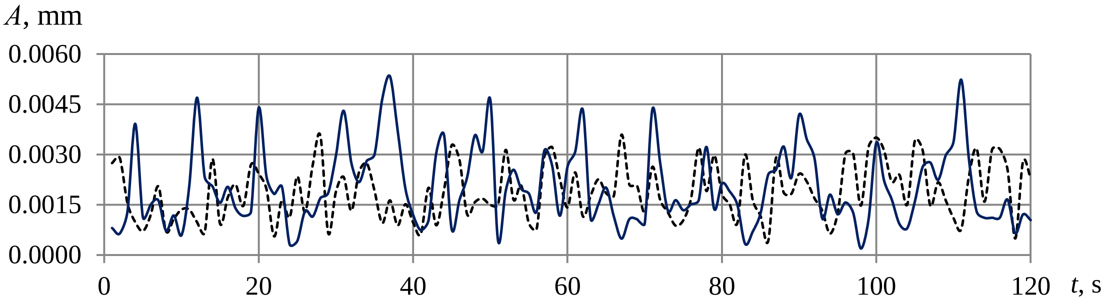

Fig. 9. Vibration amplitudes depending on the surface inclination angle: solid line — 10°, dotted line — 40°

M. R. Gimadeev and V. V. Gusliakov[4] analyzed the international practice of profile assessment of surface roughness. The authors of work [32] put forward proposals for the transition to a three-dimensional assessment. In the presented study, roughness measurements were carried out in an orthogonal coordinate system to make a comprehensive assessment.

The analysis of the profilograms obtained (Fig. 10) allowed us to conclude about the regularity of the surface microrelief after processing with a spherocylindrical end mill. In this case, it is impractical to take into account the roughness of the tool, since its manifestations are insignificant. Some additional increase in roughness was observed in the direction of the side pitch a_e, which verified the increase in elastic squeezes of the tool. The presented profiles, where the profile periods (peak-to-valley) correspond to a given feed value fz = 0.2 mm/tooth, testify to this.

[4] Gimadeev MR. Analiz zarubezhnogo opyta pri frezerovanii sferotsilindricheskim instrumentom. Khabarovsk: Informatsionnye tekhnologii XXI veka; 2019. P. 330–334. (In Russ.)

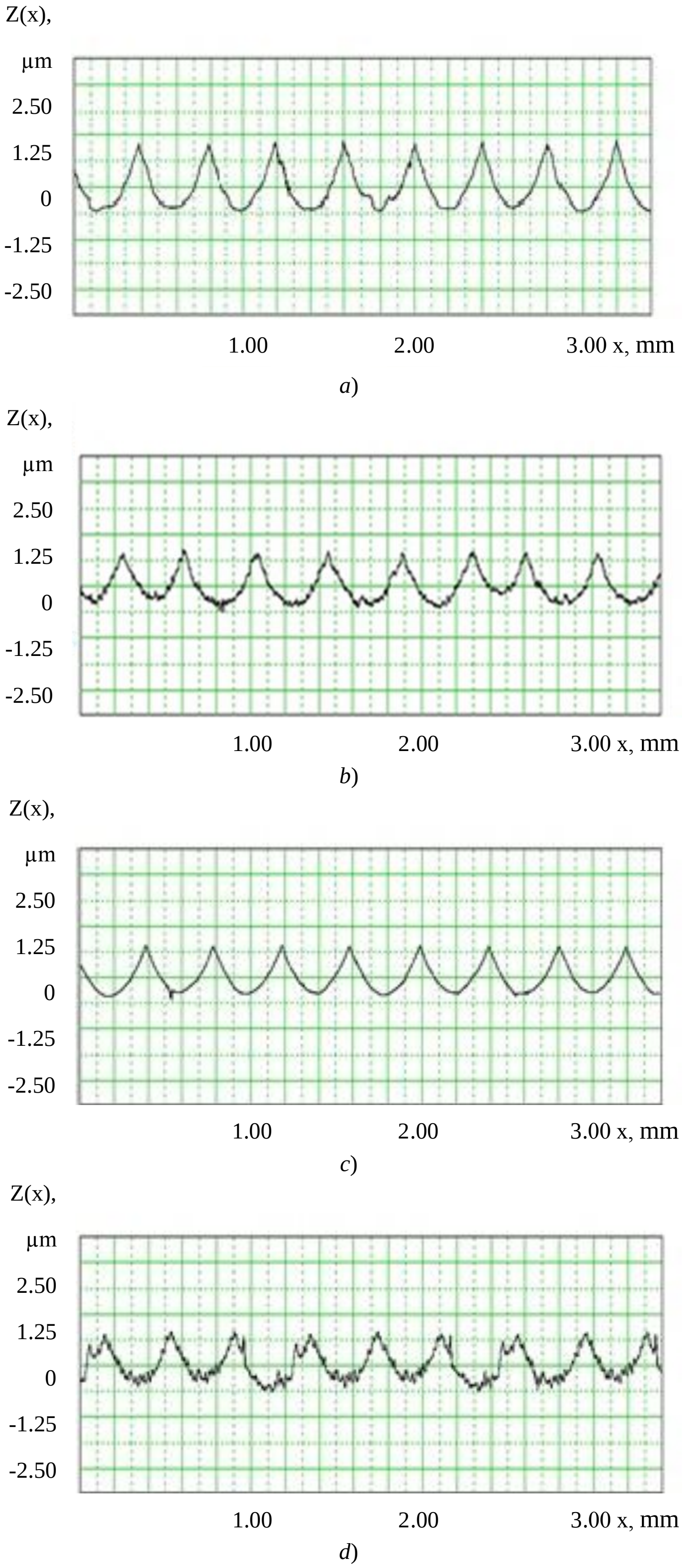

Fig. 10. Profilograms of surfaces after milling at different inclination angles γ:
a — γ = 10; direction f_z; *b* — γ = 10; direction a_e; *c* — γ = 40; direction f_z; *d* — γ = 40; direction a_e

Photomicrographic images of the treated surface have an obvious hexagonal shape (Fig. 11). The quality of the machined surface in the direction of the side pitch a_e may decrease due to the cutting tool retraction and an increase in the amplitude of the technological system vibrations under milling. This is validated by the results of vibroacoustic diagnostics.

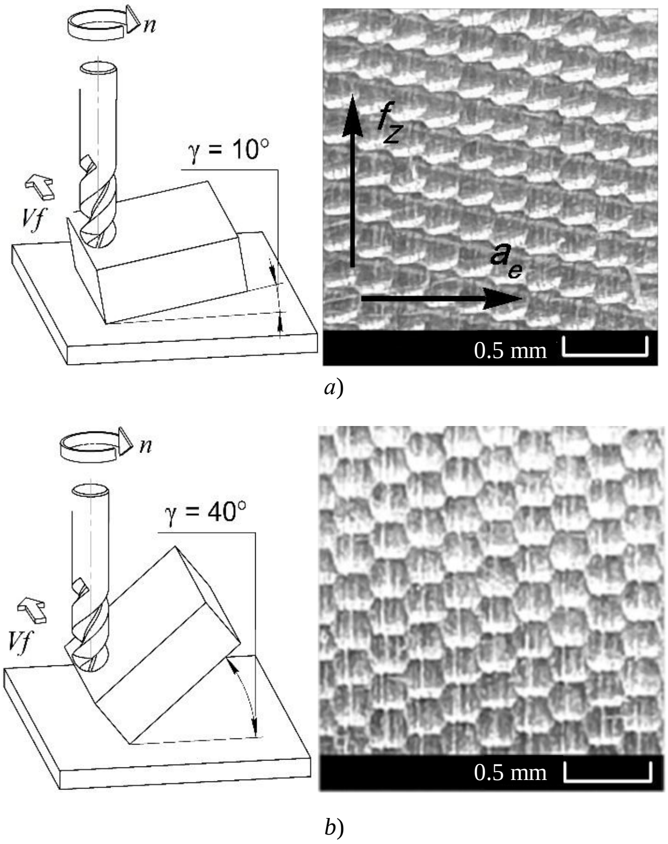

Fig. 11. Milling scheme and photo of the treated surface at: *a* — γ = 10; *b* — γ = 40

We emphasize once again that the experimental results correlate with the data obtained by many authors, and are consistent with the theories of elasticity, shaping, material cutting, and mechanical engineering technology.

Discussion and Conclusions. The influence of the inclination angle of the treated surface on the cutting forces, vibrations and microrelief parameters was studied. A model of cutting force and vibration was created, including kinematic and geometric parameters. The study has shown that quantitatively and qualitatively the cutting forces and vibrations of the cutting tool depend on the angle of inclination of the surface.

An analysis of the experimental data made it possible to identify a trend towards a decrease in the amplitude parameters of roughness by 10–20 % with an increase in the angle of inclination to 30–40°. The quality of the treated surface was reduced due to the elastic retraction of the spherocylindrical tool and an increase in the amplitude of vibrations of the technological system.

It was established that the forces grew in direction $a_e(X)$ and $fz(Y)$ at $\gamma > 40°$. This can be explained by the distribution of the cutting force components along the cutting edge, which depends on the inclination of the surface.

The solutions to the problems of monitoring and analysis of roughness parameters obtained by the authors due to acoustic diagnostics can significantly reduce the volume of experimental studies. This approach makes it possible to significantly reduce the cost of material resources and time for mechanical processing of products.

The experimental results are of practical interest and make the information about the formation of microrelief, including the roughness parameters under mechanical cutting, more accurate. A more detailed study of the proposed method of acoustic diagnostics is needed.

References

1. Vijiakumar S Jatti, Ravi Sekhar, Pritesh Shah. Machine learning based predictive modeling of ball nose end milling using exogeneous autoregressive moving average approach. In: Proc. 2021 12th IEEE Int. Conf. on Mechanical and Intelligent Manufacturing Technologies (ICMIMT). 2021. P. 68–72. https://doi.org/10.1109/ICMIMT52186.2021.9476067

2. Zhou Lingli, Liu Guoqing, Xiong Xiaocong. Research and development of fungus shaped blade root CAM software based on VB. In: Proc. 2021 4th IEEE Int. Conf. on Pattern Recognition and Artificial Intelligence (PRAI). 2021. P. 291–295. https://doi.org/10.1109/PRAI53619.2021.9551076

3. Koichi Akazawa, Eiji Shamoto. Study on regenerative chatter vibration in ball end milling of flexible workpieces. In: Proc. 2008 IEEE Int. Symposium on Micro-Nano Mechatronics and Human Science. 2008. P. 1–6. https://doi.org/10.1109/MHS.2008.4752412

4. Xiurong Zhu, Yeu Wang. Process analysis and parameter optimization of five axis NC machine for machining complex curved surface impellers. In: Proc. 2019 IEEE Int. Conf. on Intelligent Transportation, Big Data & Smart City (ICITBS). 2019. P. 122–124. https://doi.org/10.1109/ICITBS.2019.00036

5. Salami R, Sadeghi MH, Motakef B. Feed rate optimization for 3-axis ball-end milling of sculptured surfaces. International Journal of Machine Tools & Manufacture. 2007;47:760–767. https://doi.org/10.1016/j.ijmachtools.2006.09.011

6. Lei Shi, En Fu Liu, Yi Zhang, et al. The simulation of cutting force of free-form surface machining with ball-end milling cutter. In: Proc. 2009 IEEE Int. Conf. on Industrial Engineering and Engineering Management. 2009. P. 2314–2318. https://doi.org/10.1109/IEEM.2009.5373028

7. Altintas Y, Lee P. Mechanics and dynamics of ball end milling. Journal of Manufacturing Science and Engineering. 1998;120:684–692. https://doi.org/10.1115/1.2830207

8. Anstev AV, Ngon Dang Thien, Trong Dang Huu, et al. Influence of vibration amplitude on tool wear during ball end milling of hardened steel. In: Proc. 2018 4th IEEE Int. Conf. on Green Technology and Sustainable Development (GTSD). 2018. P. 232–236. https://doi.org/10.1109/GTSD.2018.8595567

9. Yueping Chen, Jian Gao, Haixiang Deng, et al. Spatial statistical analysis and compensation of machining errors for complex surfaces. Precision Engineering. 2013;37:203–212. https://doi.org/10.1016/j.precisioneng.2012.08.003

10. Vila C, Abellán-Nebot JV, Siller-Carrillo HR. Study of different cutting strategies for sustainable machining of hardened steels. Procedia Engineering. 2015;132:1120–1127. https://doi.org/10.1016/j.proeng.2015.12.604

11. Avinash A Thakre. Optimization of milling parameters for minimizing surface roughness using Taguchi's Approach. International Journal of Emerging Technology and Advanced Engineering. 2013;3:226–230.

12. Amal TS, Vidya V, Abraham AK. Machining parameters optimization in end milling of Ti6Al4V using Taguchi method. International Journal of Research in Engineering and Technology. 2015;3:31–40.

13. R Ashok Raj, Parun T, Sivaraj K, et al. Optimization of milling parameters of EN8 using Taguchi methodology. International Journal of Mechanical Engineering and Robotics Research. 2013;2:202–208.

14. Boujelbene M, Abellard P, Bayraktar E, et al. Study of the milling strategy on the tool life and the surface quality for knee prostheses. Journal of Achievements in Materials and Manufacturing Engineering. 2008;31:610–615.

15. Choubey A, Chaturvedi V, Vimal J. Optimization of process parameters of CNC milling machine for mild steel using Taguchi design and Single to Noise ratio Analysis. International Journal of Engineering Research and Technology. 2012;1:1–12.

16. Gimadeev MR, Stelmakov VA, Gusliakov VV. Cutting Forces and Roughness During Ball End Milling of Inclined Surfaces. In: Proc. the 6th International Conference on Industrial Engineering. 2021;2:926–937. https://doi.org/10.1007/978-3-030-54817-9_107

17. Fontaine M, Devillez A, Moufki A, et al. Predictive force model for ball-end milling and experimental validation with a wavelike form machining test. International Journal of Machine Tools & Manufacture. 2006;46:367–380. https://doi.org/10.1016/j.ijmachtools.2005.05.011

18. Lamikiz A, López de Lacalle LN, Sánchez JA, et al. Cutting force estimation in sculptured surface milling. International Journal of Machine Tools & Manufacture. 2004;44:1511–1526. https://doi.org/10.1016/j.ijmachtools.2004.05.004

19. Altintaş Y, Lee P. A general mechanics and dynamics model for helical end mills. CIRP Annals. 1996;45:59–64. https://doi.org/10.1016/S0007-8506(07)63017-0

20. Bouzakis KD, Aichouh P, Efstathiou K. Determination of the chip geometry, cutting force and roughness in free form surfaces finishing milling, with ball end tools. International Journal of Machine Tools & Manufacture. 2003;43:499–514. https://doi.org/10.1016/S0890-6955(02)00265-1

21. Radzevich SP. Formoobrazovanie poverkhnostei detalei. Osnovy teorii. Kiev: Rastan; 2001. 592 p. (In Russ.)

22. Gimadeev MR, Davydov VM. Obespechenie kachestva poverkhnosti pri mekhanoobrabotke slozhnoprofil'nykh detalei. Tekhnologiya Mashinostroeniya. 2018;11:9–16. (In Russ.)

23. Toh CK. A study of the effects of cutter path strategies and orientations in milling. Journal of Materials Processing Technology. 2004;152:346–356. https://doi.org/10.1016/j.jmatprotec.2004.04.382

24. Subrahmanyam KVR, Wong Yoke San, Geok-Soon Hong, et al. Cutting force prediction for ball nose milling of inclined surface. The International Journal of Advanced Manufacturing Technology. 2010;48:23–32. https://doi.org/10.1007/s00170-009-2275-5

25. Wojciechowski S, Chwalczuk T, Twardowski P, et al. Modeling of cutter displacements during ball end milling of inclined surfaces. Archives of Civil and Mechanical Engineering. 2015;15:798–805. https://doi.org/10.1016/j.acme.2015.06.008

26. Ponomarev BB, Nguyen Sy Hien. The influence of tool orientation on cutting forces during end milling. Proceedings of Higher Educational Institutions. Machine Building. 2019. — № 3 (708). — C. 11–20. https://doi.org/10.18698/0536-1044-2019-3-11-20

27. Ponomarev BB, Nguyen Sy Hien. Modeling and analysis of influence of process conditions on cutting forces during end milling. Modern Technologies. System Analysis. Modeling. 2018;59:8–16. https://doi.org/10.26731/1813-9108.2018.3(59).8-16

28. Gimadeev MR, Davydov VM. Correlation of roughness indicators during milling with a spherical tool. Tyazheloe Mashinostroenie. 2018;9:24–29.

29. Davydov VM, Gimadeev MR, Nikitenko AV, et al. Formation of roughness parameters based on correlation relations during finishing milling of spatially complex surfaces. Strengthening Technologies and Coatings. 2019;174:243–248.

30. Ponomarev BB, Paikin DB. Selection of optimum strategy parameters for milling surfaces of a complex shape. iPolytech Journal. 2010;46:52–56.

31. Arshanskiy MM, Shcherbakov VP. Vibrodiagnostika i upravlenie tochnost'yu obrabotki na metallorezhushchikh stankakh. Moscow: Mashinostroenie; 1983. 136 p. (In Russ.)

32. Davydov VM, Zayev VV, Panochevnyi PN, et al. Analysis of international practice profile and three-dimensional evaluation of surface roughness. Uchenye Zametki TOGU. 2013;4:1061–1074.

Received 25.04.2022
Revised 19.05.2022
Accepted 25.05.2022

About the Authors:

Gimadeev, Mikhail R., associate professor of the Technical Informatics and Information Systems Department, Pacific National University (136, Tihookeanskaya St., Khabarovsk, 680035, RF), Cand.Sci. (Eng.), ScopusID, ORCID, 009063@pnu.edu.ru

Li, Andrey A., teaching assistant of the Technical Informatics and Information Systems Department, Pacific National University (136, Tihookeanskaya St., Khabarovsk, 680035, RF), ORCID, 011864@pnu.edu.ru

Claimed contributorship

M. R. Gimadeev: research objectives and tasks setting; basic concept formulation; methodical description of equations; analysis of the research results; text preparation; correction of the conclusions. A. A. Li: experiment planning; solving research problems; conducting the experiment and computational analysis; the text revision; formulation of conclusions.

Conflict of interest statement

The authors do not have any conflict of interest.

All authors have read and approved.

MACHINE BUILDING AND MACHINE SCIENCE

Check for updates

UDC 62-19

https://doi.org/10.23947/2687-1653-2022-22-2-130-141

Original article

Determination of the Dynamic Characteristics of a Gear Pump by the Load Variation Method Using Special Bench Systems

Valeriy I. Sanchugov, **Pavel D. Rekadze** ✉

Samara National Research University, 34, Moskovskoye Shosse,Samara, Russian Federation

✉ Rekadze1993@gmail.com

Abstract

Introduction. Some of the major factors in the occurrence of vibration of units, causing fatigue failure of the housings of elements, pipelines, and failure of pump elements, are pulsations of the working medium in the hydraulic systems of machine tools, fuel feed systems of aircraft engines and liquid-propellant engine supply. This study aimed at the implementation of a method for determining the dynamic characteristics of a volumetric pump using special bench systems, and the comparison of the calculation results to the experimental data. The stages of calculating the dynamic characteristics of a volumetric pump were described, taking into account the pre-developed special bench systems on the example of an external gear pump with a capacity of 14 cm^3/rev. The implementation of V. P. Shorin's load variation method using special bench systems developed by the authors with predetermined dynamic characteristics was shown. The main stages of the methodology for determining the dynamic characteristics of a gear pump were described.

Materials and Methods. Methods of spectral analysis of pulsating pressure were applied in the work. Pulsations of fluid flow at the pump outlet were determined using the impedance method, the method of load variation, and special bench systems.

Results. The paper implemented a technique for determining the dynamic characteristics of a gear pump in the drive shaft speed range of 500-2500 rpm for four harmonic components of the vibration spectrum in a wide range of dynamic loads (from inertial to capacitive nature). The bench systems yielding the calculation of the dynamic characteristics of the pump with a minimum error based on the condition of matching the dynamic load and the source of vibrations were analyzed. The developed approach to the evaluation of the dynamic characteristics of the pump was verified through comparing the calculated and experimental data of pressure pulsations in the bench systems with choke, cavity and an extended pipeline at the pump outlet.

Discussion and Conclusions. The method for determining the dynamic characteristics of a volumetric pump was implemented using special bench systems developed by the authors. The research results show that the gear pump under study can be considered as an independent source of flow fluctuations, for which the deviation of its own dynamic characteristics from the average values does not exceed 10% for the first harmonic component.

Keywords: volumetric pump, load variation method, bench systems, source of flow fluctuations, pump dynamic characteristics, independent source of fluctuations, flow pulsations, impedance.

Acknowledgements: the authors would like to thank the reviewers for the comments, which contributed to quality of the article – the research of the second author was carried out on theme no. FSSS-2020-0015 within the frame of the government task of the Ministry of Education and Science of the Russian Federation.

For citation: V. I. Sanchugov, P. D. Rekadze. Determination of the dynamic characteristics of a gear pump by the load variation method using special bench systems. Advanced Engineering Research, 2022, vol. 22, no. 2, pp. 130–141. https://doi.org/10.23947/2687-1653-2022-22-2-130-141

Introduction. The main disadvantages of pumps are the acoustic noise that accompanies their operation, the vibration of the body, connected pipelines, and the resulting structural damage.

The traditional way of improving pump designs, used in mechanical engineering and consisting in smoothing out the uneven flow of the liquid, is hampered by the lack of means of direct measurement of fluid flow at the pump outlet. This limits any experimental evaluation of the design efficiency and finishing work on pumps. In addition, this limits the analytical description of the pump as a source of vibrations required by hydraulic system developers to provide the target dynamic quality of the systems by themselves.

For this reason, the research on the modeling of dynamic processes in hydromechanical systems [1, 2] and the application of new approaches to solving problems of hydraulic system dynamics [3, 4] based on physical principles are pressing issues.

Materials and Methods. The implementation of V. P. Shorin's method of load variation [4] is presented. It consists in determining pressure pulsations behind a pump interacting with several bench systems, whose dynamic characteristics are calculated in advance. Further, the processed frequency-response functions of the pressure using the impedance of the bench systems are recalculated into the pump's own dynamic characteristics — pulsation performance and impedance. The development of the approach provides that special bench systems are proposed. They take into account the connecting fittings, adapters and internal channels of the pump, which makes it possible to more accurately determine the dynamic characteristics of pumps, as well as to verify the applicability of the pump model used in the form of an equivalent source of vibrations.

Research Results

Method for determining the dynamic characteristics of a gear pump

Samara University has developed a computational and experimental method for determining the dynamic characteristics of a gear pump (pulsation performance and impedance), which is based on the research of L. Thévenin, E. Norton and V. P. Shorin [5, 6]. The developed methodology includes the following main stages: creation of models and calculation of dynamic characteristics of special bench systems; experimental determination of pressure pulsations at the pump outlet; calculation of the spectrum of excited vibrations in various bench systems; determination of approximating dependences for individual harmonic components; calculation of the pump own dynamic characteristics (pulsation performance and impedance); evaluation of the independence (stability) of the dynamic characteristics of the pump from the characteristics of bench systems; verification of the applicability of the pump model used as an equivalent source of flow (or pressure) fluctuations. The following is an example of the implementation of the proposed technique using an external gear pump with a specific capacity of 14 cm^3/rev.

Models and calculation of dynamic characteristics of special bench systems

Basic options of bench systems at the liquid outflow during pump tests were considered. In concentrated parameters, the bench system can implement active flow-dependent, inertial, and elastic loads. In distributed parameters, the bench system can be provided in the form of an extended cylindrical pipeline implementing an active frequency-independent non-reflective load.

Pump models in the form of equivalent source of flow fluctuations (ESFF) or pressure (ESPF) are determined using constant flow source Q_0, an ideal source of pressure fluctuations p (or flow q) and internal impedance Z_u [4]. Figure 1 shows pump models in the form of an equivalent source of pressure fluctuations (and flow) with an attached system.

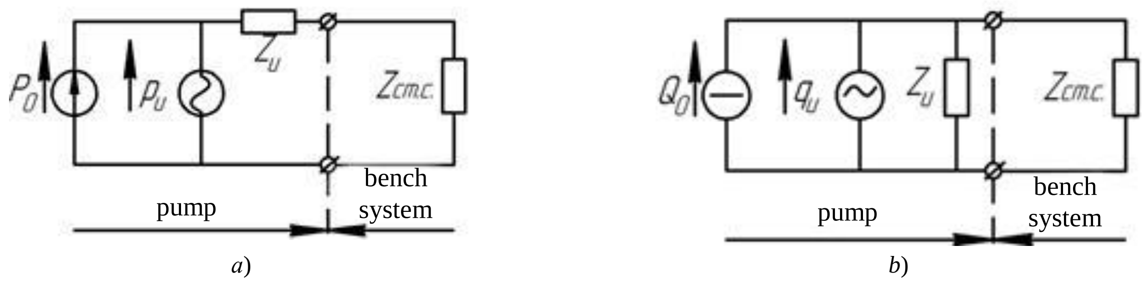

Fig. 1. Pump models in the form of an equivalent source of: *a* — pressure fluctuations; *b* — flow with attached system Q_0, P_0 — average flow and pressure; p_H, q_H — pump's own pulsating performance in terms of pressure and flow, $Z_u, Z_{cm.c.}$ — impedance of pump and bench system (adapted from [4])

In this connection, the task of selecting a bench system is to provide such system parameters at which the best conditions for high measurement accuracy are realized. The task of selecting the parameters of the attached system should be carried out when the impedance changes in the range from -∞ to +∞.

Figure 2 shows schematic diagrams of the bench systems.

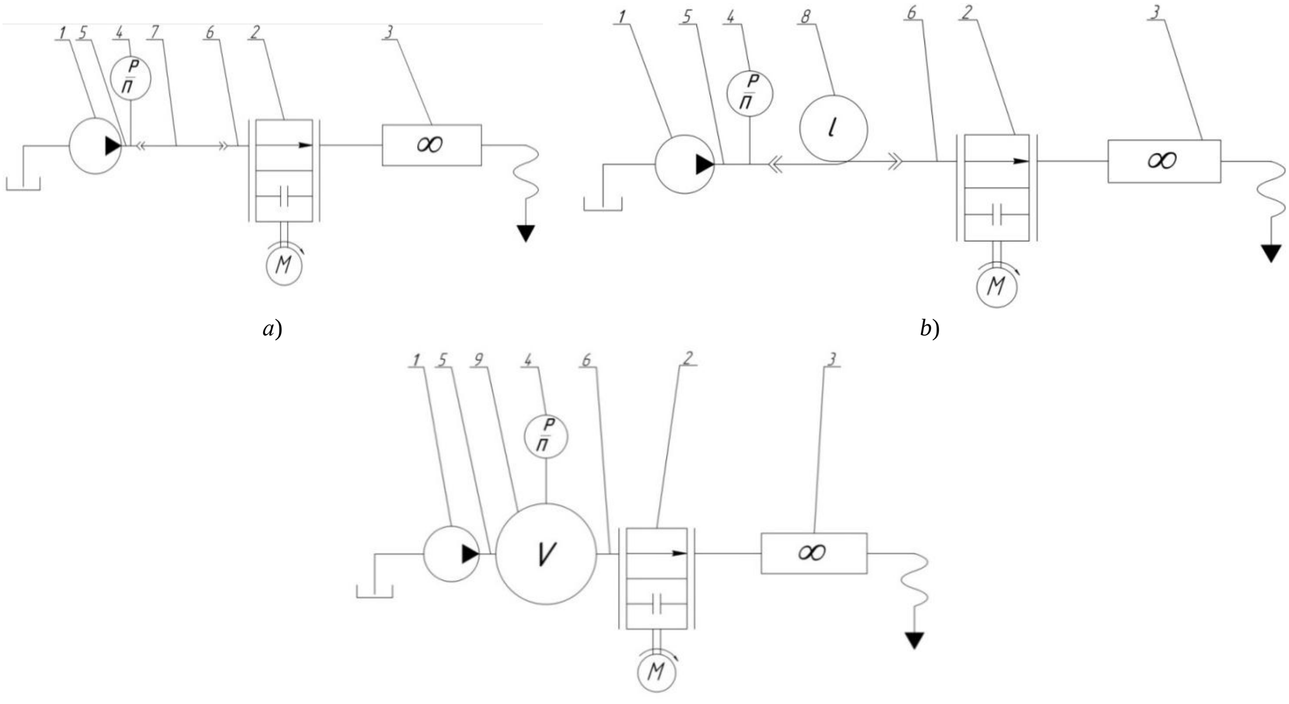

a) *b*) *c*)

Fig. 2. Schematic diagrams of the bench systems for determining own dynamic characteristics of pumps: *a* — with active throttle load; *b* — with active non-reflective load; *c* — with capacitive load: 1 — test pump; 2 — load choke; 3 — flow meter; 4 — pressure sensor; 5, 6 — connecting fittings; 7 — main line; 8 — extended pipeline; 9 — cavity

Computational models of impedances of special bench systems:

− with active throttle load (throttle):

$$Z_{ст.с.k}\left(Q_0, f\right) = \sqrt{(Z_{др}\left(Q_0\right) + ReZ_{тр}\left(Q_0\right))^2 + \left(2\pi f_k \frac{\rho l_\Sigma}{S_{тр}}\right)^2}\, e^{j arctg \frac{2\pi f_k \frac{\rho l_\Sigma}{S_{тр}}}{Z_{др}\left(Q_0\right) + ReZ_{тр}\left(Q_0\right)}}, \quad (1)$$

− with active distributed load (extended pipeline):

$$Z_{ст.с.} = \frac{\rho a}{S_{тр}}, \quad (2)$$

− with capacitive load (cavity):

$$Z_{ст.с.k}\left(Q_0, f_k\right) = \sqrt{\left(ReZ_{лам}\left(Q_0\right) + ReZ_{турб}\left(Q_0\right) + ReZ_{м.с.}\left(Q_0\right) + Z_{др}\left(Q_0\right)\right)^2 + \left(\frac{\left(2\pi f_k\right)^2 LC - 1}{2\pi f_k C}\right)^2} * \quad (3)$$

$$* e^{j arctg\left[\frac{\left(2\pi f_k\right)^2 LC - 1}{2\pi f_k C\left(ReZ_{лам} + ReZ_{турб}\left(f_k\right) + ReZ_{м.с.}\left(f_k\right) + Z_{др}\left(Q_0\right)\right)}\right]}$$

The formulas indicate: $Z_{др}\left(Q_0\right)$ — impedance of the throttle; $ReZ_{тр}(Q_0)$ — real part of the impedance of the pipeline, including the connecting line, fittings, internal channels in the pump and throttle; $ReZ_{лам}(Q_0), ReZ_{турб}(Q_0), ReZ_{м.с.}(Q_0)$ — real part of the impedance of the fittings and the internal channel in the pump and cavity with laminar, turbulent fluid flow behind the pump and local resistances, respectively; f_k — frequency k — *th* of the harmonic component of the vibration spectrum behind the pump; ρ — density of the working environment; l_Σ — pipeline length, including the length of main line 6, connecting fittings 5 and 7 and internal channels of the pump and throttle (not shown in Fig. 7); $S_{тр}$ — cross-sectional area of the pipeline; L — "inertia" of the connecting fittings and the internal channel in the pump and cavity; C — elasticity of the cavity; k — number of the harmonic component of the vibration spectrum; j — imaginary unit ($j = \sqrt{-1}$).

Using a bench system with a throttle at the pump outlet, three inertially active dynamic loads were implemented, in which the active resistance was changed through changing the overlap area of throttle F_0:

− for bench system no. 1, overlap area F_{01}=9.290×10^{-6} m^2,

− for bench system no. 2, overlap area F_{02}=7.299×10^{-6} m^2,

− for bench system no. 3, overlap area F_{03}=2.247×10^{-5} m^2.

Using a bench system with a cavity at the outlet of the pump with a volume of 2 liters, an inertial elastic dynamic load was realized.

An active frequency-independent load was implemented using a bench system with an extended pipeline length of 106 m.

The dependences of the impedance (module and phase) on the frequency were calculated according to the models of bench systems using formulas (1)–(3). Table 1 for the 1st harmonic shows the regression functions of the impedance module of the bench system $Z_i(f)$ and phases $\beta_i(f)$ for the analyzed bench systems.

Table 1

Regression functions of dynamic characteristics of bench systems according to the 1st harmonic

No. of stand system according to Figure 2	Bench system type	Bench system impedance module Z_i (f), $\frac{kg}{m^4 s^2}$	Bench system impedance phase β_i (f), rad
a – no.1	With throttle at pump outlet	$1.412\cdot10^7 f + 2.201\cdot10^9$	$7.066\cdot10^{-4} f + 0.199$
a – no.2		$1.610\cdot10^7 f + 4.258\cdot10^9$	$6.906\cdot10^{-4} f + 0.09039$
a – no.3		$4.980\cdot10^7 f + 1.503\cdot10^9$	$2.723\cdot10^{-3} f + 0.251$
b – no.4	With cavity at pump outlet	$3.308\cdot10^4 f^2 – 1.416\cdot10^7 f + 1.873\cdot10^9$	$arctg(\frac{4.234\cdot10^6 f + 1.495\cdot10^9}{1.430\cdot10^5 f + 2.930\cdot10^6})$
c – no.5	With extended pipeline at pump outlet	$1.897\cdot10^{10}$	0

Experimental determination of pressure pulsation at the pump outlet

The background information for determining the dynamic characteristics of the pump was the measurement of pressure at the pump outlet. An example of an oscillogram and a pressure pulsation spectrum at the pump outlet in the bench system with an active distributed load is shown in Figure 3. Operating mode of the pump in this case is as follows: average pressure $P_0 = 23.8$ MPa, drive shaft speed $n = 1000\,rpm$.

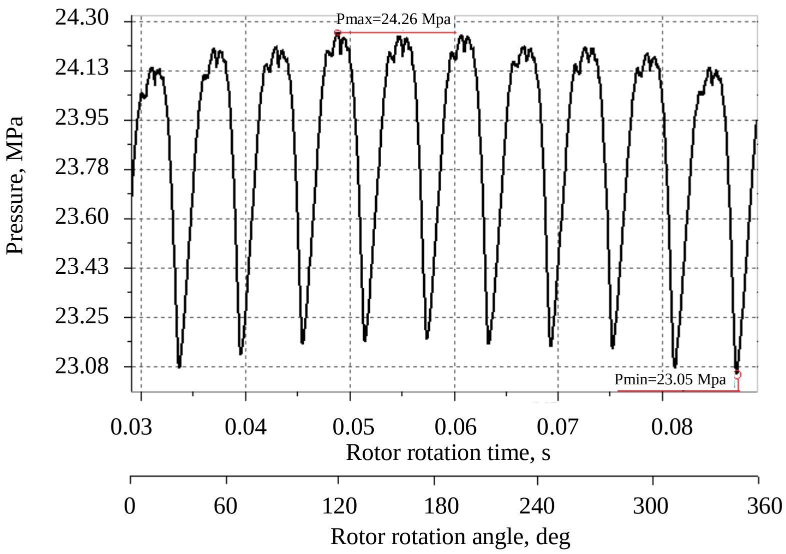

a)

Machine building and machine science

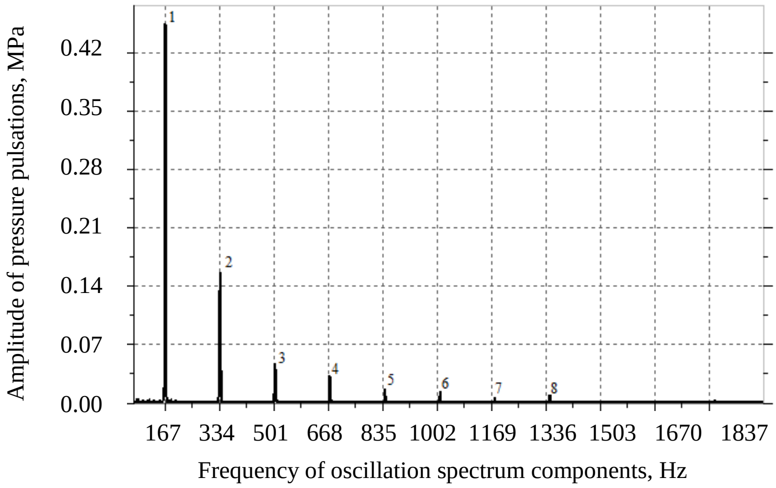

b)

Fig. 3. Pressure at the pump outlet: *a* — oscillogram; *b* — spectrogram

The amplitude-frequency response of pressure pulsations at the pump outlet in the speed range of the pump drive shaft n=500–1250 rpm is shown in Figure 4. The regression functions built in the *Microsoft Excel* environment using the Trendline tool are plotted with a solid line.

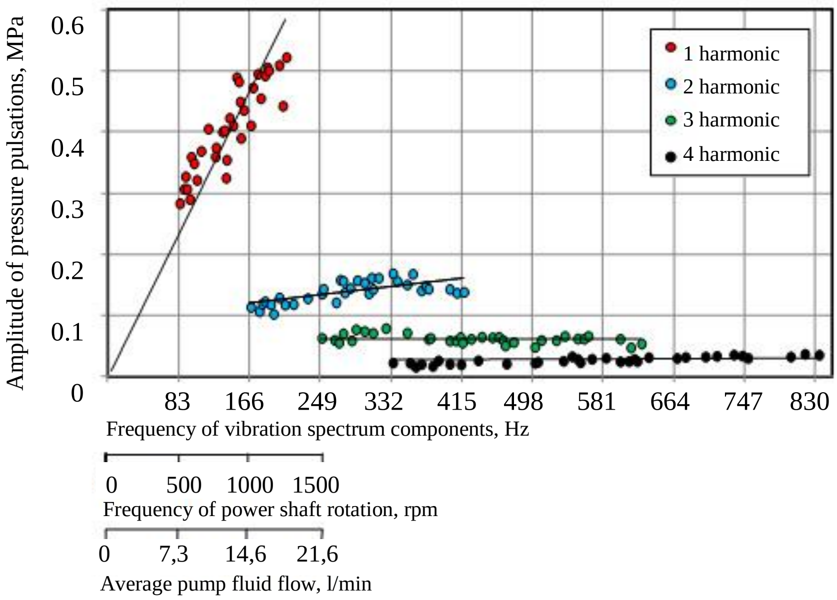

Fig. 4. Amplitude-frequency response of pressure pulsations at the pump outlet by individual harmonic components (dots indicate data on: ● — first, ● — second, ● — third, ● — fourth harmonics, lines indicate regression functions)

The analysis of the oscillogram, spectrogram and amplitude-frequency response of pressure pulsations showed the following: the type of process was polyharmonic steady; the number of recorded harmonics was 8, analyzed[1] — 4; the amplitude range of pressure fluctuations was 0.28–0.52 MPa; the drive shaft frequency range was 500−1250 rpm, the analyzed harmonic components of the spectrum 83–833 Hz.

Fourier series expansion was used for harmonic analysis of periodic signals [7]. To decompose into a Fourier series, sections of the pressure oscillogram measured relative to the reference signal at the rotor frequency were used, i.e., one section of the oscillogram was extracted for a full rotation of the rotor. The reference signal was recorded at a fixed gear position, set at the beginning of recording the pressure waveform for five bench systems. In this way, the amplitude-frequency (FRF) $A_k(\omega)$ and phase-frequency (PFC)$\varphi_k(\omega)$ characteristics were determined.

[1] It is assumed in the work that the extreme highest analyzed harmonic in amplitude should not be more than 5 % of the amplitude of the first harmonic.

Calculation of the spectrum of excited vibrations in various bench systems and determination of approximating for individual harmonic components of pressure fluctuations

Based on the experimental determination of pressure in five bench systems: with a throttle (no.1–3), with a cavity (no.4) and an extended pipeline (no.5) at the pump outlet, the spectra of excited vibrations were calculated. Table 2 shows the regression functions of the amplitudes $A_p(f)$ and the initial phases of pressure pulsations for the 1st harmonic.

Table 2

Regression functions of amplitudes and initial phases of pressure fluctuations

No. of stand system according to Figure 2	Bench system type	Pressure pulsation amplitude A_{pi} (f), $\frac{kg}{ms^2}$	Initial phase of pressure pulsations φ_i (f), rad	Frequency range
a – no.1	With throttle at pump outlet	$1.003 \cdot 10^{-3}f$	–0.543	83–417
a – no.2		$1.243 \cdot 10^{-3}f$	–0.280	
a – no.3		$6{,}129 \cdot 10^{-4}f$	–5.941	
b – no.4	With cavity at pump outlet	$1.343 \cdot 10^{-6}f^2 – 4.298 \cdot 10^{-4}f + 3.913 \cdot 10^{-2}$	–5.373	
c – no.5	With extended pipeline at pump outlet	$2.694 \cdot 10^{-3}f$	–0.658	

Calculation of the dynamic characteristics of the pump

To calculate the dynamic characteristics of the pump (impedance and pulsation performance of the source), it is required to conduct an experiment with at least two dynamic loads[2]. Therein, according to the model of an equivalent source of flow fluctuations refined by the authors using analytical dependences $p_i(f)$ and $Z_i(f)$ from Tables 1 and 2, the pump impedance is calculated from the formula:

$$Z_u = Z_1 \frac{1 - \frac{p_1}{p_2}}{\frac{p_1}{p_2} - \frac{Z_1}{Z_2}}, \tag{4}$$

where Z_u — pump impedance; ($Z_u = |Z_u| e^{j\varphi_u}$) — pump impedance module; ($|Z_u| = \sqrt{ReZ_H{}^2 + ImZ_H{}^2}$), ReZ_u, ImZ_u — real and imaginary part of pump impedance; φ_u — pump impedance argument; Z_1, Z_2 — input impedance of dynamic loads no. 1–2; ($Z_1 = |Z_1| e^{j\beta_1}, Z_2 = |Z_2| e^{j\beta_2}$), β_1, β_2 — impedance arguments of dynamic loads no. 1–2; p_1, p_2 — pressure pulsations behind the pump in bench system no. 1–2; ($p_1 = A_{p1} e^{j\varphi_1}, p_2 = A_{p2} e^{j\varphi_2}$), A_{p1}, A_{p2} — amplitudes of flow pulsations behind the pump in bench system no. 1–2; φ_1, φ_2 — initial phases of pressure pulsations of dynamic loads no. 1–2.

Then, using the analytical dependences from Tables 1 and 2, the pulsation capacity of the pump was determined according to the model of an equivalent source of vibrations refined by the authors (variable component of volumetric flow q_u and pressure p_u):

$$q_u = \frac{p_2}{Z_2} \frac{1 - \frac{Z_2}{Z_1}}{1 - \frac{p_2}{p_1}}, \; p_u = \frac{1 - \frac{Z_1}{Z_2}}{\frac{p_1}{p_2} - \frac{Z_1}{Z_2}}, \tag{5}$$

[2] For a sufficient sample size, it was required to use at least four dynamic loads Z_{ij}, that form six non-repeating (including i ≠ j) combinations: Z_{12}, Z_{13}, Z_{14}, Z_{23}, Z_{24}, Z_{34}.

where q_u, p_u — variable component of the volume flow ($q_u = A_{qu}e^{j\varphi_q}$) and pressure ($p_u = A_{pu}e^{j\varphi_p}$) of the pump; A_{qu}, A_{pu} — pump flow and pressure pulsation amplitude; φ_q, φ_p — argument of the variable component of the volume flow and pressure of the pump.

Of the calculated characteristics according to ESFF ($q_u(f)$) and ESPF ($p_u(f)$) models, using formula (5), only one will be stable, since the equivalent oscillation source has an independent dynamic characteristic only for one of the parameters (pulsating flow or pressure).

The calculation of impedance Z_u and the variable component of the volume flow q_u of the pump was carried out according to formulas (4)–(5) for five dynamic loads, i.e., using ten different combinations of these loads: “1_2”, “1_3”, “2_3”, “1_4”, “2_4”, “3_4”, “1_5”, “2_5”, “3_5”, “4_5” (Table 1).

For further calculation and analysis, a characteristic of the pump flow pulsation amplitudes A_{qu} was obtained from ten flow pulsation amplitude curves. The values of the amplitudes A_{qu} (at each frequency) were calculated using the formula from source [8]:

$$A_{qu} = \overline{A_{qu}} \pm \Delta A_{qu},$$

where $\overline{A_{qu}}$ — average amplitude of pulsating flow; ΔA_{qu} — confidence interval of the amplitude of pump flow pulsations ($\Delta A_{qu} = \frac{t\sigma}{\sqrt{m}}$); σ — standard deviation of the amplitude of the pulsating flow rate from the average value; m — number of dynamic load combinations ($m = 10$); t — Student's coefficient ($t = 2.262$, was calculated for the confidence level 0.95).

The confidence interval of amplitudes ΔA_{qu} was formed from errors (instrument and method) and the degree of dependence of the dynamic characteristics of the pump $A_q(f)$ on the bench system. The instrument error consisted of the error of determining the pressure and phases, the method error included the error of the unaccounted influence of the dynamic properties of the drive mechanical system.

The phases of flow pulsations φ_q and their deviations were calculated in a similar way. When calculating the phases, combinations “1_2” and “1_5” were excluded due to the degeneration of the variable component of the volume flow of the pump q_u when using close values of characteristics at the same frequency: $\varphi_1 \approx \varphi_2$ *and* $\beta_1 \approx \beta_2$.

The results of calculating the intrinsic dynamic characteristic of the pump in the form of pulsation performance and impedance are shown in Figure 5. Phases, for convenience, are presented in degrees.

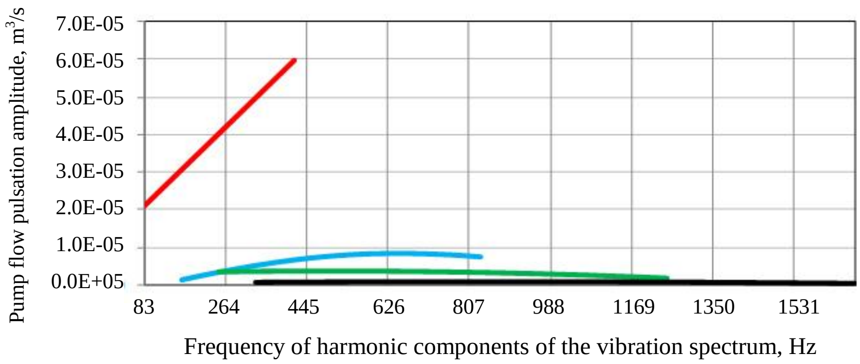

a)

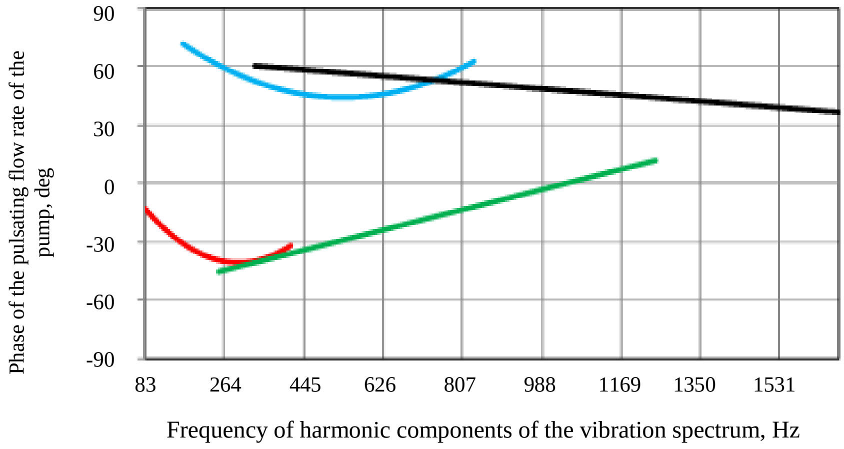

b)

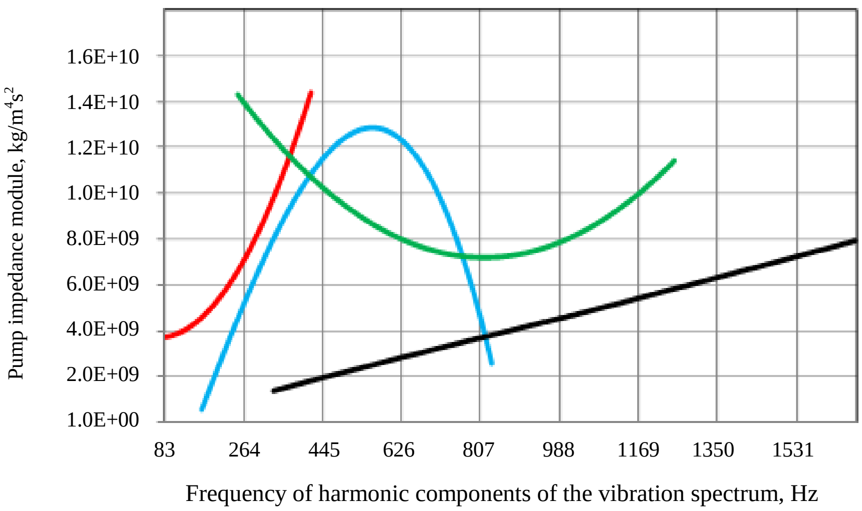

c)

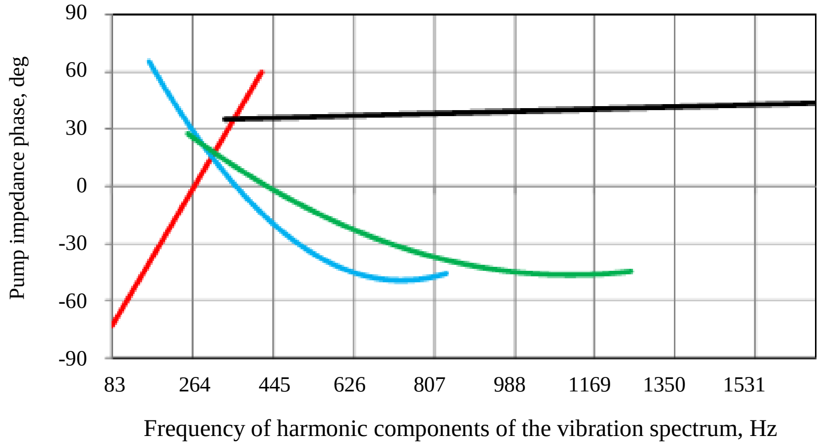

d)

Fig. 5. Dynamic characteristics of the pump: *a* — flow pulsation amplitude; *b* — flow pulsation phase; *c* — impedance modulus; *d* — impedance phase (solid lines indicate data on: — first, — second, — third, — forth harmonics)

The amplitude of the flow pulsations at the 1st harmonic has a monotonically increasing character. With an increase in the harmonic number, the slope of the flow pulsation amplitude curve decreases to an almost constant value to the 4th harmonic. The values of amplitudes A_q at the higher harmonics are by an order of magnitude less than at the 1st harmonic.

The pump impedance module at the 1st harmonic has a monotonically increasing character.

To evaluate the realized dynamic loads, the criterion of matching the impedance module $|Z_u|$ of the oscillation source and the input impedance module of the dynamic load $|Z_{cm.c}|$ was used [99, 10]. The impedance modules should be comparable ($|Z_u| \cong |Z_{cm.c}|$), so that the quantitative values of the dynamic characteristics of the pump were determined with minimal error. For comparison, ratio $\left|\frac{Z_u}{Z_{cm.c.}}\right|$ was used. At $\left|\frac{Z_u}{Z_{cm.c.}}\right| \cong 1$, the dynamic load was considered consistent with the source.

Due to the difference in the curve shapes of the pump impedance modules and dynamic loads in the frequency range of 83–417 Hz, it was rational to use average ratio $\left|\frac{Z_u}{Z_{cm.c.}}\right|_{f_{min}\cdots f_{max}}$, that provided considering the contribution of most of the frequency range, i.e., ratio $\left|\frac{Z_u}{Z_{cm.c.}}\right|_{f_{min}\cdots f_{max}}$ according to the 1st harmonic would be:

− for active throttle load no.1 — 1.16;
− for active throttle load no.2 — 0.8;
− for active throttle load no.3 — 2.65;
− for capacitive load no.4 — 4.64;
− for active distributed load no.5 — 0.35.

That is, the dynamic loads of bench systems no. 1, 2 were the most consistent with the source of vibrations. Thus, the dynamic characteristic of the pump, calculated using dynamic loads of bench systems no.1, 2 (“1_3”, “2_3”, “1_4”, “2_4”, “1_5”, “2_5”) was determined with a minimum error.

Evaluation of the stability of the dynamic characteristics of the pump from the characteristics of bench systems

Stability of the dynamic characteristics A_{qu} and φ_q ($|Z_u|$ and φ_u) of the pump was evaluated using mathematical statistics tools [8]. Thus, the stability of the characteristic A_{qu} was estimated through calculating the ratio of the confidence interval $|\Delta A_{qu}|$ at frequency *f* to the average value of the characteristic $|\overline{A_{quMe}}|$ at this frequency[3]. The resulting relative deviation Δ_q should not exceed the specified deviation $\Delta_{\partial onq}$:

$$\Delta_q = \left|\frac{\Delta A_{qu}}{\overline{A_{quMe}}}\right| \le \Delta_{\partial onq},$$

where $|\overline{A_{quMe}}|$ — average median value of the amplitude of pump flow pulsations; $\Delta_{\partial onq}$ — specified relative deviation of the pump flow rate pulsation amplitude from the average value.

With relative deviation $\Delta_q \to 0$ (when $|\Delta A_{qu}| \to 0$), the stability of characteristic A_{qu} was maximum. Based on the experience of other researchers, it is preferable to select value $\Delta_{\partial onq}$ within 5–30 % [11–17].

For a single-digit evaluation of the dynamic characteristics of the pump, it is rational to use the value of the relative deviation. The calculation of such a value is possible through estimating the average median value of relative deviations in the frequency range of each harmonic ($f_{min} \dots f_{max}$): $\Delta_{qMe} = \left.\frac{\Delta A_{qu}}{\overline{A_{qu}}}\right|_{f_{min}\cdots f_{max}}$. Value Δ_{qMe} is efficiently used, if $\left.\frac{\Delta A_{qu}}{\overline{A_{qu}}}\right|_{f_{min}\cdots f_{max}} \le 0.3$, i.e., when the confidence interval ΔA_{qu} does not exceed 30% of the average amplitude of pulsating $\overline{A_{qu}}$.

The results of assessing the stability of the dynamic characteristics of the pump from the characteristics of the bench systems[4] were: according to the 1st harmonic — 2 %, according to the 2nd — 8 %, according to the 3rd — 15 %, according to the 4th — 48 %. The results of the calculation of the dynamic characteristics of the pump showed that for

[3] Stability of other intrinsic characteristics of the pump is evaluated similarly.
[4] It is required to consider the method error of the approach and the instrument error of determining the pressure.

four harmonics in the frequency range of 500–2500 rpm, the gear pump under study should be considered according to the model of an equivalent source of flow fluctuations.

Checking the applicability of the pump model used as an equivalent source of flow fluctuations

To test the developed approach for evaluating the dynamic characteristics of the pump, a calculated determination of pressure pulsations in bench systems with a throttle, a cavity and an extended pipeline at the pump outlet was performed. Using the found dynamic characteristics of the pump, the amplitudes of pressure pulsations in the analyzed bench systems were calculated, which were compared to the experimental ones. The results of the calculation of amplitudes $A_p(f)$ in a bench system with an extended pipeline are presented below. The amplitudes of pressure pulsations p_i were calculated in accordance with the ESFF model from the formula:

$$p_i = \frac{q_u \cdot Z_u \cdot Z_i}{Z_u + Z_i}, \tag{6}$$

The results of calculating the amplitudes of pressure pulsations behind the pump are shown in Figure 6. The dotted line indicates the amplitudes obtained experimentally, and the solid line — calculated from formula (6).

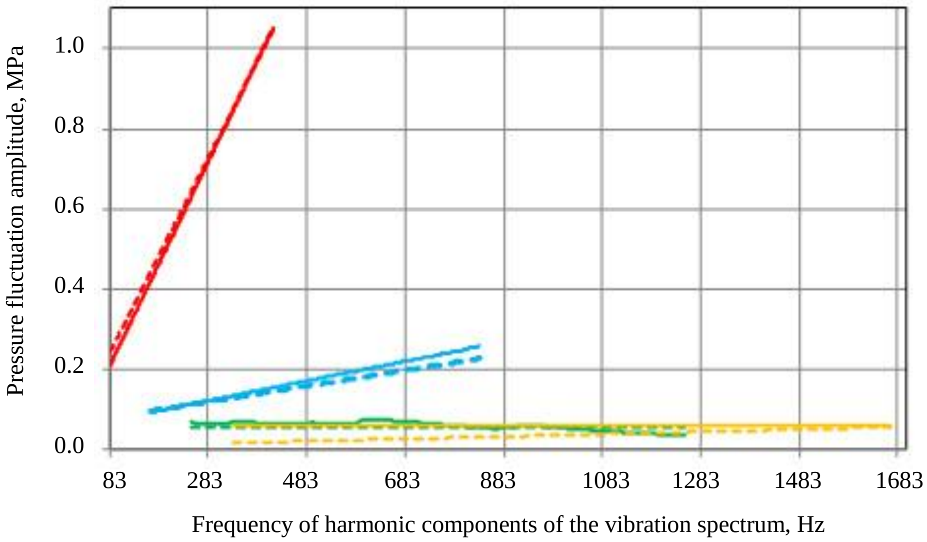

Fig. 6. Pressure frequency response for the bench system with extended pipeline length *l*=106 m (solid lines indicate calculated data on: — first, — second, — third, — forth harmonics; dotted lines indicate experimental data)

Convergence of the results of the verification calculation was evaluated according to the formula of deviation of the difference between the experimental and calculated values from the experimental data. The results of the test calculation for the bench systems with a throttle, a cavity and an extended pipeline at the pump outlet showed that according to the 1st harmonic, the relative deviation from the experimental data for the considered bench systems did not exceed 10 %, the minimum relative deviation was characteristic of a bench system with an extended pipeline at the pump outlet — 2%. The amplitudes of the pressure pulsations of the 2nd–4th harmonics were within the corridor calculated from the formula $A_p = \overline{A_p} \pm \overline{A_p}$ (where $\overline{A_p}$ — the average amplitude of the pulsating pressure).

Discussion and Conclusions. Methodology for calculating dynamic characteristics of the pump in the form of an equivalent source of fluid flow fluctuations was implemented on the example of a gear pump with a capacity of 14 cm^3/rev using special bench systems developed by the authors and an updated model of impedance and pulsation flow rate. It was shown that the investigated gear pump of external gearing was rationally considered according to the model of an equivalent source of flow fluctuations. The proposed approach was verified in the form of calculation of pressure pulsation amplitudes in the bench systems and comparison to experimental values. The deviation of the calculated amplitudes of pressure pulsations from the experimental values did not exceed 10%. It is worth noting that the impact on the dynamic characteristics of the gear pump of the drive mechanical system and the wear of the gear pump parts remained outside the scope of the review. Based on the work carried out, it was possible to formulate directions for the development of the proposed approach:

− assessment of the dynamic characteristics of the gear pump during the entire service life;

− development of a four-pole model of a gear pump as an equivalent source of vibrations, taking into account the mechanical drive and hydraulic output systems;

− development of a gear pump model as an equivalent source of vibrations, taking into account its design features, the displacement process, reverse water hammer in the chamber between teeth, the work of the locked volume, and leakage from the injection area to the suction area.

Here, it is required to expand the nomenclature of the tested volumetric pumps for the entire class of volumetric displacement machines to confirm the operability of the proposed approach.

References

1. Rybak AT, Zharov VP, Fridrikh RA. Modelirovanie i ehksperimental'nye issledovaniya gidromekhanicheskoi sistemy so znakoperemennoi nagruzkoi. Vestnik of DSTU. 2006;6:17–25. (In Russ.)

2. Rybak AT. Ob''emnaya zhestkost' i ee vliyanie na dinamiku gidromekhanicheskoi sistemy. Vestnik of DSTU. 2006;6:200–207. (In Russ.)

3. Ozerskiy AI. Application of Lagrange approach to solving problems of heat power plants hydraulic systems dynamics. Vestnik of DSTU. 2010;10:914–925.

4. Bystrov ND, Gimadiev AN, Golovin AN, et al. Formirovanie dinamicheskikh svoistv truboprovodnykh tsepei. Shorin VP (ed.) Samara: Samara University Publ.; 2020. 328 p. (In Russ.)

5. Staniloiu M, Popescu H, Rezmeriţă G, et al. The equivalent circuits Thévenin and Norton. The Scientific Bulletin of Electrical Engineering Faculty. 2021;21:40–48.

6. Thévenin L. Sur un nouveaux théorème d'électricité dynamique. Comp. Rendus hebdomadaires des Séances de l'Académie des Sci. 1883;97:159–161.

7. Oberguggenberger M, Toft J, Vindas J, et al. (eds.) Generalized Functions and Fourier Analysis. Springer International Publishing AG, 2017. 276 p.

8. Bronshtein IN, Semendyayev KA, Musiol G, et al. Handbook of Mathematics, 5th ed. Berlin: Springer, 2015. 1207 p.

9. Artyukhov AV, Brudkov LI. Osobennosti chastotnykh ispytanii gidravlicheskikh nasosov. In: Interuniversity coll. of sci. papers "Vibratsionnaya prochnost' i nadezhnost' dvigatelei i sistem letatel'nykh apparatov". Kuibyshev: KUAI. 1982;9:12–17. (In Russ.)

10. Sundararajan D. Introductory circuit theory. Switzerland: Springer; 2020. 297 p. https://doi.org/10.1007/978-3-030-31985-4

11. Ichiyanagi T, Nishiumi T, Nakagawa Sh. The temperature characteristics of flow ripple and source impedance in an external gear pump. In: Proc. 10th JFPS Int. Symposium on Fluid Power, 2017. 5 p.

12. Artyukhov AV, Shorin VP. Metodika opredeleniya dinamicheskikh kharakteristik gidravlicheskikh nasosov. In: Interuniversity coll. of sci. papers "Dinamicheskie protsessy v silovykh i ehnergeticheskikh ustanovkakh letatel'nykh apparatov apparatov". Kuibyshev: KUAI; 1988. P. 70–77. (In Russ.)

13. Jinghao Liu. Source flow ripple and source impedance measurement for different hydraulic pumps. In: Proc. 47th Int. Congress and Exposition on Noise Control Engineering (InterNoise 2018). Chicago, Illinois; 2018. 7 p.

14. Liselott Ericson. On Fluid Power Pump and Motor Design – Tools for Noise Reduction. PhD Thesis. Linköping University, Sweden; 2011. 130 p.

15. Bramley C, Johnston DN. Comparison of methods for measuring pump flow ripple and impedance. In: Proc. ASME/BATH 2017 Symposium on Fluid Power and Motion Control. 2017. 11 p. ttp://dx.doi.org/10.1115/FPMC2017-4223

16. Jinghao Liu, Sanghoon Suh, Yuzhen Yang. Hydraulic Fluid-Borne Noise Measurement and Simulation for Off-Highway Equipment. In: Proc. 2017 SAE/NOISE-CON Joint Conf. (NoiseCon 2017), Grand Rapids, MI. 2017;9:435−443.

17. Min Pan, Nigel Johnston, Andrew Plummer, et al. Theoretical and experimental studies of a switched inertance hydraulic system including switching transition dynamics, non-linearity and leakage. Proc. Institution of Mechanical Engineers, Part I: Journal of Systems and Control Engineering. 2014;228:802–815. https://doi.org/10.1177/0959651814548299

Received 27.04.2022
Revised 20.05.2022
Accepted 27.05.2022

About the Authors:

Sanchugov, Valeriy I., professor of the Automatic Systems of Power Plant Department, Samara National Research University (Samara University) (34, Moskovskoye Shosse, Samara, 443086, RF), Dr.Sci. (Eng.), ORCID, Sanchugovv.i@yandex.ru

Rekadze, Pavel D., design engineer of Research Institute-201, Samara National Research University (Samara University) (34, Moskovskoye Shosse, Samara, 443086, RF), ResearcherID, ScopusID, ORCID, Rekadze1993@gmail.com

Claimed contributorship

V. I. Sanchugov: academic advising; basic concept formulation; research objectives and tasks. P. D. Rekadze: basic concept formulation; computational analysis; text preparation; formulation of conclusions; analysis of the research results; the text revision; finalization of conclusions.

Conflict of interest statement

The authors do not have any conflict of interest.

All authors have read and approved the final manuscript.

MACHINE BUILDING AND MACHINE SCIENCE

Check for updates

UDC 621.224
https://doi.org/10.23947/2687-1653-2022-22-2-142-149

Original article

Converting Hydraulic Resistance Energy of the System into Electricity

Aram A. Sahakyan [1] ✉, **Denis A. Butko** [2]
[1] National University of Architecture and Construction of Armenia, 105, Teryan St., Yerevan, Republic of Armenia
[2] Don State Technical University, 1, Gagarin sq., Rostov-on-Don, Russian Federation
✉ sahakyan.aram@nuaca.am

Abstract

Introduction. A gravity conduit with a control valve and a pressure regulator in the gravity water-supply pipe is considered under conditions when the hydraulic regime of the water-supply system is not disturbed. In relation to such a system, the problems of converting the energy of local artificial hydraulic resistance into electricity are investigated.

Materials and Methods. Literature that highlights the possibility of using microturbines for power generation in water systems was studied. The actual values noted by the continuous pressure recorder (logger) for 12 hours were presented, as well as the water consumption by the turbine at a given unit section (the average for a year), and the pressure differential. It was noted that the use of small hydroelectric power plants in water supply systems significantly reduced the cost of their operation. The indicators of water consumption in the hydroturbine unit during the year, broken down by months, were given. The maximum power at the turbine inlet was calculated. The principles of selecting the type of hydraulic turbine were described. The average efficiency values for different elements of the hydroturbine plant, the average parameters of the power of the small hydro and the corresponding indicators of the average monthly electricity generation were indicated.

Results. Equipping the units under study with specially designed turbines can enable to obtain electrical energy through converting artificially created by local resistance and extinguished mechanical energy. It is possible to apply the approaches described in this article when replacing many of the pressure control units of the Yerevan City Network system. The productivity of a small hydro power plant was predicted, as well as the terms of its construction and operation — for 2 years and 30 years, respectively. The construction and maintenance costs were calculated in advance. The expected data on income, expenses, and net profit are given. It is indicated that it will potentially be close to 6 million drams per year. The analysis of the data allowed us to conclude that the internal rate of return will be at the level of 10.4%, and the payback period is 9 years.

Discussion and Conclusions. We recommend replacing the regulator with a hydroturbine having the same hydraulic resistance and automatic flow control in the system. The conclusions were confirmed by the energy and economic indicators of the hydroturbine plant located on the section of the Arzakan — Yerevan main water pipeline.

Keywords: hydraulic resistance, energy, hydroturbine, adjuster, water supply, energy efficiency indicator, renewable energy sources, pressure control, expert systems.

Acknowledgements: the authors would like to thank the reviewers, whose critical evaluation of the submissions and suggestions for improvement contributed significantly to the quality of this article.

For citation: A. A. Sahakyan, D. A. Butko. Converting Hydraulic Resistance Energy of the System into Electricity. Advanced Engineering Research, 2022, vol. 22, no. 2, pp. 142–149. https://doi.org/10.23947/2687-1653-2022-22-2-142-149

Introduction. Traditional non-renewable primary energy sources, which are very limited in resources, continue to play a dominant role in the Armenian economy. The active use of fossil energy sources has caused environmental problems such as air and soil pollution, water scarcity, and ecosystem degradation. Population growth, continuous household and industrial energy consumption should be taken into account. All this suggests that further quantitative (extensive) development of the energy industry is inexpedient. The use of renewable energy sources to replenish the overall energy balance of the country is an imperative of the time. This approach makes it possible to provide sustainable development while preserving the environment. Water and energy resources are essential for human life and are subject to regular economic, technological, demographic, and social impacts [1]. According to some estimates, 2–3 % of the world's electricity consumption comes from water systems (WS) [2], and pumping units are used in 80–90 % of cases. The costs of their maintenance are among the main operating costs of WS [2]. The concept of rational and efficient use of water resources and electricity is of strategic importance for sustainable development and climate change mitigation. Rational use of water and electricity is hampered by weak infrastructure and outdated operating procedures. This is especially true for developing countries. Moreover, in line with the Millennium Development Goals[1], there is a need for alternative solutions: the goal is to halve the number of people without sustainable access to clean water and basic sanitation. As renewable energy sources, it is proposed to put into operation small hydroelectric power plants (SHPP) in sections of the water supply network with local hydraulic resistance, subject to semi-open valves or pressure regulators. This is cost-efficient for the production of electricity and water supply, and illustrates perfectly the rational use of water resources. In the past decades, hydroelectric power was one of the main sources of energy from water. Today, the water sector is considered a direct consumer of electricity, and this affects the distribution of water resources[2]. Active energy consumption directly affects the state of water resources in the world, which in turn is the cause of climate change. Rational use of energy should contribute to sustainable development through the competent distribution of energy resources at all stages of transformation. For a comprehensive assessment of the problem, an example of the construction of the SHPP on the Arzakan —Yerevan water pipeline is given.

Materials and Methods. The Arzakan-Yerevan water pipeline supplies water to the administrative districts of Yerevan (Arabkir, Malatia-Sebastia, Achapnyak, Erebuni) and adjacent settlements (Zovuni, Kanakeravan, Nor-Achin, Nor-Gekhi, Yeghvard, etc.). The water pipeline originates from the Arzakan spring, and on the territory of the Getamej administrative community, it is divided into two water pipelines with different pressure conditions. The construction of the SHPP on one of the branches of this water pipeline feeding the north-western and western districts of Yerevan is being considered. The company operating on the dividing branch of the water pipeline installed a semi-open valve to

[1] Millennium Development Goals. United Nations URL: https://www.un.org/development/desa/ru/millennium-development-goals.html (accessed: 05.06.2022) (in Russ.)

[2] Mao Yushi, Sheng Hong, Yang Fuqiang. The true cost of coal. Understanding China's Energy Landscape. 2008. URL: https://www.understandchinaenergy.org/greenpeace-chinathe-china-sustainable-energy-programwwf-china-main-authors-mao-yushi-sheng-hong-yang-fuqiang-2010-the-true-cost-of-coal-full-report/ (accessed: 05.06.2022).

adjust the water flow in the system. This provides the pressure in the water supply for settlements located above the main highway (adjacent to the city of Nor-Achin). When the valve is semi-open, a local hydraulic resistance of about 13 m of water column (w.c.) is created (before that, the pressure in the water pipe was about 33 m w.c.).

We propose to install a SHPP instead of a semi-open valve, without disturbing the normal hydraulic mode of operation of the water supply system. Figure 1 shows a plan of the area in the Google Earth program, and Table 1 summarizes the actual values recorded by the continuous pressure recording device (logger) for 12 hours.

Fig. 1. Map of the area in Google Earth

Table 1

Data from pressure recorders installed in the study area

Research Date	Time	Registered pressure (m H2O)	
		Before semi-open valve	After semi-open valve
15.09.2020	20:00	32.8	13.0
15.09.2020	21:00	33.2	12.6
15.09.2020	22:00	33.3	13.0
15.09.2020	23:00	33.3	13.0
16.09.2020	00:00	33.5	12.8
16.09.2020	01:00	33.8	12.4
16.09.2020	02:00	33.9	13.2
16.09.2020	03:00	33.9	13.1
16.09.2020	04:00	33.9	13.6
16.09.2020	05:00	33.8	13.3
16.09.2020	06:00	33.8	13.2
16.09.2020	07:00	33.7	12.6
16.09.2020	08:00	33.4	13.0

The proposal aims at providing the transformation of hydraulic energy artificially created in the local resistance unit into electrical energy. Favorable conditions are created at the construction site of a small hydroelectric power plant (on a branch of the Arzakan-Yerevan main water pipeline) for the integrated use of water and energy potential. The flow rate of the turbine in this section of the assembly is 1.15 m^3/s (average during the year). The control device on the pipe provides a given flow rate. As a result, pressure drops from 20.3 m w.c. to 21.4 m w.c. (Table 1). The expediency of the practical use of the so-called "hidden" energy generated in the sections of main water pipelines in the Republic of Armenia should be noted. The hydropower potential of water supply systems has long been known, but not properly explored. The literature describes in detail the possibilities of using microturbines to generate electricity in water supply systems [3−5]. Gravity systems in areas with high slopes form significant pressures in water supply and distribution networks, creating the prerequisites for generating hydroelectric power. Turbines installed in water distribution networks can also be used as pressure control systems. To do this, pressure relief valves (PRV), which control water losses and leaks, are used [6]. They dissipate energy, thus reducing the pressure in the system. As for water turbines, they can convert excess pressure into electricity[3]. Major advantages of hydraulic energy recovery in water pipes, according to F. Vieira and J. S. Ramos [3, 7], are improving the energy efficiency of the system through the use of local sources, and reducing dependence on external (grid) energy. In addition, hydraulic energy recovery contributes to an overall reduction in operating costs. F. Vieira and J. S. Ramos [3, 7] emphasize in their research that the use of small hydroelectric power plants in water supply systems reduces significantly the cost of their operation. This is due to the fact that the proposed solution enables to replace the control valve with a hydraulic turbine equal in hydraulic resistance. Table 2 shows the water consumption in the system (monthly averages are indicated).

Table 2

Water consumption in the hydroturbine unit

Month	Consumption, m^3/s		
January	1.20	July	1.30
February	1.10	August	1.30
March	1.10	September	1.05
April	1.00	October	1.05
May	1.10	November	1.10
June	1.30	December	1.20

Note that the maximum head is Hmax = 21.4 m, the minimum — Hmin = 20.3 m.

Average annual consumption, according to Table 2: Q = 1.15 m^3/s.

With a design head equal to H = 20 m, the flow power at the turbine inlet [12]:

$$N = \rho q Q H = 1000 \cdot 9.81 \cdot 1.15 \cdot 20 = 225632 \text{ Вт} \approx 225 \text{ kW}.$$

Principles for selecting a hydro turbine. With a low head and a higher flow rate (for SHPP), a turbine with a high specific speed should be selected. Of the reaction turbines, an axial jet turbine will do. Of the low-power active turbines, Banki turbine should be chosen to pass a relatively large flow rate. However, in this case, it is unacceptable to use an active turbine, since when it is filled, excess pressure is formed at the outlet, and Banki turbine operates as a very poor jet turbine with very low energy performance.

[3] The Millennium Development Goals Report 2011. United Nations. New York, 2011. URL: https://www.un.org/millenniumgoals/pdf/(2011_E)%20MDG%20Report%202011_Book%20LR.pdf (accessed: 05.06.2022).

It is recommended to install the hydro turbine unit at the valve on the bypass line. Inlet and outlet valves will provide uninterrupted operation of the line even in the event of a station shutdown. The operation of the SHPP will be monitored by pressure sensors installed at the inlet and outlet of the turbine. This maintains the required pressure on the line[4]. When installing equipment on drinking water mains, special requirements should be taken into account [8-10]. Specifically, contamination of the water with lubricating oils and other materials[5, 6] must be avoided. In general, the distributed water should meet the quantitative and qualitative standards of drinking, domestic, and industrial consumption [11].

Energy indicators of SHPP. The following average efficiency values are applied for different elements of the hydro turbine installation: $\eta_{т} = 0.86$, $\eta_{ген} = 0.94$.

Turbine shaft power: $N_z = \eta_z N = 0.86 \cdot 225 = 193.5$ kW, and at the generator output: $N_{ген} = \eta_{ген} N_z = 0.94 \cdot 193.5 =$ 184 kW.

Table 3 presents the averaged parameters of the power of the SHPP and the corresponding indicators of the average monthly electricity generation.

Table 3

Average monthly capacity and output of SHPP

Month	Power, kW	Output, kWh
January	190	141,360
February	174	116,930
March	174	129,456
April	158	113,760
May	174	113,456
June	206	148,320
July	206	153,264
August	206	153,264
September	166	119,520
October	166	123,504
November	174	125,280
December	190	141,360
	Total	1,573,474

It should be noted that the use of a SHPP jet turbine at a large negative suction height ($h_S = -13$ m), in our opinion, is proposed for the first time in world practice. In this case, on the one hand, the occurrence of cavitation is

[4]Markaryan AYa, Tokmadzhyan VO. Regulirovanie proizvoditel'nosti nasosov s tsel'yu predotvrashcheniya kavitatsionnykh yavlenii. In: Proc. 7th Int. Congress “Water: Ecology and Technology”. Moscow: EHKVATEHK-2006. Part 1. P. 566. (In Russ.)

[5]Sanitarakan Kanonner yev Normer N2-III-A2-1, Khmelu jur: Jramatakararman kentronats’vats hamakargeri jri vorakin nerkayats’vogh higiyenik pahanjner, Voraki hskoghut’yun, Yerevan, 2002t, ej 11. (In Armenian)

[6] Barry JA. Watergy: Energy and Water Efficiency in Municipal Water Supply and Wastewater Treatment Cost-Effective Savings of Water and Energy. The Alliance to Save Energy. Washington, 2007. 44 p.

excluded [9, 12], which, undoubtedly, is regarded positively. On the other hand, it is not known how the high pressure at the outlet of the turbine affects the efficiency, therefore, in our calculations, a slightly underestimated indicator is used.

Research Results. The electricity produced by the SHPP (Table 3) is planned to supply to the general energy system of the Republic of Armenia on the terms of guaranteed purchase at prices approved by the Commission on Regulation of Public Services of Armenia (currently, the tariff is 10.579 drams per kWh).

According to Table 3, during the year, the SHPP will produce at least 1.5 million kWh. According to preliminary calculations, the construction period of the SHPP is 24 months, and the service life is 30 years. The cost of construction and design of the SHPP will amount to 60.4 million drams (Table 4).

Table 4

SHPP construction costs

Works	Cost, AMD mln
Pipeline construction / maintenance	2.2
Construction of the HPP building	14.5
Cost of installing hydraulic units (hydro turbines, generators)	18.0
Transformer substation	10.7
Construction of high voltage power lines	3.0
Design and calculation work	7.0
Other costs	5.0
Total	60.4

Anticipated revenues, operating costs, and profit are shown in Table 5.

Table 5

Forecast of annual financial indicators

Indicator	Amount, AMD mln
Gross income	15.9
Salary, operating expenses, current repairs, and elimination of accidents	7.0
Duties and other obligatory payments	0.2
Depreciation costs (taking into account 30 years of operation)	2.0
Other costs	0.2
Profit before income tax	7.4
Income tax	1.5
Net profit	5.9

The data on annual expenses presented in Table 5 are based on the current regulatory legal acts of the Republic of Armenia. According to these documents, the value added tax and income tax is 20 %[7], and the property tax is 0.6 % (of the residual value). Based on the data on the construction and current operating expenses of the SHPP, Table 6 shows the key indicators of financial productivity.

[7] Hayastani Hanrapetut'yan Harkayin orensgirk', HO-165-N, yndunvats 2016 t'vakani hoktemberi 4-in (In Armenian).

Table 6

Financial performance indicators

Indicator	Unit rev.	Value
Internal rate of return	%	10.4
Payback period	years	9.0

Discussion and Conclusions. Due to the mountainous terrain in the greater territory of the Republic of Armenia, local resistance is often created to adjust the pressure in the water supply network. As a rule, we are talking about semi-open valves and the installation of pressure control equipment. Equipping the network nodes with specially designed turbines will enable converting artificially created local resistance and extinguished mechanical energy into electrical energy. It should be noted that more than 300 semi-open valves and pressure control equipment were installed in the Yerevan water supply system alone. Many of them require replacement. The solutions proposed in this article can be applied to the areas under repair.

References

1. Karl-Ulrich Rudolph. The German Water Sector. Policies and Experiences. Berlin – Bonn – Witten: Federal Ministry for the Environment, Nature Conservation and Nuclear Safety. Federal Environmental Agency; 2001. P. 151.

2. Cabrera E, Pardo MA, Cobacho R, et al. Energy audit of water networks. Journal of Water Resources Planning and Management. 2010;136:669–677. https://doi.org/10.1061/(ASCE)WR.1943-5452.0000077

3. Ramos JS, Ramos HM. Sustainable application of renewable sources in water pumping systems: Optimized energy system configuration. Energy Policy. 2009;37:633–643. https://doi.org/10.1016/j.enpol.2008.10.006

4. Galperin EM, Poluyan VI, Chuvilin VN. Reliability of water supply and water disposal systems. VST. 2006;9:38−42.

5. Davidov AB, Buligin VI, Radetskiy MYu. Guarantee of water supply system reliability. VST. 2004;3:6−8.

6. Fontana N, Giugni M, Portolano D. Losses reduction and energy production in water-distribution networks. Journal of Water Resources Planning and Management. 2012;138:237–244.

7. Vieira F, Ramos HM. Hybrid solution and pump-storage optimization in water supply system efficiency: A case study. Energy Policy. 2008;36:4142–4148. https://doi.org/10.1016/j.enpol.2008.07.040

8. Bogomolov AI, Mikhailov KA. Gidravlika. Moscow: Stroiizdat; 1972. 648 p. (In Russ.)

9. Lovkis ZV. Gidravlika. Minsk: Belarusskaya navuka; 2012. 439 p. (In Russ.)

10. Landau L, SirenkoYu. (eds.) Gidroehnergetika i okruzhayushchaya sreda. Kiev: Libra; 2004. 484 p. (In Russ.)

11. Frijns J, Middleton R, Uijterlinde C, et al. Energy efficiency in the European water industry: learning from best practices. Journal of Water and Climate Change. 2012;3:11–17. https://doi.org/10.2166/wcc.2012.068

12. Vikulin PD, Vikulina VB. Gidravlika sistem vodosnabzheniya i vodootvedeniya. Moscow: MGSU; 2014. 248 p. (In Russ.)

Received 04.05.2022

Revised 28.05.2022

Accepted 07.06.2022

About the Authors:

Sahakyan, Aram Ashot, Head of the Faculty of Construction, National University of Architecture and Construction of Armenia (105, Teryan St., Yerevan, 0009, Republic of Armenia), Cand.Sci. (Eng.), ORCID, sahakyan.aram@nuaca.am

Butko, Denis A., Head of the Water Supply and Sewerage Systems Department, Don State Technical University (1, Gagarin sq., Rostov-on-Don, 344000, RF), Cand.Sci. (Eng.), associate professor, ScopusID, ORCID, den_111@mail.ru

Claimed contributorship:

A. A. Sahakyan: basic concept formulation; research objectives and tasks; computational analysis; text preparation; formulation of conclusions. D. A. Butko: analysis of the research results; the text revision; correction of the conclusions.

Conflict of interest statement

The authors do not have any conflict of interest.

All authors have read and approved the final manuscript.

MACHINE BUILDING AND MACHINE SCIENCE

UDC 621.375. (075.8)
https://doi.org/10.23947/2687-1653-2022-22-2-150-160

Original article

Investigation of ACS Image Stabilization of On-board Optoelectronic Guidance and Tracking Devices

K. A. Burdinov ✉, **K. M. Shashkina**, **Ehsan Shaghaei**
Centre for Robotics and Mechatronics Components, Innopolis University, 1, Universitetskaya St., Innopolis, Russian Federation
✉sainquake@gmail.com

Abstract

Introduction. The movement of the carrier and external factors (the effects of the atmosphere, temperature and pressure) degrade significantly the image quality of the servo optoelectronic systems (OES) and the positioning accuracy of the emitting OES. The issues of image quality improvement and the probability of keeping the image of the observation object (OO) on the optical axis of the servo EOS are considered.

Materials and Methods. The development of an automatic control system for an optoelectronic device (ACS OED) involved solving a multi-criteria optimization problem taking into account a number of conflicting technical-and-economic (TE) requirements. The determination of tolerated dynamic errors (TDE) of image stabilization was a key issue in the development of on-board optoelectronic devices (OOED). Lagrange equations of the second kind and the mixed Gilbert method made it possible to obtain a mathematical model of the CO OED. Then, the decomposition of a two-link ACS with nonlinear cross-couplings in the CO was performed. A functional diagram of the image formation model of the OOED was presented. The parameters of the matrix photodetector and the requirements for the dynamic error of the ACS OED, taking into account the permissible MTF of the OED, were listed. The functions of transferring modulation, as well as linear, harmonic and vibrational shift of the image corresponding to the permissible and achieved TDE were visualized. Logarithmic frequency characteristics were created in the Mathcad environment. The two-link control system of the OED with the specified parameters of the CO for the considered movement was presented as two independent azimuth and elevation control channels.

Results. The processes of control of the on-board optoelectronic system in the stabilization and tracking modes were described. To study the dynamics of spatial control of the OOEP in accordance with the ACS methodology, a computer simulation model (CSM) of the digital automatic control systems (DACS) of the OED was developed. It was implemented in the Matlab environment and consisted of CSM CO, drives, proportional-integral-derivative (PID) controllers taking into account non-linearities, a central computing device (CCD), a guidance software device, a CSM-carrier that implemented the equations of motion. Harmonic vibrations of the carrier were described. The errors of tracking and stabilization in the tracking mode with an additional control action introduced in the form of a constant speed were determined. The dynamics of spatial control of the OOED was investigated. A computer simulation model of a digital automatic control system of an optoelectronic device, the results of modeling the DACS OED without considering the board movement, and the processes of OED control subject to movement were visualized.

Discussion and Conclusions. The stabilization accuracy was calculated for the studied cases. It was established that the stabilization tens of times exceeded the previously stated indicators, and it tens of times reduced the requirements for the convergence of the laser beam and the laser radiation power when developing the optical path of the product in question. The proposed CSM can be used in the development of the on-board optoelectronic systems. In this case, the application of the presented methodology and CSM will help to reduce labor costs and minimize errors.

Keywords: automatic control system, modulation-transfer function, servo system, optimization, optoelectronic device.

Acknowledgements: the authors would like to thank the management of the NTI Competence Center program “Technologies in Robotics and Mechatronics Components” for their assistance in preparing this article.

For citation: K. A. Burdinov, K. M. Shashkina, Ehsan Shaghaei. Investigation of ACS image stabilization of on-board optoelectronic guidance and tracking devices. Advanced Engineering Research, 2022, vol. 22, no. 2, pp. 150–160. https://doi.org/10.23947/2687-1653-2022-22-2-150-160

Introduction. When designing modern on-board optoelectronic devices (OED) and complexes, methods of computer modeling of optoelectronic systems (OES) are widely used. Such authors as Yu. G. Yakushenkov, V. V. Tarasov, I. P. Torshina, V. P. Ivanov, V. A. Baloev, V. A. Ovsyannikov, V. L. Filippov, worked on these tasks. Computer modeling enables to solve the problems of rational choice of the structure, parameters, and element base of the OES, providing the required performance indicators under specified constraints without expensive field studies and tests.

The movement of the carrier and external factors (temperature, pressure) degrade significantly the image quality of the servo OES and the positioning accuracy of the emitting OES. The probability of holding the image of the object of observation (OO) on the optical axis of the tracking OES is reduced. For emitting OES, the positioning accuracy and the probability of performing observation tasks are reduced. To hold the image in vision or in the irradiation sector, it is required to capture a fairly large solid viewing angle. Hence, it is required to increase the dimensions of optical systems and power electronics capacities. To avoid this, controlled radiating OES is used. The above-mentioned features of the OED limit the development of the ACS OED. This problem was considered by V. A. Strezhnev, V. M. Matrosov, A. S. Zemlyakov, N. N. Malivanov, E. I. Somov, A. I. Malikov, V. A. Krenev, A. I. Karpov, D. A. Molin, A. V. Mikhalitsyn. When designing controlled OED operating in guidance and tracking modes, the following fact was established: the guidance time and the accuracy of stabilization of the optical axis, as well as the dynamics of the OED subsystems affect significantly the image quality.

Thus, the task of minimizing the time and increasing the accuracy of pointing and holding the image of the OO in vision of the controlled OED is a challenge. In this regard, the following is required:

− development of mathematical models of power lines as control objects;

− synthesis of control algorithms;

− creation of computer simulation models (CSM);

− study on control systems that take into account the dynamics of the movement of a controlled OED;

− determination of parameters affecting the dynamic properties and image quality.

The work aimed at improving the accuracy characteristics and image quality of OED operating in the guidance, stabilization and tracking modes, due to the rational choice of their parameters during synthesis and modeling.

Materials and Methods. The development of ACS OED started with solving a multi-criteria optimization problem that took into account conflicting technical-and-economic (TE) requirements. In the development of study [1], a modified method of designing a self-propelled ACS OED was proposed. For the quality criterion of the ACS, we took a set of dynamic characteristics of control channels that met the conditions:

$$T_{\text{оэп}}(\nu_{\text{н}}) \geq T_{\text{оэп}}^{\text{доп}}(\nu_{\text{н}}), \delta(\omega) \leq \delta^{\text{доп}}(\omega), \Delta\alpha_{\text{к}} \leq \Delta\alpha_{\text{к}}^{\text{доп}}, \Delta\dot{\alpha}_{\text{к}} \leq \Delta\dot{\alpha}_{\text{к}}^{\text{доп}},$$
$$M \leq M^{\text{доп}}, |\Delta\varphi| \geq \Delta\varphi^{\text{доп}}, |\Delta L| \geq \Delta L^{\text{доп}}. \quad (1)$$

Here, $T_{\text{оэп}}^{\text{доп}}(\nu_{\text{н}}), T_{\text{оэп}}(\nu_{\text{н}})$ — permissible and implemented modulation-transfer function (MTF) of the OED at the Nyquist frequency, $\delta(\omega)$; $\delta^{\text{доп}}$ — amplitude frequency response of cross-couplings and its acceptable decomposition value; $\Delta\alpha_{\text{к}}^{\text{доп}}, \Delta\dot{\alpha}_{\text{к}}^{\text{доп}}, \Delta\alpha_{\text{к}}, \Delta\dot{\alpha}_{\text{к}}$ — permissible and steady-state values of the dynamic errors of the ACS in angle and angular velocity under the action of disturbances under conditions close to the actual operation of the ACS; $\text{к} = 1, 2, \ldots$ — number of the control channel providing image quality; $M_{\text{доп}} = 1.05$–1.25 — oscillation index, $\Delta\varphi$; ΔL — stability margins in phase and amplitude.

The key issue in the development of the OED is the determination of tolerated dynamic errors (TDE) of image stabilization.

The image formation scheme of the on-board optoelectronic device (OOED) is shown in Figure 1.

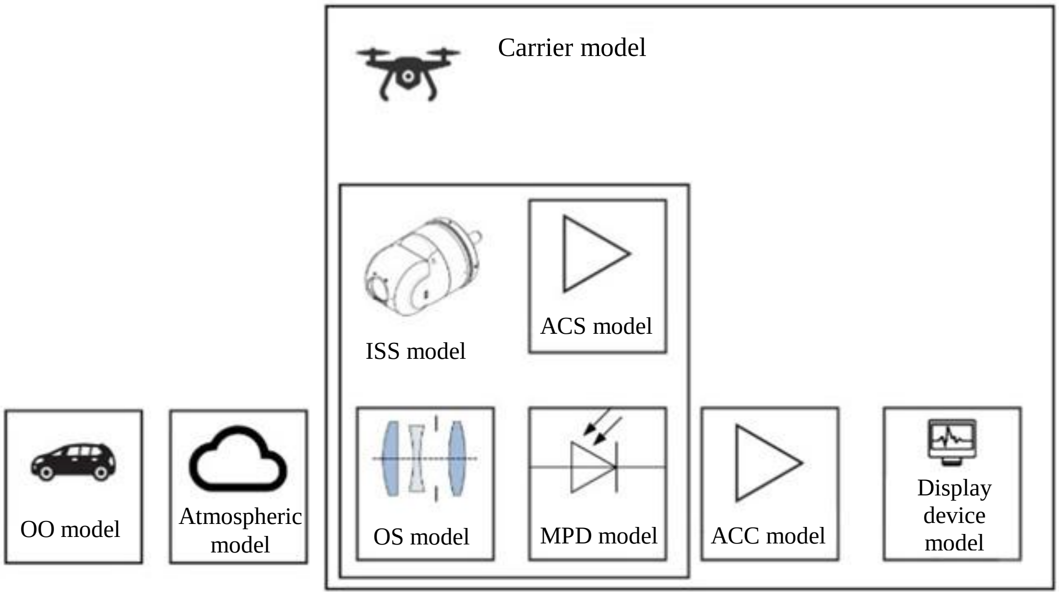

Fig. 1. Functional diagram of the OOED imaging model: OO — object of observation; OS — optical system; MPD — matrix photodetector; ACD — amplifying-converting device; ISS — image stabilization system

The MTF OOED should meet the condition that provides acceptable image quality [2]:

$$T_{\text{ОЭС}}(\nu) = T_{\text{ат}}(\nu)T_{\text{об}}(\nu)T_{\text{фп}}(\nu)T_{\text{упу}}(\nu)T_{\text{ССИ}}(\nu) > T_{\text{ОЭС}}^{\text{доп}}(\nu), \tag{2}$$

$$T_{\text{ОЭС}}^{\text{доп}}(\nu) = 2\left(Sinc\left(N\frac{\gamma_{\text{и}}}{2}\right)\right)^{-1} exp\left[-\frac{\left(N\gamma_{\text{р}}\right)^2}{16\,ln(2m)}\right].$$

Here, $T_{\text{ОЭС}}(\nu)$ — MTF OED; N — spatial frequency; $T_{\text{ОЭС}}^{\text{доп}}(\nu)$ — admissible MTF OOED; $T_{\text{ат}}(\nu)$ — atmospheric MTF; $T_{\text{об}}(\nu)$ — lens MTF; $T_{\text{фп}}(\nu)$ —photodetector MTF; $T_{\text{упу}}(\nu)$ — optical information conversion function MTF [1]; $T_{\text{ССИ}}(\nu)$ — MTF of the image shift (dynamic error of the ISS), depending on the type of dynamic displacement of the image: linear (Л) — $x(t) = Vt$, harmonic (Г) — $x(t) = a_0 sin(t)$, random (R), and defocusing.

The permissible MTF of the image stabilization system includes tracking, stabilization, vibration protection (VPS) and automatic focusing (AFS) systems [3]:

$$T_{\text{ССИ}}(N) = T_{\text{Л}}(N)T_{\Gamma}(N)T_{\text{В}}(N)T_{\Phi}(N) \geq T_{\text{ССИ}}^{\text{доп}}(N) = \frac{T_{\text{оэп}}^{\text{доп}}(N)}{T_{\text{ст}}(\text{N})},$$

$$T_{\text{Л}}(\nu) = sinc(\pi\Delta\alpha_{\text{Л}}\nu), T_{\Gamma}(\nu) = J_0(2\pi\Delta\alpha_{0\Gamma}\nu), T_{\text{В}}(\nu) = exp[-2(\pi\Delta\alpha_{\text{В}}\nu)^2], \tag{3}$$

$$T_{\Phi}(\nu) = \frac{2J_1(\Delta_{\text{ф}})}{\Delta_{\text{ф}}}, \Delta_{\text{ф}} = 28\pi\sigma\left(\frac{\lambda_{\text{ср}}\nu}{D}\right)\left(1 - \frac{\lambda_{\text{ср}}\nu}{D}\right),$$

$$T_{\text{ст}}(N) = T_{\text{ат}}(N)T_{\text{об}}(N)T_{\text{фп}}(N)T_{\text{упу}}(N).$$

Here, $T_{\text{Л}}(N)$ — image linear shift error; $T_{\Gamma}(N)$ — sinusoidal error amplitude; $T_{\text{В}}(N)$ — average value of vibration amplitude error; J_0 — zero-order Bessel function of the first kind; $J_1(\Delta_{\text{ф}})$ — Bessel function of the first kind of the first order; $\Delta_{\text{ф}}$ — focus error (mm); σ — average value of wave aberration in fractions of a wavelength; $\lambda_{\text{ср}}$ — average wavelength of the spectral range.

Let us assume that each subsystem of the ACS must make the same amount of change in the image quality of the OED and $T_{\text{ст}}(N)$ = const during observation. Then, the definition of acceptable MTF R, VPS, AFS, will be simplified (3):

$$T_j^{\text{доп}}(\nu) = \sqrt[4]{\frac{T_{\text{ОЭС}}^{\text{доп}}(\nu)}{T_{\text{ст}}(\nu)}} \quad (j = \text{Л}, \Gamma, \text{В}, \Phi). \tag{4}$$

We expand functions $T_{\text{Л}}(N), T_{\Gamma}(N), T_B(N), T_{\Phi}(N)$ (3) into a series and obtain expressions that determine the TDE:

$$\Delta\alpha_{Л}^{доп} \le \frac{0{,}824\sqrt{1-T_{Л}^{доп}(\nu_{н})}}{\nu_{н}}, \Delta\alpha_{Г}^{доп} \le= \frac{0{,}335\sqrt{1-T_{Г}^{доп}(\nu_{н})}}{\nu_{н}}, \quad (5)$$
$$\Delta_{Ф}^{доп} \le 3{,}018\sqrt{1-T_{Ф}^{доп}(\nu_{н})}, \Delta\alpha_{В}^{доп} \le \frac{\sqrt{0.5\,ln[T_{В}^{доп}(\nu_{н})]^{-1}}}{\pi\nu_{н}}.$$

Here, $\nu_{н}$ — Nyquist frequency.

The limiting spatial frequency that the OED should resolve during the observation process is determined by the Johnson criterion:

$$\nu_{пр} = \frac{N_{Д}L}{h_{кр}}, \nu_{н} = 0{,}5\nu_{пр}, \quad (6)$$

where $\nu_{пр}$ — angular (bar/rad) limiting spatial frequency; $N_{Д}$ — number of resolution elements (Johnson numbers); L — distance to OO; $h_{кр}$ — critical size of OO.

When decomposing, all members of the series are discarded, except the first ones, therefore, the tolerances obtained should be revised by gradient descent.

The above reasoning allowed us to determine the accuracy of image stabilization of the onboard optoelectronic system (OOES) for tracking and stabilization modes. A methodology and a program for calculating MTF and tolerances were developed (Patent RU2021660340[1]).

Let us denote requirements for the dynamic error of the ACS OED, taking into account the permissible MTF OED. Initial data for calculation:

− diameter of the entrance pupil — D = 90 mm,
− OS focal length — f`= 100 mm,
− wavelength — λ = 4 μm,
− distance to the object of observation — L = 10 km,
− meteorological visibility — SM = 15 km,
− flight altitude — H = 5 km,
− number of MPD elements — 256×256,
− frame rate — F = 400 Hz,
− probability of correct detection — $P_{обн}$ = 0.8,
− false alarm probability — $P_{лт} = 10^{-4}$,
− signal-to-noise ratio of the amplifier — optimal filter — m = 1.105,
− angular size of the object of observation — $\gamma_s = 5\cdot10^{-5}$ rad,
− angular distance between two adjacent targets — $\gamma_{р} = 3.34\cdot10^{-3}$ rad.

MPD parameters:

− d = 0. 0.25a — thickness of the photosensitive layer,
− $\varepsilon_n = 4\cdot10^{-5}$ — charge transfer inefficiency,
− α_c = 2 — number of samples per 1 element,
− $k_з$ = 0.6 — fill factor,
− $\tau = 5.4\cdot10^{-9}$ s — reading time,
− $\tau_{пр} = 5\cdot10^{-10}$s — time constant of the transducer.

Figure 2 shows the MTF of linear, harmonic and vibrational shift of the image corresponding to the permissible and obtained DDP of the ACS OOED.

[1] Program for calculating the modulation transfer function of an optoelectronic device based on UAV: RF patent 2021660340, 2021. Innopolis University. (In Russ.)

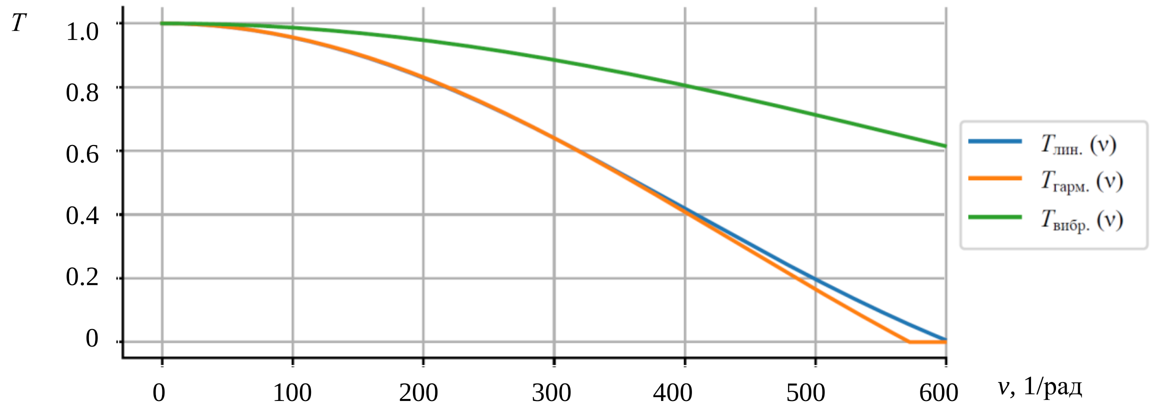

Fig. 2. Modulation transfer functions $T_j^{\text{доп}}(\nu)$

In accordance with (3)–(5) and the initial data for the calculation, we determined: $\nu_{\text{пр}} = 600$ rad^{-1} of the OOED observation channel in the infrared region with a detection probability of $P = 0.8$. For MTF OOED and TDE ACS: $\Delta\alpha_{\text{Л}} = 3.5$ ang. min, $\Delta\alpha_{\Gamma} = 3.1$ ang. min, $\Delta\alpha_{\text{В}} = 3.0$ ang. min.

On the basis of the Lagrange equations of the second kind and the mixed Gilbert method, a mathematical model of the SO OED [4] of guidance and tracking was obtained in the form of three information channels driven by DBM electric motors along the gimbal axles. We presented it in a matrix form[2]:

$$A(q)\ddot{q} + B(t,q)\dot{q} + F(q,\dot{q}) + W(t,q) + Q(t,q) = M_{\text{дв}} - M_{\text{тр}}. \tag{7}$$

Here, $q = (\alpha \quad \beta)^T$, α, β — CO rotation angles in azimuth and elevation..

$$A(q) = \begin{pmatrix} B_1 + B(\beta) & -D(\beta) \\ -D(\beta) & C_2 \end{pmatrix},\ B(t,q) = \begin{pmatrix} 0 & b_{\alpha\beta}(t,\alpha,\beta) \\ -b_{\alpha\beta}(t,\alpha,\beta) & 0 \end{pmatrix},$$

$$F(q,\dot{q}) = \begin{pmatrix} -2\dot{\alpha}\dot{\beta}F(\alpha,\beta) - \dot{\beta}^2 E(\beta) \\ \dot{\alpha}^2 F(\beta) \end{pmatrix},\ W(t,q) = \begin{pmatrix} w_\alpha(t,q) \\ w_\beta(t,q) \end{pmatrix},$$

$$Q(t,q) = \begin{pmatrix} r_\alpha(q) \\ r_\beta(q) \end{pmatrix}\left(\tilde{a}_O(t) + A_y A_c \tilde{g}\right),\ M_{\text{дв}} = \begin{pmatrix} M_{\text{дв.1}} \\ M_{\text{дв.2}} \end{pmatrix},\ M_{\text{тр}} = \begin{pmatrix} M_{\text{тр.1}} sign(\dot{\alpha}) \\ M_{\text{тр.2}} sign(\dot{\beta}) \end{pmatrix},$$

$$b_{\alpha\beta}(t,\alpha,\beta) = \{(2A_2(\beta) - C_2)\cos\alpha - 2E(\beta)\sin\alpha\}\omega_{x_y}(t) - 2F(\beta)\omega_{y_y}(t) - \{(2A_2(\beta) - C_2)\sin\alpha + 2E(\beta)\cos\alpha\}\omega_{z_y}(t),$$

$$w_\alpha(t,q) = \left\{-\dot{\omega}_{x_y}(t)F(\alpha,\beta) + \dot{\omega}_{y_y}(t)\left(B_1 + B(\beta)\right) - \dot{\omega}_{z_y}(t)D(\alpha,\beta)\right\} + \left\{E(\alpha,\beta)\Omega^2_{x_y}(t) - E(\alpha,\beta)\omega^2_{z_y}(t) + D(\alpha,\beta)\omega(t)\omega_{y_y}(t) + 2A_1(\alpha,\beta)\omega_{x_y}(t)\omega_{z_y}(t) - F(\alpha,\beta)\omega_{y_y}(t)\omega_{z_y}(t)\right\},$$

$$w_\beta(t,q) = \left\{-\dot{\omega}_{x_y}(t)[E(\beta)\cos(\alpha) - C_2\sin(\alpha)] - \dot{\omega}_{y_y}(t)D(\beta) + \dot{\omega}_{z_y}(t)[E(\beta)\sin(\alpha) + C_2\cos(\alpha)]\right\} - \frac{1}{2}\left\{[F(\beta)(1+\cos(2\alpha)) + D(\beta)\sin(2\alpha)]\omega^2_{x_y}(t) - 2F(\beta)\omega^2_{y_y}(t) + [F(\beta)(1-\cos(2\alpha)) - D(\beta)\sin(2\alpha)]\omega^2_{z_y}(t) + 2[2A_2(\beta)\cos(\alpha) - E(\beta)\sin(\alpha)]\omega_{x_y}(t)\omega_{y_y}(t) - 2[F(\beta)\sin(2\alpha) - D(\beta)\cos(2\alpha)]\omega_{x_y}(t)\omega_{z_y}(t) - 2[E(\beta)\cos(\alpha) + 2A_2(\beta)\sin(\alpha)]\omega_{y_y}(t)\omega_{z_y}(t)\right\},$$

$$r_\alpha(q) = m_1\begin{pmatrix} -x_{C_1}\sin(\alpha) + z_{C_1}\cos(\alpha) \\ 0 \\ -x_{C_1}\cos(\alpha) - z_{C_1}\sin(\alpha) \end{pmatrix}^T + m_2\begin{pmatrix} -\left(x_{C_2}\cos(\beta) - y_{C_2}\sin(\beta)\right)\sin(\alpha) + z_{C_2}\cos(\alpha) \\ 0 \\ -\left(x_{C_2}\cos(\beta) - y_{C_2}\sin(\beta)\right)\cos(\alpha) - z_{C_2}\sin(\alpha) \end{pmatrix}^T,$$

[2]Burdinov KA, et al. Matematicheskaya model' i sintez sistemy avtomaticheskogo upravleniya bortovogo optiko-ehlektronnogo pribora. In: Proc. XII All-Russian Congress on Fundamental Problems of Theoretical and Applied Mechanics, Ufa, 2019. P. 190–192. (In Russ.)

$$r_{\beta}(q) = m_2 \begin{pmatrix} \left(-x_{C_2}\, sin(\beta) - y_{C_2}\, cos(\beta)\right) cos(\alpha) \\ x_{C_2}\, cos(\beta) - y_{C_2}\, sin(\beta) \\ \left(x_{C_2}\, sin(\beta) + y_{C_2}\, cos(\beta)\right) sin(\alpha) \end{pmatrix}^T .$$

The next stage of development was the decomposition of doubly connected ACS [5] with nonlinear cross couplings in the CO, which is the studied OED. The linearized equations of motion with respect to the trajectory have the form:

$$a \times_{\text{вх}} (t) = \dot{\alpha}_0 t \in 0 \div 2\pi;\ \beta \times_{\text{вх}} (t), = \dot{\beta}_0 t \in 0 \div \pi/2,$$

$$\begin{aligned} &(a_{10} + a_{11})\Delta\ddot{\alpha} + (b_{10} + b_{11})\Delta\dot{\alpha} + c_{11}\Delta\alpha + a_{12}\Delta\ddot{\beta} + b_{12}\Delta\dot{\beta} + c_{12}\Delta\beta = K_{u1}\Delta u_1, \\ &a_{21}\Delta\ddot{\alpha} + b_{21}\Delta\dot{\alpha} + a_{20}\Delta\ddot{\beta} + b_{20}\Delta\dot{\beta} + c_{22}\Delta\beta = K_{u2}\Delta u_2, \\ &\Delta u_1 = R_1(p)\Delta\varepsilon_1, \Delta\varepsilon_1 = \Delta\alpha^*_{\text{вх}} - \Delta\alpha^*; \Delta u_2 = R_2(p)\Delta\varepsilon_2, \Delta\varepsilon_2 = \Delta\beta^*_{\text{вх}} - \Delta\beta^*. \end{aligned} \quad (8)$$

Having constructed the variable coefficients of system (8), we determine their values at $t = t_к^*$ at “dangerous” points at which the parameters change significantly or change signs in the range of angles ($\beta^* = 0 \div \pi/2$, $\alpha^* = 0 \div 2\pi$). Then, reducing system (8) (for $t = t_к^*$) to a system with constant parameters and using Cramer's rule, we express it in the form of transfer functions (TF) at points $t = t_к^*$:

$$\begin{aligned} \Delta\alpha &= W_{11}(p, t^*_к)\Delta u_1 - W_{12}(p, t^*_к)\Delta u_2, \\ \Delta\beta &= W_{22}(p, t^*_к)\Delta u_2 - W_{21}(p, t^*_к)\Delta u_1. \end{aligned} \quad (9)$$

The obtained TF (9) taking into account (8) for each selected moment of time ($t = t_к^*$) can be presented in the form of a block diagram with direct cross couplings (CC, Fig. 3). From now on, for simplicity of writing, we denote TF as $W_{кij}(p) = W_{ij}(p, t_к^*)$.

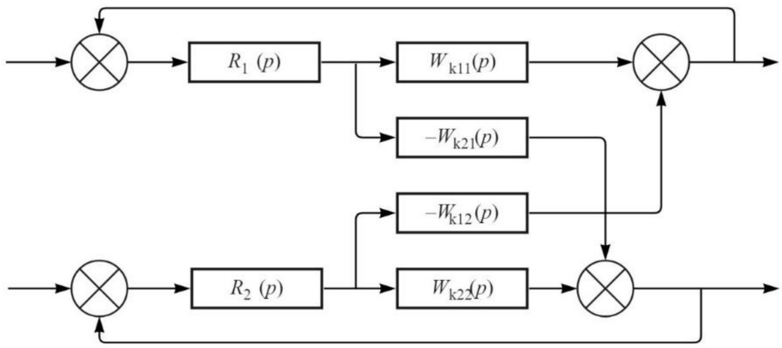

Fig. 3. Structural diagram of doubly connected ACS

We evaluate the CC ACS by their frequency response (FR). For this purpose, we write down the TF of the open system, taking into account the 2nd closed control channel when $\Delta\beta_{вх} = 0$ (Fig. 4).

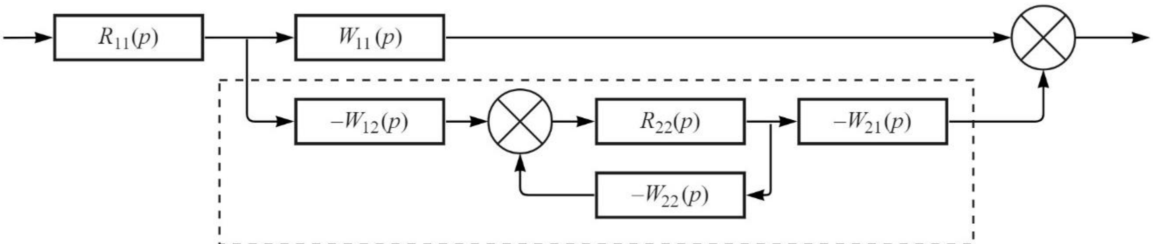

Fig. 4. Structural diagram of ACS, open on one control channel

Let us build hodograph $W_{к1}^{раз}(j\omega) = R_1(j\omega)W_{к11}(j\omega)$ and tubes around it with radii for each moment of time $t_к^*$:

$$\varepsilon_{1к}(\omega) = R_1(\omega)\, W_{к11}(\omega)\, W_{2к}(\omega)\, \delta_к(\omega). \quad (10)$$

Taking into account (10) and the Nyquist criterion, it is possible to judge the stability of the ACS (1), (2) and the influence of the CC on its stability in the range of scanning angles (3).

As a result, for each ($t_к^*$-th), we determine the CC time:

$$\delta_{\text{к}i}(\omega) = \delta_{\text{к}12}(\omega)\delta_{\text{к}21}(\omega)W_{\text{к}j}(\omega) = \frac{W_{\text{к}12}(\omega)}{W_{\text{к}11}(\omega)}\frac{W_{\text{к}21}(\omega)}{W_{\text{к}22}(\omega)}W_{\text{к}j}(\omega), (i, j = 1,2). \quad (11)$$

Let us consider the CC ACS that satisfy the decomposition conditions.

According to (8), (11), from the CO mass geometry data, for 11 selected points in time, we determined ($t_{\text{к}}^{*}$ = 0; 0.89; 1.35; 1.58; 1.71; 2.3; 2.97; 3.8; 4.5; 4.75; 6.28 s). We built $a_{ij}(t)$, $b_{ij}(t)$, $c_{ij}(t)$. Logarithmic frequency response (LFR) $\delta_{\text{к}}(\omega)$ (k = 1.11) was created in the Mathcad environment (Fig. 5).

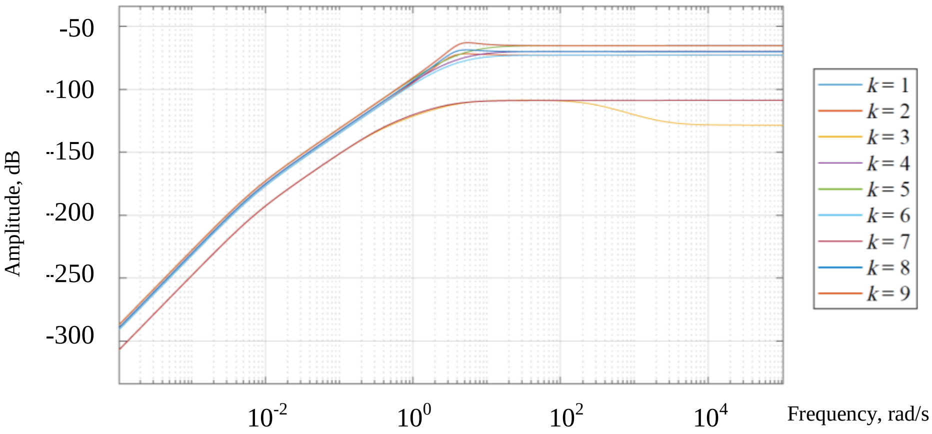

Fig. 5. Logarithmic frequency response $\delta_{\text{к}}(\omega)$

Figure 5 shows that the entire LFR set does not exceed –50 dB. From the analysis of LFR $\delta_{\text{к}}(\omega)$, we have the results presented below.

$\forall\omega\in\Omega_1 = (10^{-4}\div10^{4})$ rad/s.

The following was determined: max $\delta_{\text{к}}(\omega)$ = 0.0136 (–37.3 dB) < $\delta^{\text{доп}}$ = 0.0335 (–29.5 dB), $\Delta L = M^{\text{доп}} / (M^{\text{доп}} + 1)$ = 0.535 (–5.43 dB) at $M_{10} = M_{20}$ = 1.1; $M^{\text{доп}}$ = 1.15.

Hence, a doubly connected control system (8) of the OED with the given parameters of the CO for the motion in question can be presented as two independent control channels in azimuth and elevation angle.

Research Results. Figures 6 and 7 show the OOED control processes in stabilization and tracking modes. The scale of the misalignment graphs has been increased by 600 times. The graphs of the program control and the output values visually coincide.

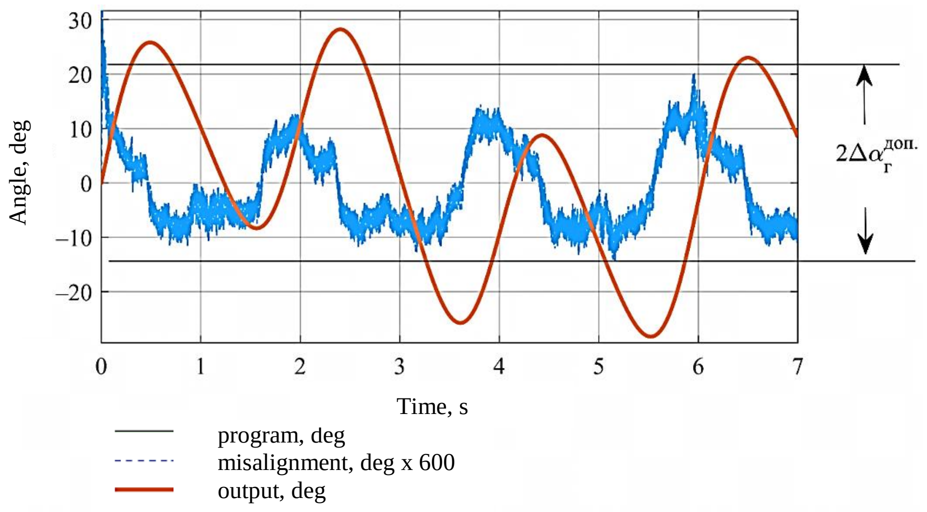

Fig. 6. OOED stabilization processes in azimuth

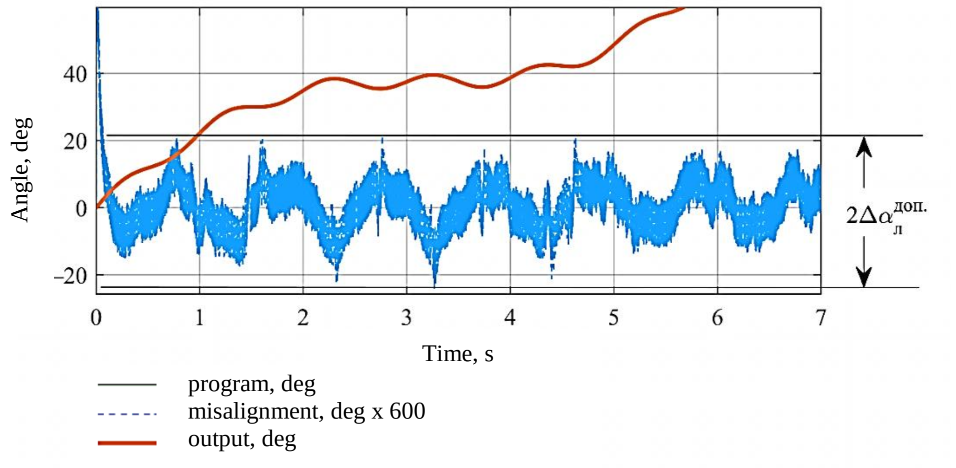

Fig. 7. OOED tracking processes in azimuth

We describe the harmonic oscillations of the carrier: $A_1 = A_2 = 2^0$ (amplitudes), $T_1 = T_2 = 1$ s (oscillation periods), and $A_1 = A_2 = 12^0$, $T_1 = T_2 = 6.28$ s. We indicate the load moments: $M_{дв1} = 2.2$ Nm, $M_{дв1} = 0.3$ Nm. With such harmonic oscillations and load moments, the error of stabilization of the sighting axis does not exceed:

− in azimuth — 1.2 ang. min,

− in elevation angle — 1.6 ang. min.

In tracking mode, with an additional control action introduced in the form of a constant speed of 12 ^{deg}/s, the error of tracking and stabilization does not exceed 1.7 ang. min in azimuth and 1.3 ang. min in elevation angle.

To study the dynamics of the spatial control of the OOED in accordance with the ACS technique, the CSM of the digital automatic control system (DACS) of a specific OED was developed (Fig. 8) [1].

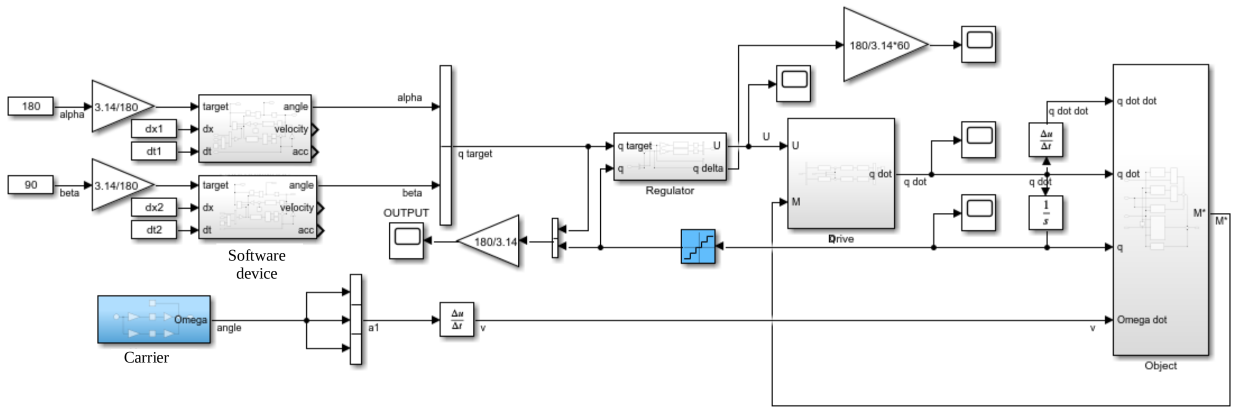

Fig. 8. Computer simulation model of a digital system for automatic control of an optoelectronic device

The solution is implemented in the Matlab Simulink environment. Its elements:

− CSM CO (Object) obtained according to (7);

− CSM of drives (Drive);

− CSM of PID-regulators (Regulator) taking into account non-linearities and DCD;

− CSM of software guidance device;

− Carrier CSM that implements the equations of carrier motion.

Figures 6 and 7 show the results of modeling the DACS OED without taking into account the movement of the board. In this case:

− guidance error does not exceed 18 ang. min in azimuth, 10 ang. min in elevation angle;

− tracking error — 0.6 ang. min in azimuth, 0.6 ang. min in elevation angle;

− stabilization error — 0.45 ang. min in azimuth, 0.6 ang. min in elevation angle.

Figure 9 shows the control processes of the OED, taking into account its movement. The azimuth guidance error is 2 ang. min, the elevation angle error is 5 ang. min. The error of tracking and stabilization is 0.8 ang. min in azimuth, 1.3 ang. min in elevation angle.

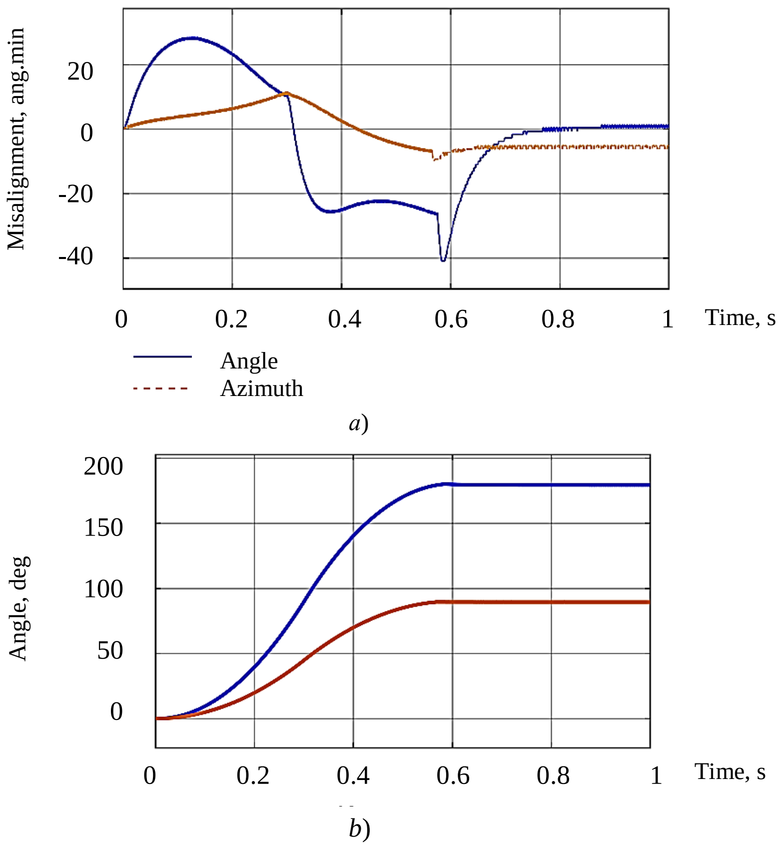

Fig. 9. Simulation results of the system in two-channel guidance mode (degrees):
a — system misalignment; *b* — transient schedules. In second case, schedules of program control (alpha target, beta target) and output value (alpha, beta) visually coincide

Discussion and Conclusions. The results obtained are presented below.

1. A technique for evaluating tolerances for the accuracy of image stabilization of the OOED under conditions of controlled and temperature influences was proposed. (Patent RU2021660340). Analytical estimates of the TDE image stabilization according to (4), (5) for tracking and stabilization modes based on the MTF OED were presented. The requirements for the ACS were obtained, providing a solution to the problem of detecting OO in the infrared region.

2. The decomposition acceptance criterion was given, the method of decomposition of a doubly connected ACS OEP with the use of computer technologies was described. The requirements for the design parameters of the CO of a real device were defined. That allowed synthesizing the ACS OEP as two independent control channels.

3. The CSM ACS OED was proposed to study the dynamics of isolated control channels and spatial control. In this case, the nonlinearity and non-stationarity of a specific CO were taken into account.

4. A mechanical model of the OED was developed, the equations of the dynamics of spatial motion (7) of the CO were obtained.

5. The parameters of the PID-controllers were synthesized, providing stable guidance and stabilization of the OED under all specified modes. Q-factor in speed: $K_{v1} = (3700 \div 4000)s^{-1}, K_{v2} = (3000 \div 3300)\ s^{-1}$. Corrective links: $T_{к11} = T_{к12} = 0.05s, T_{к21} = T_{к22} = 5 \times 10^{-5}\ s$. This provided more accurate operation of the flight planning system and trajectory construction [6–8].

6. It was shown that with the help of CSM, it was possible to obtain the required time and error of guidance, stabilization, and tracking. In this case, the guidance speed was 0.6 s. The corresponding indicator of foreign analogues — 1 s[3].

7. In [9], a laser counteraction system was considered. Its technical characteristics allowed performing the task at W = 1000 W/steradian and laser power P = 3.1 W. It was shown in [10] that the required radiation power was W = 2700 W/steradian at a laser power of P = 200 MW.

[3] Directed Infrared Countermeasure (DIRCM). EMSOPEDIA. emsopedia.org . URL: https://www.emsopedia.org/entries/directed-infrared-countermeasure-dircm/ (accessed: 01.05.2022).

We calculated the required stabilization accuracy for each of the presented cases using formula $\Delta = \frac{2\times180\times60}{\pi}\arccos\left(1-\frac{P}{2\,\pi\,W}\right)$ [ang. min] and made Table 1.

Table 1

Comparison of required stabilization accuracy

	Radiation power (W), W/sterad	Laser power (P), W	Required stabilization accuracy (Δ), ang.min
Installation [11]	2,700	0.2	33.4
Installation [10]	1,000	3.1	216.1
Product			1.3

Thus, the accuracy of stabilization of the proposed system was ten times higher than that required in papers [9, 10]. And this reduces the requirements for the convergence of the laser beam and the laser radiation power tenfold when developing the optical path of the product in question.

List of abbreviations and conventions

OES — optoelectronic system,
OED — optoelectronic device,
OO — object of observation,
CSM — computer simulation model,
ACS — automatic control system,
MTF — modulation transfer function,
TDE — tolerated dynamic error,
ISS — image stabilization system,
MPD — matrix photodetector.

References

1. Baloev VA, Burdinov KA, Karpov AI, et al. Technique for developing and testing the control and vibration-proofing systems of on-board optoelectronic devices. Journal of Optical Technology. 2021;88:24–36. https://doi.org/10.17586/1023-5086-2021-88-03-24-36

2. Molin DA. Use of the modulation transfer function for assessment of admissible characteristics of optoelectronic devices. Vestnik of KNRTU n.a. A. N. Tupolev. 2011;1:68–75.

3. Sokolskiy MN. Dopuski i kachestvo opticheskogo izobrazheniya. Leningrad: Mashinostroenie; 1989. 220 p. (In Russ.)

4. Baloev VA, Karpov AI, Krenev VA, et al. Imitatsionnoe modelirovanie dvukhstupenchatoi sistemy upravleniya skaniruyushchim ustroistvom bortovogo bazirovaniya. Journal of Optical Technology. 2017;84:6–14. (In Russ.)

5. Garkushenko VI. On synthesizing of multiply connected non-stationary system of control in the presence of incomplete information. Vestnik of KNRTU n.a. A. N. Tupolev. 2003;3:47–49.

6. Bangura M, Mahony R. Real-time model predictive control for quadrotors. IFAC Proceedings Volumes. 2014;47:11773–11780 https://doi.org/10.3182/20140824-6-ZA-1003.00203

7. Geesara Kulathunga, Fedorenko R, Kopylov S, et al. Real-time long range trajectory replanning for MAVs in the presence of dynamic obstacles. URL: https://ieeexplore.ieee.org/document/9162605 (accessed: 13.06.2022) https://doi.org/10.1109/ACIRS49895.2020.9162605

8. Geesara Prathap Kulathunga, Hany Hamed, Devitt D, et al. Optimization-Based Trajectory Tracking Approach for Multi-Rotor Aerial Vehicles in Unknown Environments. IEEE Robotics and Automation Letters. 2022;7:4598–4605.

9. HHPTh Bekman, JC van den Heuvel, FJM van Putten, et al. Development of a mid-infrared laser for study of infrared countermeasures techniques. URL: https://www.spiedigitallibrary.org/conference-proceedings-of-spie/5615/0000/Development-of-a-mid-infrared-laser-for-study-of-infrared/10.1117/12.578214.short?SSO=1 (accessed: 13.06.2022) https://doi.org/10.1117/12.578214

10. Toet A, Benoist KW, JNJ van Lingen, et al. Optical countermeasures against CLOS weapon systems. URL: https://www.spiedigitallibrary.org/conference-proceedings-of-spie/8898/1/Optical-countermeasures-against-CLOS-weapon-systems/10.1117/12.2028342.short (accessed: 13.06.2022) http://dx.doi.org/10.1117/12.2028342

Received 05.05.2022
Revised 01.06.2022
Accepted 03.06.2022

About the Authors:

Burdinov, Konstantin A., senior engineer, Center for Technologies in Robotics and Mechatronics Components, Innopolis University (1, Universitetskaya St., Innopolis, 420500, RF), ResearcherID, ORCID, sainquake@gmail.com

Shashkina, Kseniya M., Head of the Laboratory of Unmanned Technology Innopolis University (1, Universitetskaya St., Innopolis, 420500, RF), ScopusID, ORCID, k.shashkina@innopolis.ru

Ehsan Shaghaei, engineer, Center for Technologies in Robotics and Mechatronics Components, Innopolis University (1, Universitetskaya St., Innopolis, 420500, RF), ResearcherID, ScopusID, ORCID, e.shaghaei@innopolis.university

Claimed contributorship

K. A. Burdinov: academic advising; development of the methodology; analysis of the research results; the text revision; correction of the conclusions. Ehsan Shaghaei: computational analysis; text preparation; formulation of conclusions. K. M. Shashkina: proofreading and revision of the text.

Conflict of interest statement

The authors do not have any conflict of interest.

All authors have read and approved the final manuscript.

INFORMATION TECHNOLOGY, COMPUTER SCIENCE, AND MANAGEMENT

UDC 519.654
https://doi.org/10.23947/2687-1653-2022-22-2-161-168

Original article

Self-reference Lock-in Thermography for Detecting Defects in Metal Bridge Spans

Alexander L. Solovyev [1] ✉, **Mikhail E. Royak** [2]
[1] Siberian Transport University, 191, D. Kovalchuk St., Novosibirsk, Russian Federation
[2] Novosibirsk State Technical University, 20, Prospect K. Marksa, Novosibirsk, Russian Federation
✉ Alsolovyov1337@gmail.com

Abstract

Introduction. Incipient fatigue damage in the metal superstructures of bridges creates certain threats to the safety of operation. Various methods of non-destructive testing are used for their timely detection and diagnosis. A modern and popular on-the-day solution is the method of infrared (IR) thermography. Due to the specifics of the operation of IR cameras, additional processing of recordings received from these cameras is required to obtain an accurate result. This work aims at presenting a method for processing thermofilms and describing the possibilities of its application under real conditions.

Materials and Methods. A method for processing thermographic films was described. It provided detecting temperature anomalies using only information from the camera. The results of its application on the elements of existing metal bridge spans are presented.

Results. It is shown that there are temperature anomalies for existing defects. This means that the defects continue to develop, which was confirmed by subsequent observations of their condition. In addition, a case of temperature anomaly in the defect-free external region was identified. This might be a sign of an incipient defect that could not be diagnosed by other methods. If the presence of this defect is confirmed during repeated examinations, it will be possible to diagnose hidden defects that have not yet come to the surface, and/or detect potentially collapsing places.

Discussion and Conclusions. The IR thermography performance as a method of non-contact non-destructive testing is shown, as well as its operability on real objects under random load.

Keywords: IR thermography, nondestructive testing, fatigue cracks, metal bridges, structural defects, IR camera.

Acknowledgements: the authors would like to thank the reviewers, whose critical assessment of the submitted materials and suggestions for their improvement contributed significantly to the quality of this article.

For citation: A. L. Solovyev, M. E. Royak. Self-reference Lock-in Thermography for Detecting Defects in Metal Bridge Spans. Advanced Engineering Research, 2022, vol. 22, no. 2, pp. 161–168. https://doi.org/10.23947/2687-1653-2022-22-2-161-168

Introduction. Fatigue cracks in the metal structures of bridges, formed under the influence of transport loads, wind loads, etc., are a serious challenge. Although these cracks in themselves only affect the durability of the structure, under certain conditions, they can give rise to the development of brittle cracks, which directly affects the safe use of structures [1].

One of the modern methods of non-destructive testing, which is gaining popularity, is IR thermography [2–12]. The method principle is based on the fact that any body that is subjected to mechanical action releases an amount of heat proportional to the intensity of the action. Therefore, when examining a section of the structure containing defects, you can immediately get information about the distribution of stresses in this section. A different temperature distribution will be an indicator of ongoing fatigue damage [13, 14].

The major challenge when working with IR cameras (thermal imagers) is to obtain results with acceptable accuracy. Due to the structural features of the detectors, the highest accuracy is achieved when using cold sensor cameras. However, the high cost of such devices is a serious obstacle to their use. The introduction of cameras using uncooled arrays of microbolometers improved the situation, as these cameras turned out to be noticeably cheaper. The disadvantage of such thermal imagers is the lower accuracy compared to cameras with cooled matrices. Therefore, to get stable results, additional processing of the obtained thermograms is required.

This work aimed at evaluating the effectiveness of self-reference lock-in thermography using a signal obtained directly from thermal imaging[1].

Materials and Methods. The IR thermography method is based on the analysis of the temperature distribution in the material. When tensile or compressive stresses are applied to a material, its temperature changes in proportion to the magnitude of these stresses in accordance with the following formula[2]:

$$\Delta T = -\frac{\alpha}{\rho \cdot C_p} T \cdot \Delta\sigma, \tag{1}$$

where α — thermal-expansion coefficient; ρ — matter density; C_p — specific heat capacity at constant pressure; T — absolute temperature, K; $\Delta\sigma$ — change in principal stresses, MPa.

When adiabatic conditions are maintained, as well as when elastic deformations develop only, the coupling (1) is linear and reversible, in which a change in temperature follows a change in stress. As soon as damage begins to form in the material, it ceases to be elastic and develops plastic deformations. The energy of a system subject to such deformations is intensively converted into thermal energy, thus making the main contribution to the thermal effect. Hence, the thermal picture becomes a reflection of the internal state of the material (the degree of destruction) and, consequently, an indicator of the stress level.

The relative amplitude of an IR signal can be determined using the least squares method[3]. Let us assume that load F, whose impact in a certain area can be measured and denoted as $f(t)$, acts on the structure. We will consider this signal as the reference one. Suppose there is also an IR video recording of this construction in the same time interval, which can be presented as a sequence of frames (a frame is a matrix of values $M \times K$ in size) in time, and we denote values (i, j) of the element of this matrix (pixel) at time t where $1 \le i \le M$, $1 \le j \le K$, as $y_{ij}(t)$. We denote the approximation function for this element as:

$$Y_{ij}(t) = a_{ij} + b_{ij} f(t), \tag{2}$$

where a_{ij} — bias; b_{ij} — coefficient of influence of the reference signal f.

[1]Sakagami T, Nishimura T, Kubo S, et al. Development of a Self-reference Lock-in Thermography for Remote Nondestructive Testing of Fatigue Crack (1st Report, Fundamental Study Using Welded Steel Samples). Transactions of the Japan Society of Mechanical Engineers. Series A. 2006;72:1860-1867. https://doi.org/10.1299/kikaia.72.1860

[2]Thomson W. (Lord Kelvin). On the dynamical theory of heat. Trans. R. Soc. Edinburgh. 1853;20:261-283.

[3] Lesniak JR, Boyce BR, Howenwater G. Thermoelastic Measurement Under Random Loading. In: Proc. SEM Spring Conf., 1998. P. 504-507.

Using function (2), we approximate signals $y_{ij}(t)$ from the thermal imaging film. Let us show how to find these coefficients for some $y_{ij}(t)$, the reasoning for the rest will be similar. We will minimize the deviation of our approximation from the signal received from the camera:

$$\Delta^2 = \sum_{n=1}^{N} \left(y_{ij}(n) - Y_{ij}(n) \right)^2 \to \min , \qquad (3)$$

where N — number of frames in the recording; n — frame number corresponding to the time. From here, b_{ij} can be found as follows:

$$b_{ij} = \frac{\begin{vmatrix} N & \sum_{n=1}^{N} y_{ij}(n) \\ \sum_{n=1}^{N} f(n) & \sum_{n=1}^{N} y_{ij}(n) f(n) \end{vmatrix}}{\begin{vmatrix} N & \sum_{n=1}^{N} f(n) \\ \sum_{n=1}^{N} f(n) & \sum_{n=1}^{N} f^2(n) \end{vmatrix}} = \frac{N \sum_{n=1}^{N} y_{ij}(n) f(n) - \sum_{n=1}^{N} f(n) \sum_{n=1}^{N} y_{ij}(n)}{N \sum_{n=1}^{N} f^2(n) - \left(\sum_{n=1}^{N} f(n) \right)^2}. \qquad (4)$$

Through repeating (3) and (4) for all (i, j), we get matrix $B = \{b_{ij}\}$ of the same size as the original shooting frame. Thus, we obtain an approximation of each signal $y_{ij}(t)$ of the IR survey in time by means of reference signal $f(t)$. The values of matrix B show the relative intensity of the temperature change in a certain area compared to the intensity of the reference signal change. Reference signal $f(t)$ may not necessarily be received from a third-party system, e.g., from a tensometer. The described approach, called self-reference lock-in thermography, can also be applied with a reference signal obtained from the same IR recording[4] [15, 16].

Research Results. The proposed algorithm was implemented in the form of Python scripts. With the help of these scripts, thermographic films recorded on the metal spans of existing automobile bridges, in whose structures fatigue cracks had been previously diagnosed, were processed. The performance of the algorithm was verified on the bench tests simulating the behavior of real structures with known information about the defect. The survey was carried out using an infrared camera with uncooled microbolometer Fluke Ti 400 having a thermal sensitivity of less than 0.05°C and a shooting frequency of 9 Hz. The recordings were made at the time of the impact of the automobile load on the bridge. As reference signals for each record, a defect-free zone of 15×15 pixels was used from the same structural element near the existing and/or proposed destruction zone. Processing results were visually presented in the form of images obtained by means of matrix B values. Each value of the matrix corresponded to one pixel in the image, the number was converted to color using the palette function defined in the matplotlib package.

Figure 1 shows a fragment of a superstructure steel beam. A crack was found at the junction of the horizontal sheet with the wall (Fig. 1 *c*). Figure 1*a* shows one of the frames of IR film of this crack. Figure 1 *b* presents the result of processing, which clearly shows a spot, indicating heating occurring in the designated area. This zone corresponds to the area around the crack tip, which indicates the continued development of the defect. This was also confirmed by repeated surveys, which established an increase in cracks of more than 30% over 4 years.

[4] Galietti U, Modugno D, Spagnolo L. A novel signal processing method for TSA applications Measurement Science and Technology. 2005;16:2251. http://dx.doi.org/10.1088/0957-0233/16/11/017

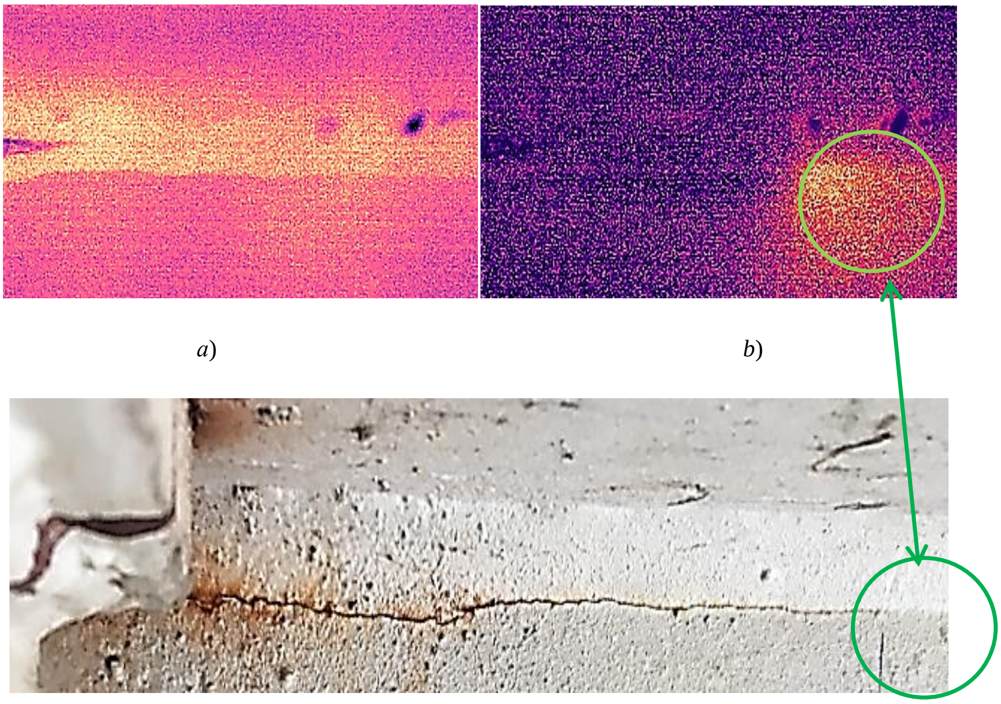

a) *b*)

c)

Fig. 1. Infrared results:
a — film frame; *b* — image built on the values of matrix *B*; *c* — photograph of the crack

Figures 2 and 3 show cracks that originated in the weld, then bifurcated and went into the stiffener and decking. The survey was carried out under the bridge tests. Strain gauges were installed in the same places to monitor the stresses, the results of which confirmed the development of these cracks.

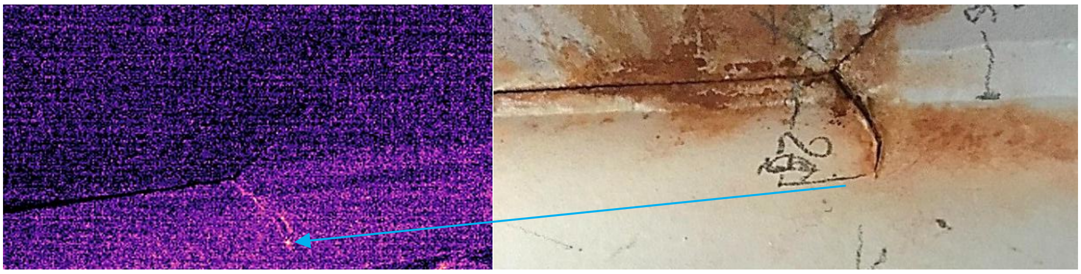

a) *b*)

Fig. 2. Diagnosed fatigue crack:
a — image built on the values of matrix *B*; *b* — photograph

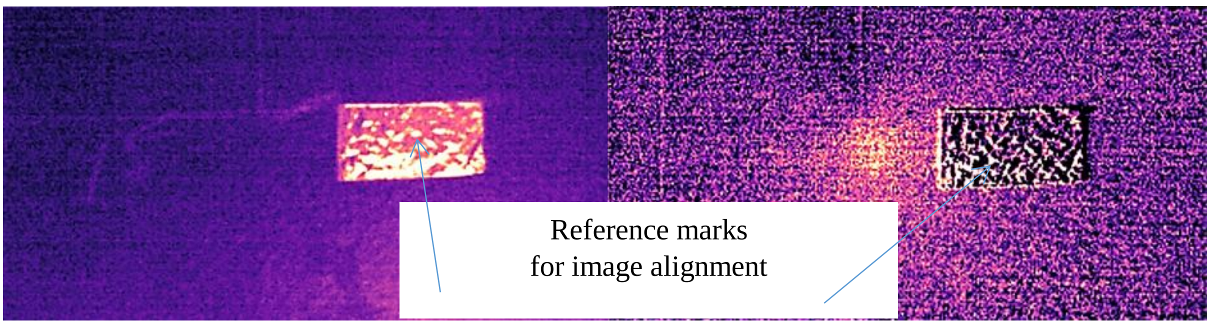

a) *b*)

c)

Fig. 3. Diagnosed fatigue crack:
a — film frame; *b* — image built on the values of matrix *B*; *c* — photograph of a crack

Figure 4 shows the combined readings of tensometers and temperature for the same section of the structure. Temperature indicators were obtained through averaging in the survey area and subsequent smoothing over time. The strain gauge data were also smoothed. As can be seen, the temperature change completely repeats the voltage change up to the sensitivity of the device.

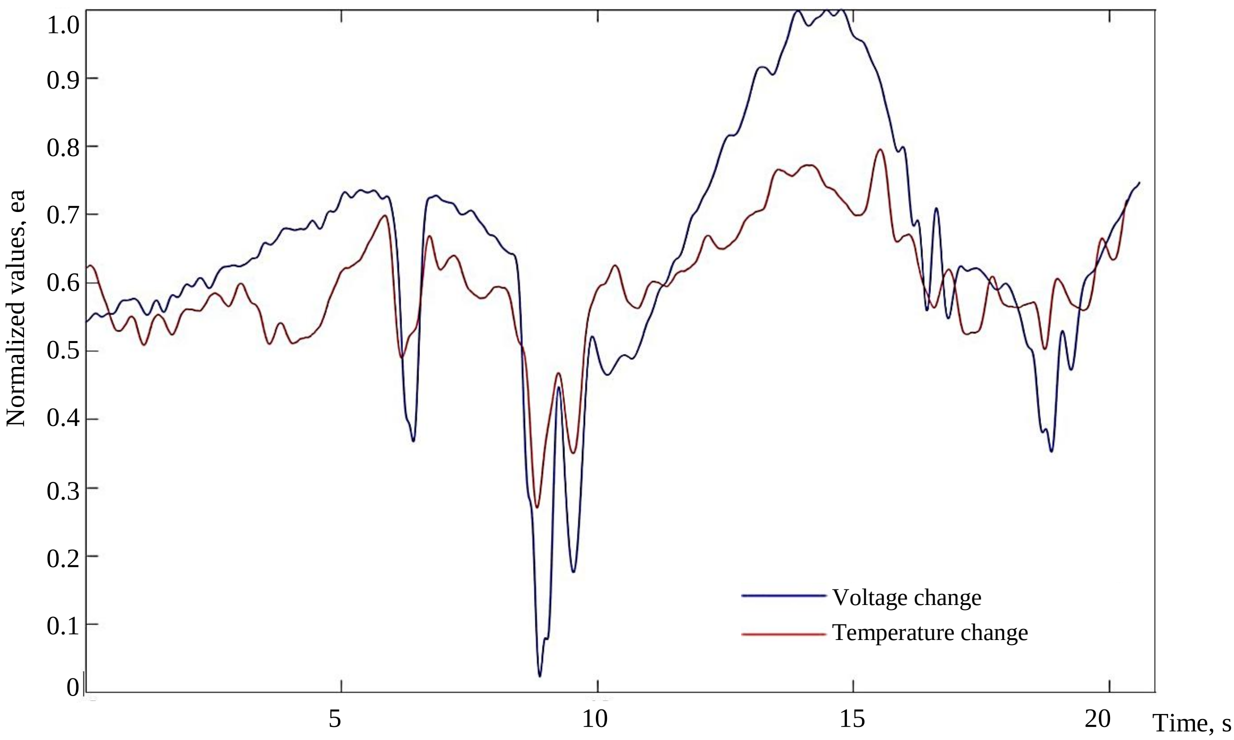

Fig. 4. Voltage changes graphs combined with temperature changes (temperature changes are taken with the opposite sign).
Values along the y-axis are normalized with respect to unity

Figure 5 shows a structural element that had no visible damage, which was also not unambiguously determined by other methods. However, as a result of processing the thermogram package, it was found that there was a thermal anomaly at the junction of two elements. This indicates that the material was probably self-heating at this point, and a defect was emerging under the surface, which would soon have to come to the surface. Thus, this section of the structure requires additional attention under future surveys.

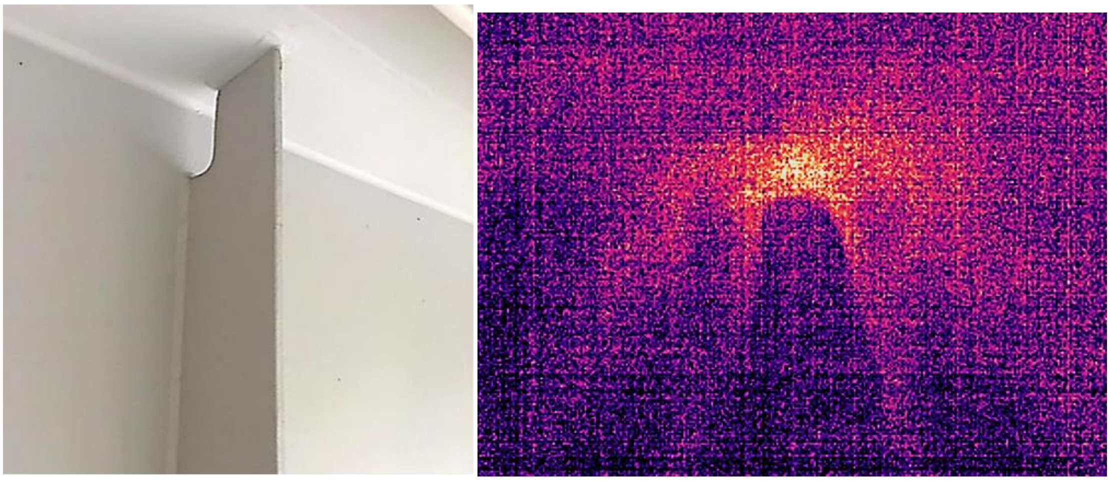

a) *b*)

Fig. 5. Infrared results: *a* — weld seam without visible fatigue damage; *b* — image of the weld toe, built from the values of matrix *B*

Discussion and Conclusions. The work carried out on the superstructures showed the effectiveness of self-reference lock-in thermography as a method of contactless diagnostics. The method performance on real objects under random load was shown. There was a correspondence of the stress change in the structure with the change in the recorded temperature. We carried out the diagnostics of some known defects, on which the continued development of damage was noted, which was subsequently confirmed by repeated examinations of these structural elements. In addition, a case of self-heating in an externally defect-free zone was identified, which indicated a probable process of the origin of the defect, which at the time of shooting could not be unambiguously diagnosed by other methods. This proves that this site requires additional monitoring. If a defect is detected at this site in the course of subsequent observations, we can talk about the possibility of using IR thermography to identify hidden defects and predict their appearance.

References

1. Solovyev LY, Solovyev AL. New technologies in bridge inspection. Proceedings of Siberian Transport University. 2020;54:14-20.

2. Vavilov V, Burleigh D. Infrared Thermography and Thermal Nondestructive Testing. Cham : Springer, 2020. 598 p.

3. Pitarresi G, Cappello R, Catalanotti G. Quantitative thermoelastic stress analysis by means of low-cost setups. Optics and Lasers in Engineering. 2020;134:106158. https://doi.org/10.1016/j.optlaseng.2020.106158

4. Breitenstein O, Warta W, Schubert MC. Lock-in Thermography. Basics and Use for Evaluating Electronic Devices and Materials. Springer Nature Switzerland AG, 2018. 342 p. https://doi.org/10.1007/978-3-319-99825-1

5. Boccardi S. Infrared thermography to monitoring mechanical tests on composite materials: Experimental procedure and data analysis. University of Naples Federico II 2017. http://dx.doi.org/10.6093/UNINA/FEDOA/11750

6. Antolis C, Rajic N. Optical Lock-in Thermography for Structural Health Monitoring – A Study into Infrared Detector Performance. Procedia Engineering. 2017;188:471−478. https://doi.org/10.1016/j.proeng.2017.04.510

7. Shiozawa D, Uchida Y, Kobayashi K, et al. Thermoelastic Stress Analysis and Dissipated Energy Evaluation Using Infrared-Optical Synchronous Measurement. In: Proc. 15th Int. Workshop on Advanced Infrared Technology and Applications. 2019;27:50. https://doi.org/10.3390/proceedings2019027050

8. Akai A, Shiozawa D, Yamada T, et al. Energy Dissipation Measurement in Improved Spatial Resolution Under Fatigue Loading. Experimental Mechanics. 2019;60:181−189. https://doi.org/10.1007/s11340-019-00552-w

9. Sieber L, Urbanek R, Bär J. Crack-Detection in old riveted steel bridge structures. Procedia Structural Integrity. 2019;17:339-346. https://doi.org/10.1016/j.prostr.2019.08.045

10. Chase SB, Adu-Gyamfi Y. Evaluation of fatigue-prone details using a low-cost thermoelastic stress analysis system. Virginia Transportation Research Council; 2016. 53 p.

11. Ciampa F, Mahmoodi P, Pinto F, et al. Recent Advances in Active Infrared Thermography for Non-Destructive Testing of Aerospace Components. Sensors. 2018;18:609. https://doi.org/10.3390/s18020609

12. Oswald-Tranta B. Lock-in inductive thermography for surface crack detection in different metals. Quantitative InfraRed Thermography Journal. 2019;16:276−300. https://doi.org/10.1080/17686733.2019.1592391

13. Vavilov VP, Klimov AG. Teplovizory i ikh primeneniya. Moscow: Intel universal; 2002. 87 p. (In Russ.).

14. Kurilenko GA. Issledovanie povrezhdaemosti metallov termodinamicheskim sposobom. Bulletin of the TPU. 2015;326:105–109 (In Russ.)

15. Boyce BR, Lesniak JR. Thermoelastic Measurement Techniques Enabled by Self-reference. Residual Stress, Thermomechanics & Infrared Imaging, Hybrid Techniques and Inverse Problems. 2019;7:125−127. https://doi.org/10.1007/978-3-319-95074-7_24

16. Izumi Y, Sakagami T, Kubo S. Accuracy improvement of self-reference lock-in thermography method and its application to detection of fatigue cracks in steel bridges. In: Proc. SPIE Conf. on Defense, Security, and Sensing, 2010. Vol. 7661. https://doi.org/10.1117/12.852961

Received 16.03.2022
Revised 06.04.2022
Accepted 17.04.2022

About the Authors:

Solovyev, Alexander L., engineer, Siberian Transport University (191, D. Kovalchuk St., Novosibirsk, 630049, RF), ORCID, Alsolovyov1337@gmail.com

Royak, Mikhail E., professor of the Applied Mathematics Department, Novosibirsk State Technical University (20, Prospect K. Marksa, Novosibirsk, 630073, RF), Dr.Sci. (Eng.), ScopusID, ResearcherID, ORCID, mikeroyak@gmail.com

Claimed contributorship

A. L. Solovyev: development and debugging of the algorithmic part; computational analysis; text preparation; formulation of conclusions. M. E. Royak: academic advising; analysis of the calculation results; the text revision; correction of the conclusions.

Conflict of interest statement

The authors do not have any conflict of interest.

All authors have read and approved the final manuscript.

INFORMATION TECHNOLOGY, COMPUTER SCIENCE, AND MANAGEMENT

Check for updates

UDC 004.934
https://doi.org/10.23947/2687-1653-2022-22-2-169-176

Original article

Analysis of Natural Language Processing Technology: Modern Problems and Approaches

Maria A. Kazakova , **Alina P. Sultanova**
Kazan National Research Technical University named after A. N. Tupolev–KAI, 10, K. Marx St., Kazan, Russian Federation
✉ kazakovamaria2609@gmail.com

Abstract

Introduction. The article presents an overview of modern neural network models for natural language processing. Research into natural language processing is of interest as the need to process large amounts of audio and text information accumulated in recent decades has increased. The most discussed in foreign literature are the features of the processing of spoken language. The aim of the work is to present modern models of neural networks in the field of oral speech processing.

Materials and Methods. Applied research on understanding spoken language is an important and far-reaching topic in the natural language processing. Listening comprehension is central to practice and presents a challenge. This study meets a method of hearing detection based on deep learning. The article briefly outlines the substantive aspects of various neural networks for speech recognition, using the main terms associated with this theory. A brief description of the main points of the transformation of neural networks into a natural language is given.

Results. A retrospective analysis of foreign and domestic literary sources was carried out alongside with a description of new methods for oral speech processing, in which neural networks were used. Information about neural networks, methods of speech recognition and synthesis is provided. The work includes the results of diverse experimental works of recent years. The article elucidates the main approaches to natural language processing and their changes over time, as well as the emergence of new technologies. The major problems currently existing in this area are considered.

Discussion and Conclusions. The analysis of the main aspects of speech recognition systems has shown that there is currently no universal system that would be self-learning, noise-resistant, recognizing continuous speech, capable of working with large dictionaries and at the same time having a low error rate.

Keywords: Natural Language Processing, oral speech, neural networks, automated natural language processing, semantic consistency.

Acknowledgements: the authors are deeply grateful to the readers for the useful comments and recommendations made during the review of the article.

For citation: M. A. Kazakova, A. P. Sultanova. Analysis of natural language processing technology: modern problems and approaches. Advanced Engineering Research, 2022, vol. 22, no. 2, pp. 169–176. https://doi.org/10.23947/2687-1653-2022-22-2-169-176

Introduction. This article provides an overview of the main language model based on the neural network for Natural Language Processing that helps computers communicate with people in their native language and scale other language tasks. Modern machine learning technologies allow computers to read text, hear speech, interpret it, measure moods, and determine which parts of speech are important. This technology is called Natural Language Processing (NLP), it is based on many disciplines, including computational linguistics. NLP is increasingly being used in interactivity and productivity applications, such as creating spoken dialogue systems and speech-to-speech engines, searching social networks for health or financial information, detecting moods and emotions towards products and services, etc.

The relevance of NLP is primarily associated with the need to process large amounts of audio and text information accumulated by mankind over the past decade. Currently, most modern devices are endowed with a voice control function, and various kinds of digital assistants are becoming widespread. Now, the speech recognition function is available in almost any gadget, it allows us to interact through voice applications, facilitating and simplifying a person's life. There are a fairly large number of commercial speech recognition systems, among the most famous there are Google, Yandex, Siri. The quality of speech recognition in such systems is at a fairly high level, but they are not without a number of shortcomings. Unfortunately, despite the amazing development of computer technology, the current problem of equipping a computer with a full-fledged, natural human voice interface is still far from over.

Materials and Methods. NLP technology is rapidly advancing due to the increased interest in the field of machine learning, as well as the availability of big data, powerful computing, and improved algorithms. However, NLP is not a new science. Attempts to teach computers to communicate with people through a natural voice interface have been made since the early days of computer technology. NLP was born with the advent of the first computers from the idea of how good it would be to use these machines to solve various useful tasks related to natural language, e.g., these programs were intended for people who, due to physiological characteristics, could not type text manually [1].

The first task that the first computers solved in the early stages of the formation of NLP was the task of machine translation, i.e., automatic translation of text from one language to another using a computer. This problem was successfully solved and started to be applied in the mid-1950s, in the past century, for the “Russian-English” pair [2].

The second task of machine learning was to create conversational systems, the programs to conduct a dialogue with a person in natural language. Many systems created at that time were imperfect due to a number of difficulties in speech recognition that can have a significant impact on the quality of the result. The difference in the voices of speaking people, the inconsistency of colloquial speech, the phonogram of the same words can vary greatly depending on a number of factors: pronunciation speed, regional dialect of the language, foreign accent, social class, and even the gender of a person [3].

The third task was to create a question-and-answer system. There was a need for programs that would answer exactly the human question. At that stage, such a question was in the form of a natural language text. Thus, the problem of scaling the recognition system has always been a significant obstacle. In the course of many years of research, it has been found that it is required to involve not only programmers, but also experts in linguistics, radio engineers, mathematicians, biologists, and even psychologists in solving the problem.

At different times, various mathematical, statistical, logical, stochastic approaches were used in natural language processing, such as Dynamic Time Warping, Bayesian discrimination, Hidden Markov Model, formal grammars, and probabilistic approaches. At the present stage of natural language processing, machine learning methods are widespread, in particular, neural networks. Currently, in modern linguistic research, at the first stage, texts are selected that are planned to be analyzed, and a corpus of texts is created. Next step, the collected material is transferred to an expert linguist. He prescribes the rules, compiles dictionaries, marks up texts for the identification of target structures in texts for the further task solution. Another method is also used, in which an expert linguist marks the text into target structures or categorizes texts in certain classes, and then machine learning methods automatically derive some rules or models for further solving current problems. At the end of the work, the quality of the methods is always checked.

Philologists study semantics of the text considering meanings of polysemantic units in context, emphasizing that context plays a fundamental role in the word definition. Therefore, e.g., the authors discover the contextual meanings of polysemantic units that are not registered in lexicographic sources. In the early stages, scientists proposed to divide any sentence into a set of words that could be processed individually, which was much easier than processing a whole sentence. This approach is similar to the one used to teach a new language to children and adults. When we first start learning a language, we are introduced to its parts of speech. Let us consider English as an example. It has 9 main parts of speech: noun, verb, adjective, adverb, pronoun, article, etc. These parts of speech help to understand the function of each word in a sentence. However, it is not enough to know the category of a word, especially for those that may have more than one meaning. Specifically, the word “leaves” can be the verb “to leave” in the 3rd person singular or the plural form of the noun “leaf”, which should be considered from the point of language as a system of interrelated and interdependent units. The idea of consistency in the lexical and semantic sphere of language was first expressed by M. M. Pokrovsky, emphasizing that “words and their meanings do not live a separate life from each other, but are connected (in our soul), regardless of our consciousness, into different groups, and the basis for their grouping is similarity or direct opposition in their basic meaning”. Paradigmatic, syntagmatic, and epidigmatic relations among language units are important manifestations of the systematic and regular nature of language. The researchers note that words enter the syntagmatic relations based on the logical contiguity of concepts and, consequently, their compatibility with each other [4].

We need to understand that from the point of view of computer science, speech is not structured information, but a sequence of characters. To ensure that voice data can continue to be used, the speech recognition application translates it into text. The accent, individual intonations, and emotions are already being erased in the text. When data are translated into text, they are translated with zeros and ones.

Therefore, computers need a basic understanding of grammar to refer to it in case of confusion. Thus, the rules for the structure of phrases appeared. They are a set of grammar rules by which a sentence is constructed. In English, it is formed with the help of a nominal and a verb group. Consider the sentence, “Kate ate the apple”. Here, “Kate” is a noun phrase and “ate the apple” is a verb phrase. Different sentences are formed using different structures. As the number of phrase structure rules increases, a parse tree can be created to classify each word in a particular sentence and arrive at its general meaning (Fig. 1).

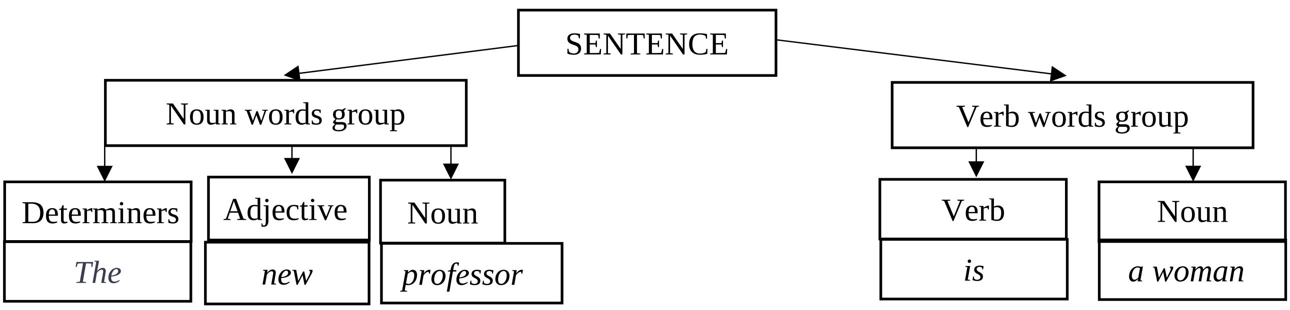

Fig. 1. Parse Tree

The spoken language system integrating speech recognition and speech synthesis is the core technology of human-computer interaction, and oral understanding is the core of spoken language system [5].

Artificial neural networks, created in the form of computer models, cope successfully with the tasks of pattern recognition. They are trainable, they can be easily adapted (and this has already been done) to solve many practical problems related to speech recognition, control of various machines and devices, event prediction, etc. The biggest feature of a deep neural network is training a large amount of data, and then extracting characteristic information. Characteristic information obtained through a network structure can give good results in the speech comprehension tasks.

An advantage of a neural network in speech processing is that the perceptron can perform discriminant learning between speech units that represent the output classes of the perceptron. The perceptron not only learns and optimizes the parameters for each class on the data belonging to it, but also tries to reject the data belonging to other classes. The perceptron is a structure with a high degree of parallelism, which allows the use of parallel hardware. The first neural network models used in speech recognition systems were developed for static signals, and not for their sequences or signals subject to temporal variability. Later, recurrent neural networks and convolutional neural networks were proposed [5].

As language models are trained on larger and larger texts, the number of unique words (the vocabulary) increases, and continuous space embedding helps to alleviate the curse of dimensionality in language modeling. An alternate description is that a neural net approximates the language function. The neural net architecture might be fed forward or recurrent, and while the former is simpler, the latter is more common. Improved algorithms, powerful computers, and an increase in digitized data have fueled a revolution in machine learning. And new techniques in the 2010s resulted in "rapid improvement in tasks" including language manipulation, in particular, transformer – architecture based on a deep learning model. It was first introduced in 2017 [6]. Table 1 presents the main types of currently existing language models of neural networks.

Table 1

Main types of neural network language models

Language model	**Characteristics**
BERT-base (2018)	Bidirectional Encoder Representations from Transformers is a new method of pretraining language. BERT is different because it is designed to read in both directions at once. Using this bidirectional capability, BERT is pretrained on two different, but related, NLP tasks: Masked Language Modeling and Next Sentence Prediction [7, 8].
ELMo (2018)	Embeddings from Language Model is a word embedding method for representing a sequence of words as a corresponding sequence of vectors, but unlike BERT, the word embeddings produced by the "bag-of-words" model is a simplifying representation. ELMo embeddings are context-sensitive, producing different representations for words that share the same spelling but have different meanings (homonyms) [9].
GPT (2018)	GPT is a Transformer-based architecture and training procedure for natural language processing tasks. Training follows a two-stage procedure. First, a language modeling objective is used on the unlabeled data to learn the initial parameters of a neural network model. Subsequently, these parameters are adapted to a target task using the corresponding supervised objective [10].
ESPnet (2018)	ESPnet mainly focuses on end-to-end automatic speech recognition (ASR), and adopts widely-used dynamic neural network toolkits, Chainer and PyTorch, as a main deep learning engine. ESPnet also follows the Kaldi ASR toolkit style for data processing, feature extraction/format, and recipes to provide a complete setup for speech recognition and other speech processing experiments [11].
Jasper (2019)	Model uses only 1D convolutions, batch normalization, ReLU, dropout, and residual connections [12].
GPT –2 (2019)	GPT-2 translates text, answers questions, summarizes passages, and generates text output on a level that, while sometimes indistinguishable from that of humans, can become repetitive or nonsensical when generating long passages [13].
WAV2LETTER++ (2019)	It is an open-source deep learning speech recognition framework. wav2letter++ is written entirely in C++, and uses the ArrayFire tensor library for maximum efficiency [14].

Language model	Characteristics
WAV2VEC (2019)	wav2vec, is a convolutional neural network that takes raw audio as input and computes a general representation that can be input to a speech recognition system [15].
XLM (2019)	These are cross-lingual language models (XLMs): one unsupervised that only relies on monolingual data, and one supervised that leverages parallel data with a new cross-lingual language model objective. It obtains state-of-the-art results on cross-lingual classification, unsupervised and supervised machine translation [16].
XLNet (2019)	XLNet uses a generalized autoregressive retraining method that enables learning bidirectional contexts through maximizing the expected likelihood over all permutations of the factorization order and autoregressive formulation. XLNet integrates ideas from Transformer-XL, the state-of-the-art autoregressive model, into retraining [17].
RoBERTa (2019)	This implementation is the same as BERT Model with a tiny embeddings tweak as well as a setup for RoBERTa pretrained models. RoBERTa has the same architecture as BERT, but uses a byte-level BPE as a tokenizer (same as GPT-2) and applies a different pretraining scheme [18].
ELECTRA (2020)	Efficiently Learning Encoder That Accurately Classifies Token Replacements is a new pre-learning method that outperforms development estimation without increasing the computational cost [19].
STC System (2020)	STC system aims at multi-microphone multi-speaker speech recognition and diarization. The system utilizes soft-activity based on Guided Source Separation (GSS) front-end and a combination of advanced acoustic modeling techniques, including GSS-based training data augmentation, multi-stride and multi-stream self-attention layers, statistics layer and spectral [20].
GPT – 3 (2020)	Unlike other models created to solve specific language problems, their API can solve “any problems in English”. The algorithm works on the principle of autocompletion: you enter the beginning of the text, and the program generates the most likely continuation of it [21].
ALBERT (2020)	ALBERT incorporates two parameter reduction techniques that lift the major obstacles in scaling pretrained models. The first one is a factorized embedding parameterization. By splitting a large vocabulary embedding matrix into two small matrices, it separates the size of the hidden layers from the size of vocabulary embedding. The second technique is cross-layer parameter sharing. This technique prevents the parameter from growing with the depth of the network [22].
BERT-wwm-ext, 2021)	Pretrained BERT with Whole Word Masking due to the complexity of Chinese grammar structure and the semantic diversity, a BERT (wwm-ext) was proposed based on the whole Chinese word masking, which mitigates the drawbacks of masking partial Word Piece tokens in pretrained BERT [23].
PaLM (2022)	This is Pathways Language Model 540-billion parameter, dense decoder. Only Transformer model trained with the Pathways system enabled us to efficiently train a single model across multiple TPU v4 Pods [24].

As can be seen from Table 1, the first transformer models, using a bidirectional capability, allowed two different but related tasks of the NLP to be studied beforehand: simulating a masked language and predicting the next sentence. Bidirectional Encoder Representations from Transformers consist of two steps: the first step is pretraining where the data enter the layers of transformer, and the result of this step are vectors for words. The second step is fine tuning. The pretraining step consists of two steps: the masked LM and Next Sentence Prediction (NSP) [7, 8]. BERT is not without flaws, the most obvious one is the learning method – the neural network tries to guess each word separately, which means that it loses some possible connections between words during the learning process. Another one is that the neural network is trained on masked tokens, and then used fundamentally different tasks, more complex ones.

Embeddings from Language Model is a deep contextualized word representation that models both complex characteristics of word usage (e.g., syntax and semantics), and how this usage varies across linguistic contexts (i.e., to model polysemy), such as “bank” in “river bank” and “bank balance”. These word vectors are learned functions of the internal states of a deep bidirectional language model (biLM), which is pretrained on a large text corpus. They can be easily added to existing models and significantly improve the state of the art across a broad range of challenging NLP problems, including question answering, textual entailment, and sentiment analysis [9].

To alleviate the problem, suffering from the discrepancy between the pretraining and fine-tuning stage because the masking token [MASK] never appears on the fine-tuning stage, XLNet was proposed, which is based on Transformer-XL. To achieve this goal, a novel two-stream self-attention mechanism, and one to change the autoencoding language model into an autoregressive one, which is similar to the traditional statistical language models, were proposed [17]. RoBERTa, STC System, GPT models were used in quite a large number of systems. And they showed pretty good results. These models suggested that averaging all token representations consistently induced better sentence representations than using the token embedding; combining the embeddings of the bottom layer and the top layer outperformed the use of the top two layers; and normalizing sentence embeddings with a whitening algorithm consistently boosted the performance [18, 20, 21].

The next step, probably, will be to study the oversampling and undersampling of textual data to improve the overall entity recognition effect.

Results. The analysis of the literary sources describing new methods of processing oral speech, which provides information about neural networks, methods for the structure and synthesis of speech, made it possible to detect the following:

1. All the models presented in the review require large computing power to solve natural language processing problems. It is computationally more expensive due to its larger structure.

2. None of the currently existing technologies enable solving the full range of tasks for recognizing continuous, defective speech.

3. Most natural language processing models are designed to handle a wide variety of English dialects and idioms.

Discussion and Conclusions. Voice assistants reproduce and reinforce all stereotypes algorithms. They, as a rule, reproduce those stereotypes that exist now in society. What does this achievement really mean? It means that the voice assistant is no worse (or maybe even better) than an average person at recognizing the speech of a person with a standard North American accent. But if an African American speaks to an assistant, then the accuracy will drop to about 80 %. This is a huge difference. Moreover, when converting voice to text, the specifics of writing, which can be important for speakers, are guaranteed to be lost.

Voice assistants do not take into account the speech and user habits of the elderly and people with special needs.

And here, it is not even always the complexity of recognition. There is, e.g., such a condition as dysarthria – a feature of the functioning of the connections between the speech apparatus and the nervous system, which can cause difficulties in pronouncing individual sounds or, in general, in speech.

Also, due to hardware limitations, any cartridge will result in too many model parameters and unsuccessful execution. The way to solve the problem of multiple cycles of dialogue requires further research.

References

1. Lee A, Auli M, Ranzato MA. Discriminative reranking for neural machine translation. In: ACL-IJCNLP 2021 – 59th Annual Meeting of the Association for Computational Linguistics and the 11th International Joint Conference on Natural Language Processing, Proceedings of the Conference, 2021. P. 7250–7264. http://dx.doi.org/10.18653/v1/2021.acl-long.563

2. Prashant Johri, Sunil Kumar Khatri, Ahmad T Al-Taani, et al. Natural language processing: History, evolution, application, and future work. In: Proc. 3rd International Conference on Computing Informatics and Networks. 2021;167:365−375. http://dx.doi.org/10.1007/978-981-15-9712-1_31

3. Nitschke R. Restoring the Sister: Reconstructing a Lexicon from Sister Languages using Neural Machine Translation. In: Proc. 1st Workshop on Natural Language Processing for Indigenous Languages of the Americas, AmericasNLP 2021. 2021. P. 122–130. http://dx.doi.org/10.18653/v1/2021.americasnlp-1.13

4. Pokrovskii MM. Izbrannye raboty po yazykoznaniyu. Moscow : Izd-vo Akad. nauk SSSR; 1959. 382 p. (In Russ.)

5. Ryazanov VV. Modeli, metody, algoritmy i arkhitektury sistem raspoznavaniya rechi. Moscow: Vychislitel'nyi tsentr im. A.A. Dorodnitsyna; 2006. 138 p. (In Russ.)

6. Lixian Hou, Yanling Li, Chengcheng Li, et al. Review of research on task-oriented spoken language understanding. Journal of Physics Conference Series. 2019;1267:012023. http://dx.doi.org/10.1088/1742-6596/1267/1/012023

7. Ashish Vaswani, Noam Shazeer, Niki Parmar, et al. Attention Is All You Need. In: proc. 31st Conf. on Neural Information Processing Systems (NIPS 2017), Long Beach, CA, USA. https://doi.org/10.48550/arXiv.1706.03762

8. Jacob Devlin, Ming-Wei Chang, Kenton Lee, et al. BERT: Pre-training of Deep Bidirectional Transformers for Language Understanding. Computing Research Repository. 2018. P. 1−16.

9. Matthew E Peters, Mark Neumann, Mohit Iyyer, et al. Deep contextualized word representations. In: Proc. NAACL-HLT. 2018;1:2227–2237.

10. Alec Radford, Karthik Narasimhan, Tim Salimans, et al. Improving Language Understanding by Generative Pre-Training. Preprint. https://pdf4pro.com/amp/view/improving-language-understanding-by-generative-pre-training-5b6487.html

11. Shinji Watanabe, Takaaki Hori, Shigeki Karita, et al. ESPnet: End-to-End Speech Processing Toolkit. 2018. https://arxiv.org/abs/1804.00015

12. Jason Li, Vitaly Lavrukhin, Boris Ginsburg, et al. Jasper: An End-to-End Convolutional Neural Acoustic Model. 2019. https://arxiv.org/abs/1904.03288

13. Chaitra Hegde, Shrikumar Patil. Unsupervised Paraphrase Generation using Pre-trained Language Models. 2020. https://arxiv.org/abs/2006.05477

14. Vineel Pratap, Awni Hannun, Qiantong Xu, et al. Wav2letter++: The Fastest Open-source Speech Recognition System. In: Proc. 2019 IEEE International Conference on Acoustics, Speech and Signal Processing (ICASSP). https://doi.org/10.1109/ICASSP.2019.8683535

15. Schneider S, Baevski A, Collobert R, et al. Wav2vec: Unsupervised Pre-Training for Speech Recognition. In: Proc. Interspeech 2019, 20th Annual Conference of the International Speech Communication Association. P. 3465−3469. https://doi.org/10.21437/Interspeech.2019-1873

16. Alexis Conneau, Guillaume Lample. Cross-lingual Language Model Pretraining. In: Proc. 33rd Conference on Neural Information Processing Systems. 2019. P. 7057−7067.

17. Zhilin Yang, Zihang Dai, Yiming Yang, et al. XLNet: Generalized Autoregressive Pretraining for Language Understanding. 2019. https://arxiv.org/abs/1906.08237

18. Yinhan Liu, Myle Ott, Naman Goyal, et al. RoBERTa: A Robustly Optimized BERT Pretraining Approach. ICLR 2020 Conference Blind Submission. 2019. https://doi.org/10.48550/arXiv.1907.11692

19. Manning Kevin Clark, Minh-Thang Luong, Quoc V Le, et al. ELECTRA: Pre-training Text Encoders as Discriminators Rather Than Generators. ICLR 2020 Conference Blind Submission. 2020. https://openreview.net/forum?id=r1xMH1BtvB

20. Medennikov I, Korenevsky M, Prisyach T, et al. The STC System for the CHiME-6 Challenge. In: Proc. 6th International Workshop on Speech Processing in Everyday Environments (CHiME 2020). 2020. P. 36−41.

21. Greg Brockman, Mira Murati, Peter Welinder. OpenAI API. 2020 : OpenAI Blog. https://openai.com/blog/openai-api/

22. Zhenzhong Lan, Mingda Chen, Sebastian Goodman, et al. ALBERT: A Lite BERT for Self-supervised Learning of Language Representations. 2020. https://arxiv.org/abs/1909.11942

23. Yiming Cui, Wanziang Che, Ting Liu, et al. Pre-Training With Whole Word Masking for Chinese BERT. In: IEEE/ACM Transactions on Audio, Speech, and Language Processing. 2021;29:3504−3514. https://doi.org/10.1109/TASLP.2021.3124365

24. Aakanksha Chowdhery, Sharan Narang, Jacob Devlin, et al. PaLM: Scaling Language Modeling with Pathways. 2022. https://arxiv.org/abs/2204.02311

Received 10.04.2022

Revised 06.05.2022

Accepted 10.05.2022

About the Authors:

Kazakova, Maria A., graduate student of the Applied Mathematics and Computer Science Department, Kazan National Research Technical University named after A.N. Tupolev–KAI (10, K. Marx St., Kazan, 420111, RF), ResearcherID, ORCID, kazakovamaria2609@gmail.com

Sultanova, Alina P., associate professor of the Department of Foreign Languages, Russian, Russian as a Foreign Language, Kazan National Research Technical University named after A.N. Tupolev–KAI (10, K. Marx St., Kazan, 420111, RF), ResearcherID, ORCID, alinasultanova@mail.ru

Claimed contributorship

M. A. Kazakova: basic concept formulation; goals and objectives of the literary review; search and analysis of literary sources; text preparation. A. P. Sultanova: generalization of the conceptual provisions of philology as a basis for the development of oral speech processing methods; the text revision.

Conflict of interest statement

The authors do not have any conflict of interest.

All authors have read and approved the final manuscript.